UC San Diego
UC San Diego Electronic Theses and Dissertations

Title
Sub Bandgap Light Detection and Photoresponse Amplification in Compensated Silicon P-N Junctions

Permalink
https://escholarship.org/uc/item/97t32605

Author
Zhou, Yuchun

Publication Date
2015

Peer reviewed|Thesis/dissertation

eScholarship.org Powered by the California Digital Library
University of California

UNIVERSITY OF CALIFORNIA, SAN DIEGO

Sub Bandgap Light Detection and Photoresponse Amplification in Compensated Silicon P-N Junctions

A dissertation submitted in partial satisfaction of

the requirements for the degree

Doctor of Philosophy

in

Electrical Engineering (Nanoscale Devices and Systems)

by

Yuchun Zhou

Committee in charge:

Professor Yu-Hwa Lo, Chair
Professor Peter Asbeck
Professor Zhaowei Liu
Professor Ivan Schuller
Professor Donald Sirbuly

2015

Copyright

Yuchun Zhou, 2015
All rights reserved.

The dissertation of Yuchun Zhou is approved, and it is acceptable in quality and form for publication on microfilm and electronically:

____

____

____

____

____

Chair

University of California, San Diego

2015

DEDICATION

To my loving family.

TABLE OF CONTENTS

Signature Page iii
Dedication iv
Table of Contents v
List of Figures vii
List of Tables x
Acknowledgements xi
Vita xiv
Abstract of the Dissertation xv

Chapter 1 Silicon Photodetectors 1
- 1.1 Introduction to Photodetectors 1
  - 1.1.1 Photoconductors 2
  - 1.1.2 Photodiodes 4
  - 1.1.3 Avalanche Photodiodes 5
  - 1.1.4 Phototransistors 6
- 1.2 Important Figures of Merits 7
  - 1.2.1 Quantum Efficiency 7
  - 1.2.2 Responsivity 9
  - 1.2.3 Response Time 9
  - 1.2.4 Device Noise 11
- 1.3 Conventional Photodiodes 13
- 1.4 Motivations and Challenges 17
- 1.5 Dissertation Outline 19

Chapter 2 Sub-Bandgap Light Detection Mechanism 20
- 2.1 Design Motivation 20
- 2.2 Sub-Bandgap Light Detection Using Silicon 21
  - 2.2.1 Franz-Keldysh Effect 21
  - 2.2.2 Quasi-quantum Confinement Effect 22
  - 2.2.3 Impurity-state Assisted Photon Absorption 23
- 2.3 Analytical Modeling 24
  - 2.3.1 Model Setup 24
  - 2.3.2 Absorption Coefficient Calculation 25
- 2.4 Conclusion 34

Chapter 3 Core-shell Nanowire Device Design, Fabrication and Characterization 35
- 3.1 Nanowire Device Design 35

3.2 Device Fabrication 36
3.3 Device Characterization 41
3.3.1 Experimental Setup 41
3.3.2 Photoresponse Measurement Results 42
3.3.3 Numerical Simulation Results 48
3.4 Conclusion 52

Chapter 4 Cycling Excitation Process (CEP) in Silicon P-N Junctions 54

4.1 Internal Gain Mechanism 54
4.2 CEP Device Design and Fabrication 55
4.3 CEP Device Characterization 57
4.3.1 Doping Concentration Profiling 57
4.3.2 Bias Dependence Measurement 60
4.3.3 Temperature Dependence Measurement 63
4.4 Results Discussion 65

Chapter 5 CEP Gain Characteristics Modeling 70

5.1 Interband Transition Calculations 70
5.2 Analytical and Simulation Results 80
5.2.1 Analytical Analysis of the CEP Process 80
5.2.2 Numerical Calculation Results 84
5.3 Conclusion 86

Chapter 6 Conclusions 88

6.1 Thesis Summary 88
6.2 Outlook 90

References 92

LIST OF FIGURES

Figure 1.1: Optical absorption coefficients for various photodetector materials 2

Figure 1.2: (a) Schematic of a photoconductor, which consists of a slab of semiconductor sandwiched between two electrodes. (b) Processes of intrinsic and extrinsic photoexcitations in photoconductors 3

Figure 1.3: Illumination of a reverse-biased p-n junction and the drift and diffusion of the photogenerated electron-hole pairs 4

Figure 1.4: The energy band diagram of an APD under illumination and large reverse bias conditions showing avalanche multiplication in the space-charge region 6

Figure 1.5: The energy band diagram of a phototransistor under illumination showing the accumulation of the holes in the base region 7

Figure 1.6: (a) Photodetection Process. (b) Equivalent circuit 12

Figure 1.7: An ideal photodiode operating in the reverse bias regime and its corresponding current-voltage characteristics. The unbiased or reversed biased photodiode experiences an increase in photocurrent I_{op} proportional to the incident optical power P 14

Figure 1.8: The spectral responsivity of a typical silicon photodiode (solid line) and the IR enhanced version of the same photodiode (dashed line) 15

Figure 1.9: Typical temperature coefficient of responsivity for a silicon photodiode 16

Figure 1.10: (a) Cross-sectional view of a p-i-n photodiode. (b) The operation of p-i-n diode and the energy band diagram under reverse bias 17

Figure 2.1: The Franz-Keldysh effect on interband absorption. The states in conduction and valence bands are separated by $\Delta E < E_g$ but the wavefunctions overlap because of the tail that tunnels into the bandgap22

Figure 2.2: 1-D schematic of relaxation of the k-selection rule by using highly boron-doped silicon. Because of the uncertainty principle, the hole in the impurity band has a highly localized wavefunction without a well-defined crystal momentum in $k-$space 23

Figure 2.3: The band diagram and simplified 1-D model illustrating the sub-bandgap light absorption process in a confined p-n junction structure 25

Figure 3.1: Process flow for the core-shell silicon nanowire photodetector 37

Figure 3.2: (a) – (c) Optical and SEM images of a fabricated core-shell silicon nanowire device 40

Figure 3.3: Overview schematic of the measurement setup 42

Figure 3.4: (a) Dark current-voltage characteristics of the fabricated arrayed silicon nanowires showing typical rectifying behavior of p-n junctions. (b) Log scale plot of the I-V plot with the extraction of the ideality factor n = ~1.71 43

Figure 3.5: (a) Dark and light measurements in the reverse bias region at 1054 nm. (b) Dark and light measurements in the reverse bias region at 1310 nm. Note the very different voltage-dependent behaviors of photocurrent in the reverse bias region. The photoresponse increases rapidly with the reverse bias only for sub bandgap (1310 nm) photons 45

Figure 3.6: Measured photo-responsivity of the nanowire devices and the planar device 46

Figure 3.7: Photo-responsivities of the nanowires with various diameters and the planar structure obtained from calibrated calculations 48

Figure 3.8: Schematic of the simulated structure and the range of p-core and n-shell, respectively 49

Figure 3.9: The concept of sub-bandgap photon absorption illustrating the interaction between a confined electron wave function (blue) and a localized impurity state wavefunction (red) in a core-shell silicon nanowire at 1.5 V reverse bias 50

Figure 3.10: Comparisons between experimental data and simulation results of the 300-nm diameter nanowires assuming the diffused p-n junction has a 1×10^{19} $cm^{-3}/2\times10^{17}$ cm^{-3} effective doping level and a core/shell radius of 66 nm/84 nm 51

Figure 3.11: Calculated absorption coefficient dependence on the effective doping concentration in the n-shell region of a nanowire under different reverse bias conditions 52

Figure 4.1: (a) Dark current-voltage characteristics of the diffused p-n junction in the absence of light illumination. Inset: Optical microscope image of the fabricated device. (b) Log scale plot of the dark I-V characteristics of the sample junction. The ideality factor is 1.98 57

Figure 4.2: (a) SIMS profile of phosphorous and boron in the OMCVD grown silicon p-n junction. (b) SIMS profile of phosphorous and boron in the diffused p-n junction. 58

Figure 4.3: (a) Effective doping concentrations of the OMCVD junction. Inset: compensation ratio near the metallurgical junction. (b) Effective doping concentrations of the diffused junction. Inset: compensation ratio near the metallurgical junction 59

Figure 4.4: Experimental Setup for CEP device measurement 61

Figure 4.5: Packaged device ready for measurement 61

Figure 4.6: Bias dependence of photoresponse to 635 nm laser light for both the diffused and OMCVD epitaxial grown Si p-n junctions at room temperature 62

Figure 4.7: Bias dependence of photoresponse to 635 nm laser light at various temperatures for the diffused p-n junction with high doping concentration 64

Figure 4.8: Comparison of the temperature dependence of photoresponse between a highly compensated silicon p-n junction and a conventional silicon p-i-n diode at -3 V.. 65

Figure 4.9: Schematic illustration of a cycling excitation process assuming a photon is absorbed in the p-region of the p-n junction and the first two excitation events were depicted in the schematic 67

Figure 4.10: Density of states (DOS) distribution with respect to the band diagram in the n-region of the p-n junction. The red arrow indicates the excitation process of bringing an electron across the energy gap from an ionized acceptor (A^-) in the n-region 68

Figure 5.1: Average number of electron-hole pairs (N) generated by an energetic carrier as a function of the bias voltage from numerical simulations 79

Figure 5.2: Carrier multiplication by cycling excitation process initiated from a single photon incident on either the p-side or n-side of the heavily doped and compensated junction 81

Figure 5.3: Block diagram illustration of the cycling excitation process (CEP), taking the process initiated by a photon absorbed in the p-region of the p-n junction as an example, in which the $j-$th hot electron or hole can produce X_j or Y_j e-h pairs in each excitation event 82

Figure 5.4: The photoresponse gain as a function of the mean value of x/y, and x/y varies from 0.01 to 0.99 under the assumption that $P_p = P_n$ and $x = y$ 83

Figure 5.5: Average number of electron-hole pairs N generated by an energetic carriers as a function of the bias voltage at different temperatures, obtained from measured data in Figure. 4.7 and eqn. (5.44) 83

Figure 5.6: (a) Histogram of gain distribution with the e-h pair generation probability at $p = 0.5$ with corresponding gain value of 2 and noise factor N.F. =1.2557. (b) Histogram of gain distribution for $p = 0.95$, with the corresponding gain value of 20.0 and noise factor N.F. =1.4789 85

LIST OF TABLES

Table 1.1: Typical values of gain and response time for common photodetectors 11

ACKNOWLEDGEMENTS

First of all, I would like to thank my advisor, Prof. Yu-Hwa Lo, for his guidance throughout my entire Ph.D. career. His tremendous knowledge and vast experience was instrumental to my development as a scientific researcher, and was always able to provide useful advice and creative solutions to the problems that I faced during my studies at UCSD. Second, I would like to thank Prof. Lu Sham for his guidance on the physical modelings and his in-depth understanding of physics. Third, I would like to thank Dr. Deli Wang for his support during my very first days at UCSD. I would also like to thank the rest of my committee members: Prof. Peter Asbeck, Prof. Zhaowei Liu, Prof. Ivan Schuller, and Prof. Donald Sirbuly for the assistance and guidance they provided.

I would like to thank all my past and present lab members for the support they have provided over the past few years. I thank Dr. James Cheng, Dr. Hongkwon Kim and Dr. Sifang You for their help in training me the experimental techniques and mentorship during the beginning of my Ph.D. Career. I thank Dr. Samia Rahman and Yu-hsin Liu for their participation and the insightful discussions we had on various projects. I also thank the rest of the group for their constant support and friendship: Dr. Tsung-Fong Wu, Dr. Wen Qiao, David Hall, Tony Yen, Zhe Mei, Wei Cai, and Tiantian Zhang.

I would also like to thank Dr. Ke Sun, Dr. Dylan Lu, Dr. Dingbo Chen, Dr. Yi Jing, Dr. Wei Lu, Dr. Muchuan Yang, Dr. Janet Pan and Namseok Park for the tricks and companionship they provided during the countless hours I spent in the cleanroom.

I also have to thank the Nano3 staff for providing the excellent cleanroom facility and technical support which made my research possible: Larry Grissom, Ivan Harris, Dr. Xuekun Lu, Dr. Ahmet Erten, Sean Parks, Ryan Anderson, Dr. Maribel Montero, and Dr. Bernd Fruhberger.

Most importantly, I would like to thank my family for their constant support and great encouragement during my Ph.D. career. I would take the opportunity to convey my special thanks to my parents, Jun Zhou and Lan Luan who're there for me through all the ups and downs and supported me in all the possible ways.

Portions of Chapter 2 is a reprint of materials as it appears in the following publication: Yuchun Zhou, Yu-hsin Liu, James Cheng and Yuhwa Lo, "Bias dependence of sub-bandgap light detection for core-shell silicon nanowires", Nano Letters, 12, 5929-5935 (2012). The dissertation author was the primary investigator and author of this material.

Portions of Chapter 3 is a reprint of materials as it appears in the following publications: Yuchun Zhou, Yu-hsin Liu, James Cheng and Yuhwa Lo, "Bias dependence of sub-bandgap light detection for core-shell silicon nanowires", Nano Letters, 12, 5929-5935 (2012); Yu-hsin Liu, Yuchun Zhou, and Yuhwa Lo, "High efficiency silicon 1310 nm detector without defect states or heteroepitaxy", Applied Physics Letters, 103, 041119 (2013). The dissertation author was the primary/secondary investigator and author of these materials.

Portions of Chapter 4 and 5 is a reprint of materials as it appears in the following publication: Yuchun Zhou, Yu-hsin Liu, Samia Rahman, David Hall, L.J. Sham, and Yuhwa Lo, "Discovery of a photoresponse amplification mechanism in compensated

PN junctions", Applied Physics Letters, 106, 031103 (2015). The dissertation author was the primary investigator and author of this material.

VITA

2009	Bachelor of Science, Beijing Jiaotong University Optical Information Science and Technology
2011	Master of Science, University of California, San Diego Electrical Engineering (Nanoscale Devices and Systems)
2015	Doctor of Philosophy, University of California, San Diego Electrical Engineering (Nanoscale Devices and Systems)

PUBLICATIONS

1. **Y. Zhou**, Y.H. Liu, S.N. Rahman, D. Hall, L.J. Sham, and Y.H. Lo, "Discovery of a photoresponse amplification mechanism in compensated PN junctions", Applied Physics Letters, 106, 031103 (2015).

2. Y.H. Liu, **Y. Zhou**, and Y.H. Lo, "High efficiency silicon 1310 nm detector without defect states or heteroepitaxy", Applied Physics Letters, 103, 041119 (2013).

3. Y.H. Liu, **Y. Zhou**, and Y.H. Lo, "Efficient detection of 1310 nm light using silicon nanoscaled p/n junctions", IEEE Photonics Conference, Bellevue, USA (2013).

4. A. Kargar, K. Sun, Y. Jing, C. Choi, H. Jeong, **Y. Zhou**, K. Madsen, P. Naughton, S. Jin, G.Y. Jung, and D. Wang, "Tailoring n-ZnO/p-Si branched nanowire heterostructures for selective photoelectrochecmical water oxidation or reduction", Nano Letters, 13, 3017–3022 (2013).

5. K. Sun, Y. Jing, X. Zhang, R. Aquinaldo, A. Kargar, K. Madsen, K. Banu, **Y. Zhou**, Y. Bando, Z. Liu, and D. Wang, "3D branched nanowire heterojunction photoelectrodes for high-efficiency solar water splitting and H_2 generation", Nanoscale, 4, 1515-1521 (2012).

6. **Y. Zhou**, Y. H. Liu, J. Cheng and Y.H. Lo, "Bias dependence of sub-bandgap light detection for core-shell silicon nanowires", Nano Letters, 12, 5929-5935 (2012).

ABSTRACT OF THE DISSERTATION

Sub Bandgap Light Detection and Photoresponse Amplification in Compensated Silicon P-N Junctions

by

Yuchun Zhou

Doctor of Philosophy in Electrical Engineering (Nanoscale Devices and Systems)

University of California, San Diego, 2015

Professor Yu-Hwa Lo, Chair

This thesis presents work on two significant research areas in silicon photonics. The first is focused on improving the capability of using single crystal silicon for infrared photon detection. A vertically arrayed core-shell silicon nanowire device has been fabricated and characterized for the investigation of the bias dependence behavior of the sub-bandgap light detection. The intrinsic properties of the nanowire device are based on three physical mechanisms: Franz-Kelydsh effect, quasi-quantum confinement effect, and the impurity state assisted photon absorption. A detailed physical model incorporates all the three physical mechanisms has been developed to analyze its fundamental characteristics and an excellent agreement with the experimental data has

been found.

The second is on the discovery of a new photoresponse amplification mechanism in highly doped and heavily compensated silicon p-n junctions. The new gain mechanism has been investigated by measuring the photoresponse behavior of a simple planar mesa device. The distinctive characteristics of such an internal amplification mechanism include the gain occurs at bias voltage as low as -2 V and the amplified signal is enhanced rather than suppressed with increasing temperature. A physical model – cycling excitation process (CEP) has been proposed based on the experimental observations. Results from theoretical modeling, fabrication, and experimental measurements of these devices are discussed. In particular, the gain mechanism works in low voltage range and favors room temperature over cryogenic temperature, makes it promising for practical device applications.

Chapter 1

Silicon Photodetectors

Semiconductor photodetectors are devices that can detect optical signals though photoelectric processes. Photodetectors are necessary and very important in optical communications, accurate measurements for scientific and industrial applications, consumer electronics, and medical purposes. Silicon photodetectors have been widely used in these fields. This chapter presents a review of various photodetection mechanisms and the important figures of merits for silicon photodiodes.

1.1 Introduction to Photodetectors

The general operation of a photodetector involves three processes: (1) carrier generation through photoexcitation, (2) carrier transport and/or multiplication by specific gain mechanisms, and (3) carrier collection as terminal current to provide the output signal [1]. Different kinds of semiconductor material are chosen and optimized for photodetection at various wavelengths of interest. Absorption coefficient α is the parameter that determines the amount of light absorbed by photoexcitation. A high value of absorption coefficient indicates that light is absorbed near the surface of the photodetector, and light can penetrate deeper into the semiconductor if the material has a low value of absorption coefficient. Figure 1.1 shows the measured spectral response

of the intrinsic (the photoexcitation happens between the band edges) absorption coefficient of various semiconductors.

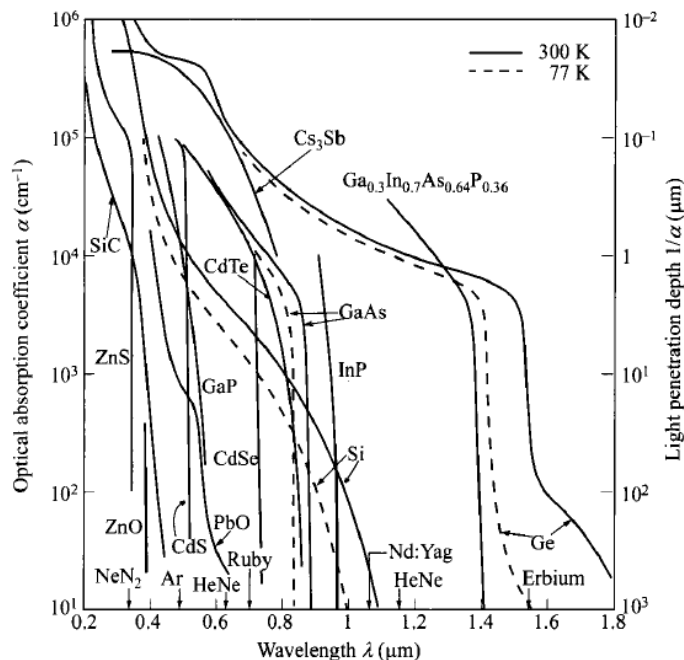

Figure 1.1: Optical absorption coefficients for various photodetector materials [1].

1.1.1 Photoconductors

Photoconductor is one of the most commonly used photodetectors. The structure of a photoconductor is very simple and consists of a slab of semiconductor, either in bulk or thin-film form, with Ohmic contacts at two opposite ends. Therefore, the photoconductor is attractive for its simple structure, low cost, and rugged features. The incoming light is absorbed in the semiconductor between the two contacts, and carriers are generated through photoexcitation. The photoexcitation process is either from band-to-band transition or extrinsic transition between the impurity band and the conduction

band (or valence band) as shown in Figure 1.2. Extrinsic photoconductors can therefore be used as long-wavelength light detectors without using materials of very narrow energy gap (e.g. infrared photodetectors). For mid-infrared to far-infrared and longer wavelengths, the photoconductors are cooled to lower temperatures (such as 77 K and 4.2 K). The lower temperatures reduce thermal effects which cause thermal ionization and deplete the energy levels, and increase the gain and detection efficiency. For photoconductors a gain of 1000 is typical, and a gain as high as 10^6 has also been achieved [1]. The response time of a photoconductor is determined by the carrier life time and the trade-off between gain and response time needs to be considered for different applications. Generally, a photoconductor has a much longer response time compared to that of a photodiode.

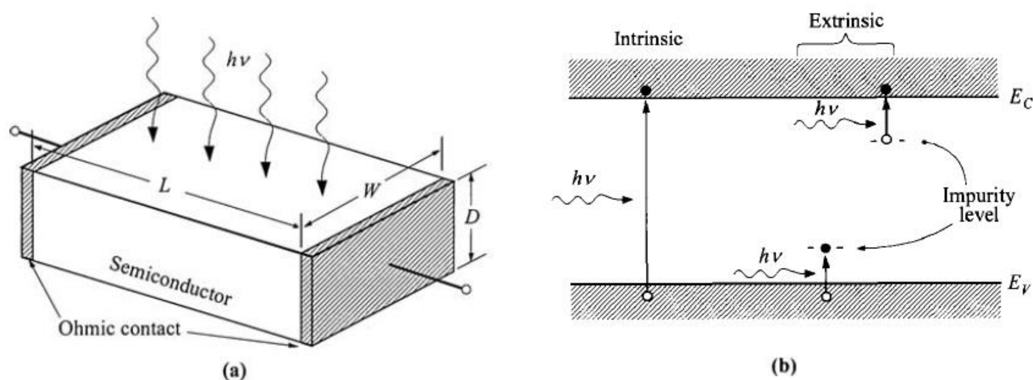

Figure 1.2: (a) Schematic of a photoconductor, which consists of a slab of semiconductor sandwiched between two electrodes. (b) Processes of intrinsic and extrinsic photoexcitations in photoconductors [1].

1.1.2 Photodiodes

A photodiode has a structure similar to a regular semiconductor p-n junction or a p-i-n diode, and is operated under reverse bias for optical signal detection. In the presence of light with photon energy greater than the bandgap of the semiconductor, excess electron-hole pairs are generated near the junction, resulting in a change of the current-voltage characteristics of the diode. Figure 1.3 presents the charge carrier transport mechanism in an illuminated reverse biased p-n junction photodiode [2].

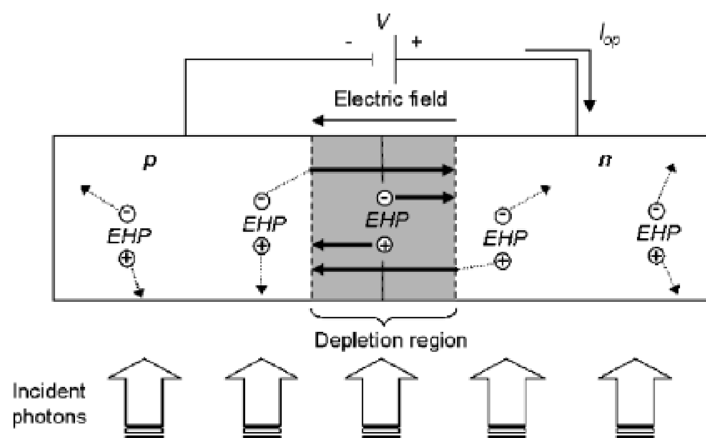

Figure 1.3: Illumination of a reverse-biased p-n junction and the drift and diffusion of the photogenerated electron-hole pairs [2].

The photogenerated electron-hole pairs in the depletion region of the junction are swept out by the electric field induced by the built-in potential and the applied reverse bias. Then these excess electrons recombine with holes at the metal contacts. If the device is reverse biased, such process can be enhanced due to the increased width of the depletion region, in which more photoexcited carriers will be captured to contribute to the photocurrent. The electron-hole pairs generated within the depletion

region and the region within a diffusion length from the depletion region will produce photocurrent. Electron-hole pairs generated far away from the depletion layer will be lost by recombination and produce no photocurrent. The current voltage characteristic of an ideal p-n junction becomes:

$$I = I_s\left(e^{\frac{qV}{kT}} - 1\right) - I_{op} \tag{1.1}$$

where I_s is the drift current according to the traditional p-n junction theory, and I_{op} is the photocurrent introduced by the photoexcitations. The magnitude of photocurrent is proportional to the incoming optical power below saturation.

1.1.3 Avalanche Photodiodes

Avalanche photodiodes (APDs) are photodiodes that operate at high reverse bias voltages and produce very high gain and high speed. The major characteristic of avalanche photodiodes is that avalanche multiplication is introduced as an internal signal amplification mechanism to produce gain. If the reverse bias voltage is high enough, the electric field in the depletion (space-charge) region will eventually become strong enough to cause both optically and thermally generated electrons and holes to gain sufficient kinetic energy, and impact ionization can occur when collisions between carriers take place. Impact ionization produces more energetic electrons and holes and these carriers can generate further impact ionizations to produce more electron-hole pairs. Such processes can repeat to produce gain until it reaches a steady state or the limit determined by the series resistance and the external circuitry [1]. The avalanche multiplication process is shown in Figure 1.4. However, since both thermally generated

(dark current) and photoexcited carriers (photocurrent) go through the same impact ionization processes, the high gain may come with the price of high dark current and noise.

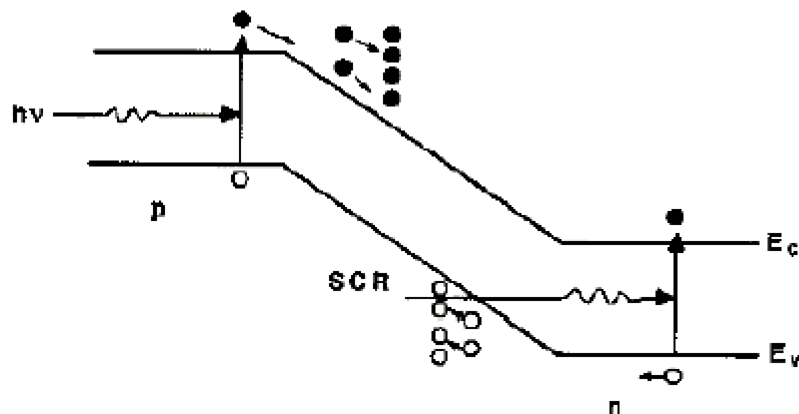

Figure 1.4: The energy band diagram of an APD under illumination and large reverse bias conditions showing avalanche multiplication in the space-charge region [3].

1.1.4 Phototransistors

A phototransistor is in essence a bipolar transistor that can produce high gain through internal bipolar-transistor action. Figure 1.5 presents the schematic of the band diagram of a floating base n-p-n bipolar phototransistor biased in the active regime under light illumination. A floating base means that a positive bias is applied to the collector with respect to the emitter. Light is absorbed near the depletion region between the base and the collector. The photogenerated holes move to and are accumulated in the base. The accumulation of holes in the base lowers the energy barrier between base and emitter and attracts more electrons from the emitter to the collector. The electron

transit time through the base is usually much shorter than the minority-carrier life time, and the gain mechanism of phototransistor is similar to that of bipolar transistors.

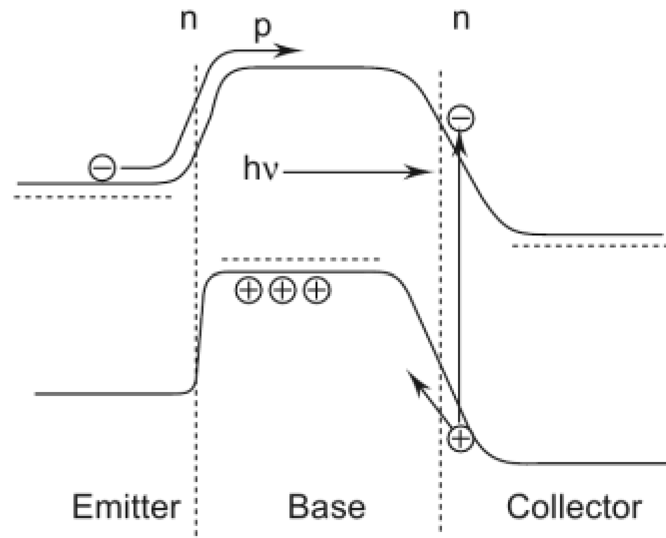

Figure 1.5: The energy band diagram of a phototransistor under illumination showing the accumulation of the holes in the base region [4].

Compared to avalanche photodiodes, phototransistors do not require high voltage operation, yet provides a decent photocurrent gain. On the other hand, photoreceivers using phototransistors usually produce lower sensitivity and speed and greater thermal noise than PIN-FET or APD receivers.

1.2 Important Figures of Merits & Definitions

1.2.1 Quantum Efficiency

Quantum efficiency is defined as the number of carriers produced per photon, or in other words the probability that a single photon will generate an electron-hole pair that contributes to the photocurrent. Thus, the quantum efficiency η can be represented by the following equation:

$$\eta = \frac{I_{ph}}{q\Phi} = \frac{I_{ph}}{q}(\frac{h\upsilon}{P_{opt}}) \tag{1.2}$$

where I_{ph} is the photocurrent, Φ is the photon flux $(= P_{opt}/h\upsilon)$, and P_{opt} is the incoming optical power [1].

For normal photodiodes without any internal gain mechanisms, the ideal quantum efficiency is unity $(0 < \eta \leq 1)$. The reduction is usually caused by loss due to reflection, in-coupling at the detector interface, incomplete absorption and recombination. Another useful expression is the external quantum efficiency:

$$\eta_{ext} = T_{op}F_{EHP}(1 - e^{-\alpha L}) \tag{1.3}$$

where T_{op} is the percentage of the incoming optical power transmitted at the detector interface. F_{EHP} is the fraction of the generated electron-hole pairs that finally contribute to the photocurrent, α is the absorption coefficient (cm^{-1}) and L is the active photodetector length [2]. External quantum efficiency η_{ext} is usually the value that can be measured directly. Taking a photodetector integrated with an optical waveguide for example, T_{op} includes the insertion loss between the fiber and the waveguide as well as the reflection loss due to the coupling between the photodetector and the waveguide. And the internal quantum efficiency can be expressed as $\eta_{int} = \eta_{ext}/T_{op}$.

1.2.2 Responsivity

Responsivity is defined as the ratio between the photocurrent and the incoming optical power. Its quantity is related to the quantum efficiency according to the following relation:

$$R = M\frac{q\eta}{h\nu} \tag{1.4}$$

In eqn. (1.4), a multiplication (gain) factor M is introduced due to any photoresponse amplification mechanism in a specific photodetector. Similar to quantum efficiency, responsivity is dependent on the absorption coefficient α. Since the absorption coefficient is a strong function of wavelength, the responsivity is wavelength dependent. Since most of semiconductor photodiodes use band-edge photo-excitation of charge carriers for photodetection, the long-wavelength cutoff λ_c is determined by the energy bandgap of semiconductor material. For silicon $\lambda_c \sim$ 1.1um. For wavelength longer than λ_c, α is too small to give rise to enough photoresponse. The short wavelength cutoff, on the other hand, is due to the fact that most of the light is absorbed near the surface of the photodetector where surface recombination is more likely to happen. The photogenerated electron-hole pairs thus recombine before they can reach the p-n junction. Therefore, proper device structure designs need to be considered to increase the responsivity and quantum efficiency. In general, for a given wavelength, the photocurrent increases linearly with the incident optical power (R is a constant), until a saturation level is reached.

1.2.3 Response Time

The fundamental response time or speed limit of a photodiodes is limited by three factors: (1) the drift time of the carriers going through the depletion region; (2) the diffusion time of carriers generated outside the depletion region; and (3) the capacitance of the depletion region.

The drift time of carriers in the depletion region is mainly determined by the depletion layer width and the electric field. At low electric fields, the drift velocity is given by:

$$v_d = \mu E \tag{1.5}$$

where E is the electric filed within the depletion region and with sufficient reverse bias voltage, the carrier will move with a saturation drift velocity. The carriers generated outside the depletion region need to diffuse into the junction, which could result in a considerable time delay. The diffusion time is relatively slow, and is limited by the recombination lifetime τ. To minimize the diffusion effect, it is desirable to have a depletion region wide enough by ensuring most of the photogenerated electron-hole pairs are generated within the depletion region itself and to make the junction very close to the detector surface. The junction capacitance, which arises due to the ionized donors an acceptors in the depletion region, taking an abrupt P-N junction as an example, the junction capacitance C_j can be represented by the following equation:

$$C_j = \frac{\varepsilon A}{W} \tag{1.6}$$

where ε is the dielectric constant of the semiconductor material, A is the cross section area of the junction, and W is the depletion width. So the depletion width should not be

too thin, since a larger $R_L C$ time constant will be introduced, where R_L is the load resistance. So, while designing a detector, attention needs to be paid for selecting an optimum compromise in depletion layer width of a specific junction.

Table 1.1: Typical values of gain and response time for common photodetectors

Photodetector		Gain	Response time (s)
Photoconductor		1–10^6	10^{-8}–10^{-3}
Photodiodes	*p-n* junction	1	10^{-11}
	p-i-n junction	1	10^{-10}–10^{-8}
	Metal-semiconductor diode	1	10^{-11}
CCD		1	10^{-11}–10^{-4}
Avalanche photodiode		10^2–10^4	10^{-10}
Phototransistor		$\approx 10^2$	10^{-6}

Table 1.1 summarizes typical values of gain and response time for common photodetectors [1].

1.2.4 Device Noise

There are two major noise sources in a photodiode or photoreceiver: shot noise and thermal noise. To illustrate the noise characteristics, a general photodetection process is shown in Figure 1.6(a). Both optical signal and background radiation are absorbed by the photodetector, where by photoelectric effect electron and hole pairs are generated. After which, the electrons and holes are separated by the electric field and drift toward the opposite ends of the junction. In the process, a photocurrent signal and noise is induced in the external load resistor.

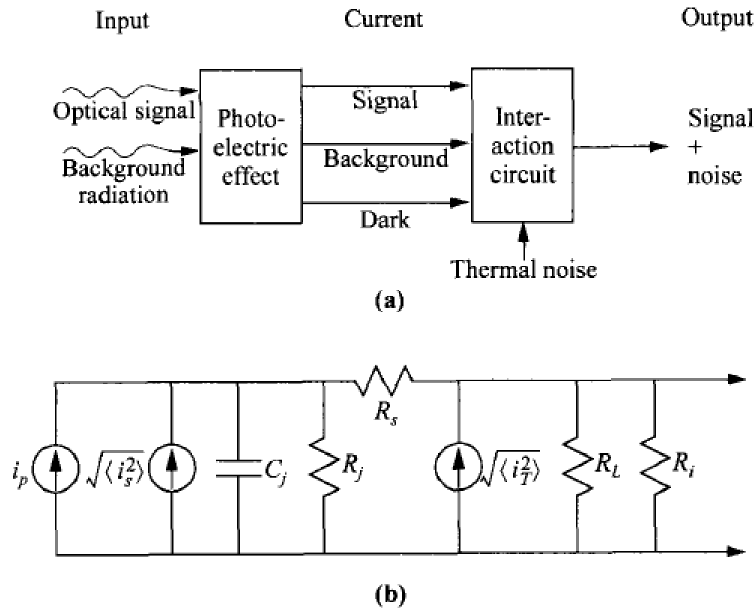

Figure 1.6: (a) Photodetection Process. (b) Equivalent circuit [1].

The shot noise is due to random fluctuations in the flow of charge carriers, which is affected by various contributions to the overall current and can is given by:

$$\langle i_s^2 \rangle = 2qB(I_P + I_B + I_D) \tag{1.7}$$

In eqn. (1.7), we designate the root-mean-square (RMS) shot noise to be $\langle i_s^2 \rangle$, the current resulting from the background radiation to be I_B, the dark current of the photodiode to be I_D. I_P is the photocurrent of the photodiode and B is the bandwidth. I_B is usually small and can be negligible. The dark current I_D is almost due to thermal generation within the depletion layer if the photodiode is reverse biased at a modest voltage.

The thermal noise, or Johnson noise, is determined by the junction resistance R_j, the series resistance R_S, the external load resistor R_L, and the input resistance R_i of the following amplifier (Figure 1.6(b)). Among which, the series resistance is usually much smaller than other resistances and can be neglected. Therefore, in the equivalent circuit, the other three contributing resistances can be combined to give the equivalent resistance R_{eq}. The thermal noise is then given by:

$$\langle i_T^2 \rangle = \frac{4kTB}{R_{eq}} \tag{1.8}$$

where

$$\frac{1}{R_{eq}} = \frac{1}{R_j} + \frac{1}{R_L} + \frac{1}{R_i} \tag{1.9}$$

Another important figure associated with the noise characteristics is the signal-to-noise ratio (SNR), which is the ratio between the mean-squared photocurrent (assuming the average optical power is P_{opt}) and the variance originated from shot and thermal noise:

$$SNR = \frac{(1/2)(q\eta P_{opt}/h\nu)^2}{2qB(I_P+I_B+I_D)+4kTB/\,R_{eq}} \tag{1.10}$$

The minimum optical power required to obtain a measurable signal for a given SNR and bandwidth can be determined using the above equation by setting $I_P = 0$. This is especially important in the context of measuring a modulated signal [5], [6].

1.3 Conventional Photodiodes

Conventional photodiodes are reverse biased p-n or p-i-n didoes operating below the breakdown voltage. Figure 1.7 shows a typical p-n junction photodiode's biasing condition and its corresponding current-voltage characteristics in the voltage range far away from the breakdown voltage. In the presence of photons with energy higher than the bandgap energy of silicon (~ 1.1 μm), besides the dark current additional current from the electron-hole pairs generated by photoexcitation within in the junction will change the I-V characteristics of the biased device. Due to the presence of extra electrons and holes within the biased and closed circuit loop, the magnitude of the reverse current is enhanced on top of the dark current. This increased current therefore is defined as the photocurrent I_{op}. Under modest bias conditions, the magnitude of the photocurrent is proportional to the incident optical power until the saturation level is reached, for example, $I_{op1} < I_{op2}$ as shown in Figure 1.7.

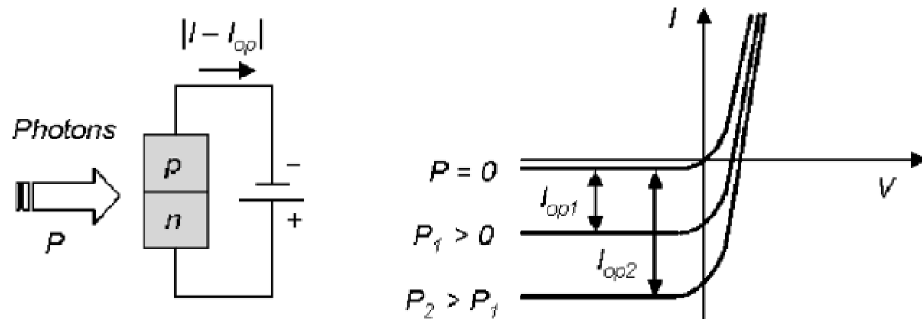

Figure 1.7: An ideal photodiode operating in the reverse bias regime and its corresponding current-voltage characteristics. The unbiased or reversed biased photodiode experiences an increase in photocurrent I_{op} proportional to the incident optical power *P* [2].

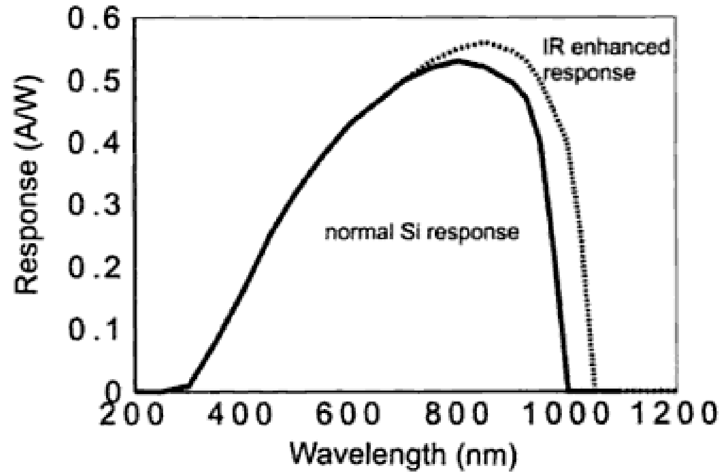

Figure 1.8: The spectral responsivity of a typical silicon photodiode (solid line) and the IR enhanced version of the same photodiode (dashed line) [7].

The spectral responsivity of a typical silicon photodiode is shown in Figure 1.8. The response of a given detector is a strong function of wavelength. On the long wavelength end, as described in the previous section, the rapid drop in responsivity is caused by the bandgap of silicon, even for the state-of-the art infrared enhanced photodetector, the cut-off wavelength is usually still below 1200 nm. On the other hand, the decrease of responsivity as the wavelength becomes shorter is due to the large value of absorption coefficient, and the optical power is absorbed near the detector surface, where recombination is more likely to happen. Responsivity increases slightly with the reverse bias due to the enhanced carrier collection. Figure 1.9 also presents the temperature dependence of responsivity of a normal silicon photodiode. The spectral response will vary depending on the processing. However, the general features are mainly determined by the temperature effect on the band gap [8].

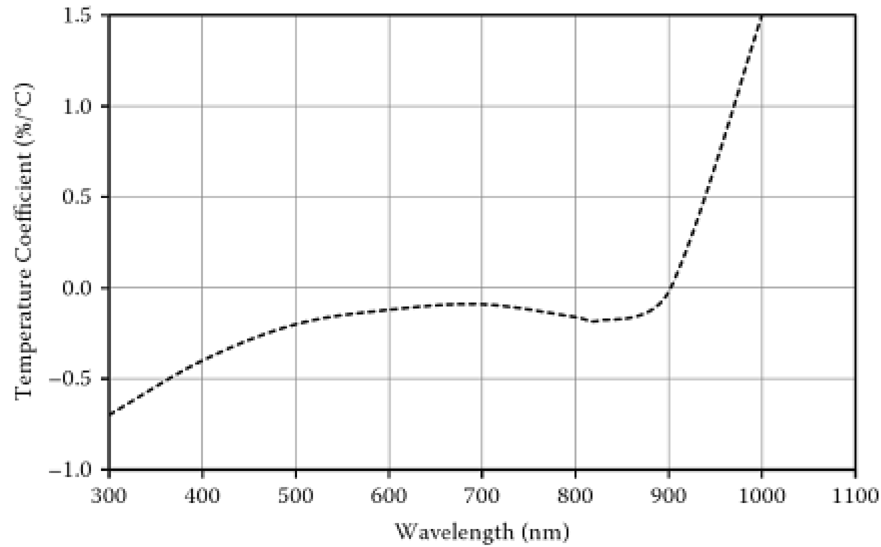

Figure 1.9: Typical temperature coefficient of responsivity for a silicon photodiode [8].

The p-i-n diode is a special variation of the p-n junction photodiodes, and is one of the most commonly used the photodetectors, which is shown in Figure 1.10. The thickness of the depletion region is optimized by sandwiching an intrinsic or lightly doped region between and p- and n- region. In this structure, two depletion regions form between the p- and i- interface and n- and i- interface. These two depletion regions may combine with each other to form a single large depletion region where more photons can be captured, resulting in enhanced responsivity of the detector. Most of the conventional avalanche photodetectors are also reverse biased p-i-n diodes operating below the breakdown voltage.

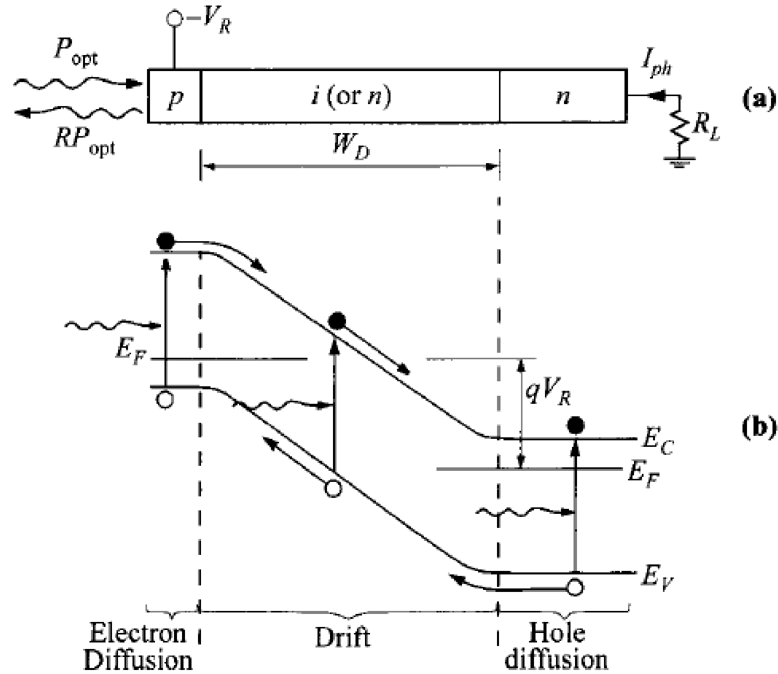

Figure 1.10: (a) Cross-sectional view of a p-i-n photodiode. (b) The operation of p-i-n diode and the energy band diagram under reverse bias [1].

1.4 Motivations & Challenges

Since silicon is the most important and commonly used semiconductor material and the standard complementary metal-oxide-semiconductor (CMOS) technologies are mainly based on silicon, tremendous efforts and various approaches have been investigated in enabling silicon for infrared and sub-bandgap photon detection because the development of power monitoring is essential for any optical communication technology. However, since intrinsic silicon has a negligible response to infrared photons ($\lambda > 1.15$ μm) with energies lower than its bandgap energy, it poses a great challenge to use silicon as an active absorbing material for infrared photodetection. In

order to sensitize silicon to sub-bandgap photons, the incorporation of germanium with silicon as the optically responsive element, two-photon absorption processes, surface-plasmon Schottky detectors, and detection using defect states have been widely studied [9] – [12]. However, the development of SiGe devices is greatly tempered by the material growth as well as the waveguide integration issues. Both the surface plasmon enhanced mechanisms and the two-photon absorption process require a high photon density in a very small interaction volume, therefore complicated fabrication techniques are necessary. Detectors using defect or interfacial states usually produce inconsistent results and hard to reproduce [13], [14].

Avalanche amplification induced by impact ionization has been the only primary internal signal amplification mechanism over the past few decades. Most of the state-of-the-art photoreceivers for telecommunications and single photon avalanche diodes (SPADs) for quantum communications and imaging have adopted this mechanism [15] – [22]. However, impact ionization usually requires high bias voltage, typically 30 to 200 V depending on the applications and the semiconductor materials, and often suffers from high excess noise associated with the avalanche process. Moreover, most of the avalanche photodiode devices (APDs) are fabricated using III-V materials, it is incompatible with the mainstream CMOS process, and imposes serious limits on the power consumption and the level of integration (e.g. number of pixels for imaging applications) [23] – [26].

To summarize, there is no current technology which can offer effective infrared or sub-bandgap light detection using single crystal silicon and there is no effective

amplification mechanism that can be utilized in silicon to produce comparable performance observed in the current III-V APD devices. The goal of this work is to develop a device technology that can enable single crystal silicon for effective infrared photon detection as well as to investigate a new photoresponse amplification mechanism that can potentially give rise to a new series of semiconductor devices.

1.5 Dissertation Outline

Following the first chapter of introduction, Chapter 2 will present the design that utilizes three physical mechanisms for sub-bandgap photon detection using single crystal silicon, and support the concept with a theoretical model based on these mechanisms. Chapter 3 will discuss the design, fabrication and characterization details of the core-shell silicon nanowire devices, explain the experimental data as well as the comparisons with the simulation results. Chapter 4 will present a new planar silicon device for investigation of a new photoresponse amplification mechanism, and discuss the critical results and findings. Chapter 5 will show the theoretical model for analyzing the gain characteristics of the device with all the necessary physical models and assumptions included. Finally, Chapter 6 will summarize this dissertation.

Chapter 2

Sub-Bandgap Light Detection Mechanism

Chapter 2 discusses the physical mechanisms of using silicon nanostructures for sub-bandgap light detection. After presenting the physical mechanisms, an analytical model for optical absorption coefficient calculation will be discussed with further details.

2.1 Design Motivation

As mentioned in Chapter 1, it is extremely difficult to realize all-silicon complementary metal-oxide-semiconductor (CMOS) compatible sub-bandgap/infrared photodetectors. The main reason is that silicon has a negligible response to infrared photons ($\lambda > 1.15\ \mu$m) with energy lower than its bandgap energy. This poses a great challenge to use silicon as an active absorbing material for infrared photon detection. Although various approaches including heterogeneous integration [27], wafer bonding [28], and defect or interfacial states absorption have been explored and investigated [29] [30], either complex fabrication techniques, material growth and integration, or low repeatability of performance hindered the development of these methods for real applications. Therefore, using silicon nanostructures due to their unique optical and electrical properties that cannot be observed in their bulk counterparts may provide a new way to increase the capability of sub-bandgap light detection of silicon. In addition

to the increased sensitivity to infrared photons the noise characteristics is expected be much better compared to other mechanisms, since these characteristics are attributed to the intrinsic properties of silicon nanostructures (e.g. core-shell silicon nanowires to be discussed in Chapter 3) rather than defect or interfacial states. The theory suggests it should also be applied to other semiconductor materials.

2.2 Sub-Band Light Detection Mechanism

2.2.1 Franz-Keldysh Effect

The design presented here integrates three physical mechanisms: the Franz-Keldysh effect, quasi-quantum confinement effect, and the impurity-state assisted photon absorption in core-shell silicon nanowire structures. Via Franz-Keldysh effect, the wavefunctions of the carriers tunnel into higher energy regions beyond the classical reflection point, thus allowing interactions with the electromagnetic radiations or photons at energies lower than the bandgap [31] – [34]. Under a high electric field due to the built-in potential or reverse bias, the edges of conduction band and valence band are tilted along the direction of the electric field. As a result, the electron and hole wavefunctions possess the characteristics of Airy functions, having a “tail” that extends into the classically-forbidden bandgap regime [35]. Because the absorption coefficient is proportional to the magnitude square of the overlap integral of the e-h wavefunctions, the presence of the tunneling tails, as illustrated in Figure 2.1 [36], significantly enhances the e-h interactions with sub-bandgap photons. A high built-in electric field

(E >10^{5-6} V/cm) over the radial core-shell p-n junction in silicon nanowires can thus be utilized to induce the above stated Franz-Keldysh effect.

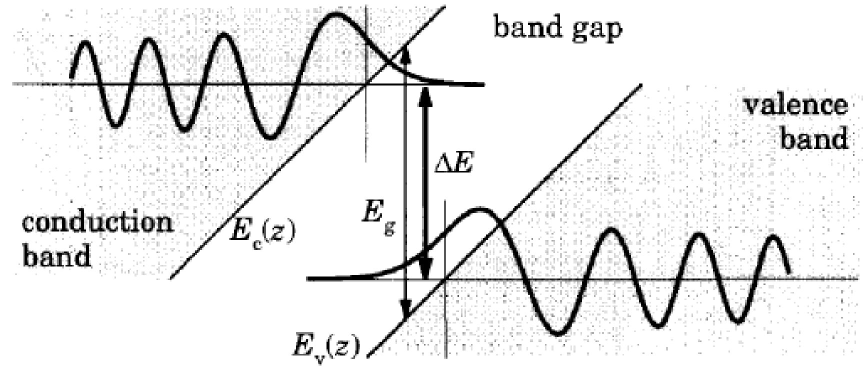

Figure 2.1: The Franz-Keldysh effect on interband absorption. The states in conduction and valence bands are separated by $\Delta E < E_g$ but the wavefunctions overlap because of the tail that tunnels into the bandgap [36].

2.2.2 Quasi-quantum Confinement Effect

To further enhance the relatively weak Franz-Keldysh effect, quantum confinement also plays an important role in the core-shell nanostructure to limit the spread of the electron wavefunctions [37]. Because the electrons in the shell region are spatially confined in the radial direction. The boundary conditions arising from the nanowire geometry force the electron wavefunctions to decay rapidly near the nanowire surface, thus increasing the probability for electrons to reach the regions near the p-n junction for enhanced value of the overlap integral between the electron and hole wavefunctions [36]. For the core-shell nanowire structures we will discuss in Chapter 3, the dimension of our concern (~ 50 - 100 nm) is greater than the dimension of

conventional quantum wells (~ 10 nm) , we call the effect quasi-quantum confinement effect instead. Our purpose here is not for energy quantization of electrons but for spatial confinement of electron wavefunctions to maximize the wavefunction overlap integral. Nevertheless, the quasi-quantum confinement produces discrete electron sub-bands of discrete energy levels. Dozens of subbands exist and the number of subbands increases with the bias voltage due to the increase in the confinement energy.

2.2.3 Impurity-state Assisted Photon Absorption

In addition to the mechanisms that maximize the e-h interactions with sub-bandgap photons, we further propose to use highly doped silicon to create a large number of impurity states to relax the k-selection rule in the momentum or $k-$space.

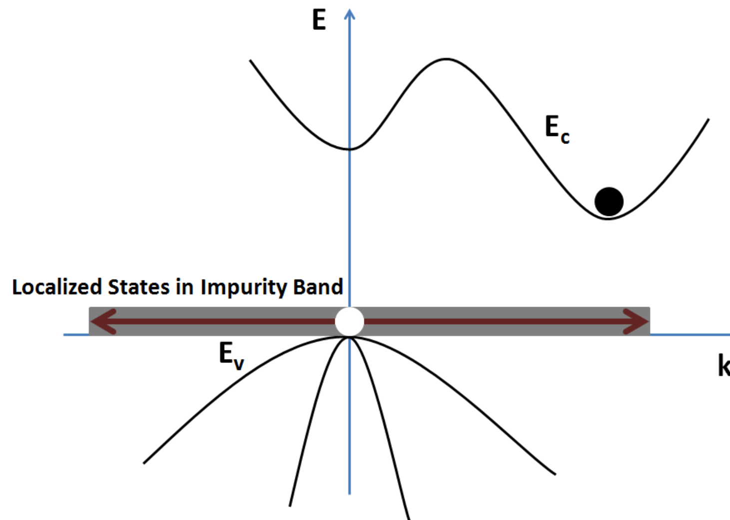

Figure 2.2: 1-D schematic of relaxation of the k-selection rule by using highly boron-doped silicon. Because of the uncertainty principle, the hole in the impurity band has a highly localized wavefunction without a well-defined crystal momentum in $k-$space.

When the average distance between the impurity atoms approaches the atomic orbital radius, an impurity band is formed above the valence band edge for p+ silicon (or similarly an impurity band is formed below the conduction band edge for n+ silicon), as shown in Figure 2.2. The mobility of the carriers in the impurity band is nearly zero, suggesting that holes in the impurity states are highly localized. As a result, the k selection rule is greatly relaxed if the optical excitation involves the impurity states, a mechanism that favors optical transition for indirect bandgap semiconductors such as silicon [1].

2.3 Analytical Modeling

In this section, we present a detailed physical model of the sub-bandgap light absorption process in core-shell silicon nanowires. The model include all the key physical mechanisms described in the previous section. Given the symmetrical properties of the nanowires, we can reduce the problem into a 1-D problem as if we take a radial slice of the core-shell structure using one-dimensional approximation.

Our treatment is based on the calculations of optical absorption coefficient using the Fermi's golden rule from the time-dependent perturbation theory. This is, of course, a simplified model but under certain operation conditions, it is expected to achieve results consistent with experimental observations.

2.3.1 Model Setup

The band diagram of the simplified 1-D model (Figure 2.3) is shown below. Along the radial direction of the p-n junction (x direction in the schematic), the slice

consists of p- and n- regions in the core-shell silicon nanowire. As discussed earlier, the most important contribution to sub-bandgap photon absorption occurs between an impurity (bound) state and a quasi 2-D state. In other words, through the absorption of a sub-bandgap photon, a quasi 2-D electron and hole in the acceptor state (or a quasi-2D hole and an electron in the donor state) would be created. These two processes are essentially similar to each other. Given the core-shell nanowire devices are fabricated using boron doped p+ silicon, the excitation processes happen between quasi-2D electrons and impurity states in the impurity band extended from the valence band.

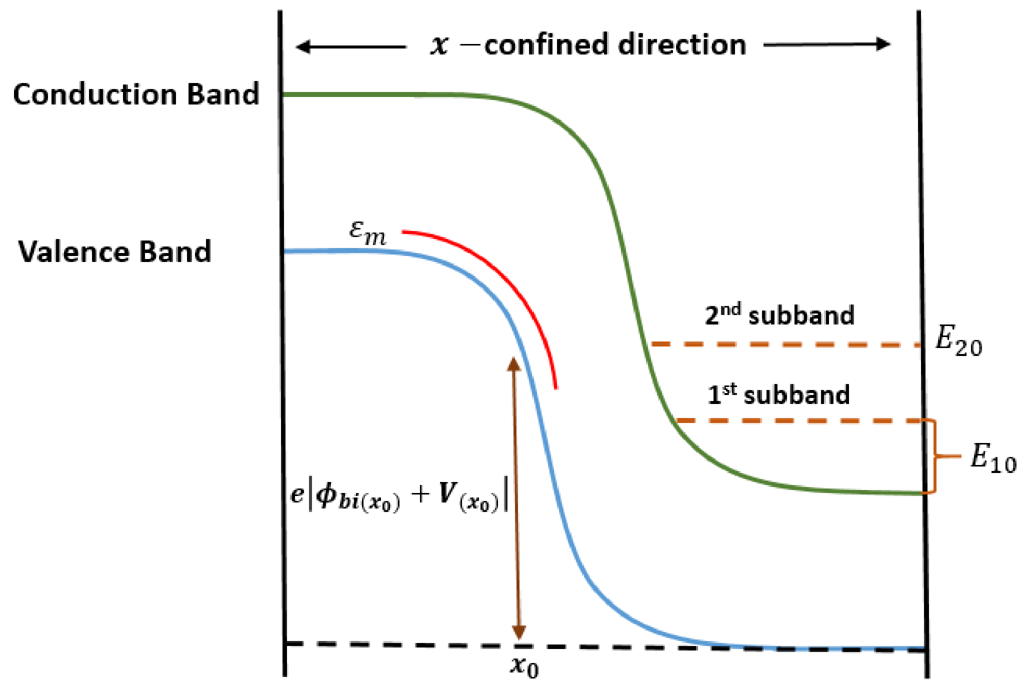

Figure 2.3: The band diagram and simplified 1-D model illustrating the sub-bandgap light absorption process in a confined p-n junction structure.

2.3.2 Absorption Coefficient Calculation

Based on the Fermi's golden rule [38], the transition rate for absorption between an initial state state $|\Psi_h\rangle$ in the impurity band with energy E_h and a final state $|\Psi_e\rangle$ in the conduction band with energy E_n can be written as:

$$w_{abs} = \frac{2\pi}{\hbar} |< \Psi_e|\hat{H}_{PO}|\Psi_h >|^2 \delta(E_n + E_h - \hbar\omega) \qquad (2.1)$$

Here $\hat{H}_{PO}$ is the perturbing Hamiltonian induced by the electromagnetic field of incoming photons using the electric dipole approximation, and $\hat{H}_{PO} = -\frac{eA_0 \exp(i\boldsymbol{k_{op}}\cdot\boldsymbol{r})}{2m_0}\boldsymbol{e}\cdot\hat{\boldsymbol{p}}$, m_0 is the free electron mass, $\hat{\boldsymbol{p}}$ is the momentum operator $-i\hbar\nabla$, **A** is electromagnetic vector potential (with a magnitude of A_0) corresponding to a wave of angular frequency ω, $\boldsymbol{k_{op}}$ is the wavevector of the optical field inside the material, and the field is linearly polarized with its electric vector in the direction (x – direction) of unit vector $\boldsymbol{e}$. Since the magnitude of $\boldsymbol{k_{op}}$ vector is much smaller than that of vectors associated with electron and holes, in the following treatment, we have ignored the k vector for photons. $\delta(E_n + E_h - \hbar\omega)$ represents the energy conservation relation. Note that here we treat holes in the same way as electrons except that the "hole energy" E_h is pointing downward in the band diagram (e.g. hole energy at the valence band edge is zero and as the hole goes deeper into the valence band the hole may possess a higher hole energy). The absorption coefficient α is the probability of absorption of a photon per unit length in the direction of light propagation (i.e. along the nanowires):

$$\alpha = \sum_n \sum_h \sum_e \frac{2\pi}{\hbar} | < \Psi_e|\hat{H}_{PO}|\Psi_h > |^2 \delta(E_n + E_h - \hbar\omega) / (\frac{I}{\hbar\omega}) \qquad (2.2)$$

where I is the optical power intensity upon the core-shell nanowire (power per unit area per second) and $\frac{I}{\hbar\omega}$ is the flux of incident photons upon the nanowires. The

subscripts n, h and e in eqn. (2.2) stand for the summations over all the electron subband levels (n), all the states $|\Psi_e\rangle$ in each electron subband (e), and all the impurity states $|\Psi_h\rangle$ (h) considering a unit volume. To get the absorption coefficient we would like to first calculate the square of matrix element $M^2 = \hbar^2 |\int_V \varphi_e^* \frac{\partial}{\partial x} \varphi_h dxdydz|^2$.

Since silicon is an indirect bandgap material and has six conduction band minima. The electron wavefunctions can be expressed as:

$$\Psi_{e,4-fold} = \frac{u_c(\vec{r}) e^{i(\vec{k}_{e\perp} - \vec{k}_{0\perp}) \cdot \vec{r}_\perp} \xi_{e,n}(x)}{\sqrt{V}} \tag{2.3}$$

$$\Psi_{e,2-fold} = \frac{u_c(\vec{r}) e^{i(\vec{k}_{e\perp}) \cdot \vec{r}_\perp} \xi_{e,n}(x) e^{-ik_0 x}}{\sqrt{V}} \tag{2.4}$$

for states with 4-fold degeneracy eqn. (2.3) and 2-fold degeneracy eqn. (2.4) respectively. Here $\vec{k}_{0\perp} = (0, \pm k_0, 0)$ or $(0,0,\pm k_0)$, and $k_0 = \frac{1.7\pi}{a}$ is the distance in k-space between the zone center and the conduction band minimum in silicon. $\xi_{e,n}(x)$ is the electron wavefunction associated with one specific subband energy level n in the x – direction. The localized impurity wavefunction can be approximated using hydrogen atom model (1s state). Since the impurity state is highly localized, the wavefunction can be written in the form of the following:

$$\Psi_h = \eta(\vec{r}, x_o) u_h(r) \tag{2.5}$$

Again, $u_h(r)$ is the usual atomic wavefunction and $\eta(\vec{r}, x_o)$ represents the spread of the impurity state in space with its physical location at x_o (distance from the center of the p^+ core). For simplicity, $\eta(\vec{r}, x_o)$ can be further approximated as:

$$\eta(x, y, z;\ x_o) = \frac{1}{(2a^*)^{3/2}} \tag{2.6}$$

The above equation is only valid if $|x - x_o| \leq a^*, |y| \leq a^*, |z| \leq a^*$ is satisfied, otherwise $\eta(x, y, z;\ x_o) = 0$, defining a^* as the Bohr radius calculated from $a^* = \frac{4\pi\epsilon\hbar^2}{m_h^* e^2}$, where the average effective hole mass of silicon m_h^* is used. Also, we assume that the impurity states have a single ionization energy $\varepsilon = 0.045$ eV above the valence band edge (e.g. in boron doped silicon) [39]. The atomic wavefunctions associated with electrons and holes can be represented as $u_c(r) = \sum_G a_G e^{i\vec{G}\cdot\vec{r}}$ and $u_v(r) = \sum_{G'} b_{G'} e^{i\overrightarrow{G'}\cdot\vec{r}}$ respectively, where $\vec{G}$ and $\overrightarrow{G'}$ are reciprocal lattice vectors. Assuming the light is incident along the nanowires, therefore the optical wave can be assumed to be linearly polarized along the x – axis, so the square of matrix element for the 4-fold degeneracy case becomes:

$$M_{4-fold}^2 = \frac{\hbar^2}{V}\Big|\sum_{\vec{G},\overrightarrow{G'}} a_G^* b_{G'} G_x' \int_V \ e^{i(\overrightarrow{G'}-\vec{G})\vec{r}} e^{i(\vec{k}_{0\perp}-\vec{k}_{e\perp})\vec{r}_\perp} \xi_{e,n}^*(x)\eta(\vec{r}, x_o)dxdydz + \int_V \ u_c^* u_v e^{i(\vec{k}_{0\perp}-\vec{k}_{e\perp})\vec{r}_\perp} \xi_{e,n}^*(x)\frac{\partial\eta(r,x_o)}{\partial x} dxdydz\Big|^2 \tag{2.7}$$

Note that the integrand in the second integral contains a fast varying function $u_c^* u_v$. Because of the atomic function for electrons and holes are orthogonal, the second integral is negligible. Therefore, eqn. (2.7) can be further reduced as:

$$M_{4-fold}^2 = \frac{\hbar^2}{V}\Big|\sum_{\vec{G},\overrightarrow{G'}} a_G^* b_{G'} G_x' \int_V \ e^{i(\overrightarrow{G'}-\vec{G})\vec{r}} e^{i(\vec{k}_{0\perp}-\vec{k}_{e\perp})\vec{r}_\perp} \xi_{e,n}^*(x)\eta(\vec{r}, x_o)dxdydz\Big|^2 \tag{2.8}$$

Similarly for the 2-fold degeneracy case the square of the matrix element becomes:

$$M_{2-fold}^2 = \frac{\hbar^2}{V}\Big|\sum_{\vec{G},\overrightarrow{G'}} a_G^* b_{G'} G_x' \int_V \ e^{i(\overrightarrow{G'}-\vec{G})\vec{r}} e^{+ik_0 x} e^{-i\vec{k}_{e\perp}\vec{r}_\perp} \xi_{e,n}^*(x)\eta(\vec{r}, x_o)dxdydz\Big|^2 \tag{2.9}$$

From eqn. (2.8) and (2.9), the integration is non-zero only when $\vec{G} = \vec{G'}$, these two equations can further be simplified into:

$$M_{4-fold}^2 = \frac{\hbar^2}{V} |\sum_G a_G^* b_G G_x|^2 \left| \int_V e^{-i(\vec{k}_{e\perp} - \vec{k}_{0\perp}) \cdot \vec{r}_\perp} \xi_{e,n}^*(x) \eta(\vec{r}, x_o) dxdydz \right|^2 \quad (2.10)$$

$$M_{2-fold}^2 = \frac{\hbar^2}{V} |\sum_G a_G^* b_G G_x|^2 \left| \int_V e^{-i\vec{k}_{e\perp} \cdot \vec{r}_\perp} e^{+ik_0 x} \xi_{e,n}^*(x) \eta(\vec{r}, x_o) dxdydz \right|^2 \quad (2.11)$$

Reorganizing the terms, let $|M_b|^2 = \hbar^2 |\sum_G a_G^* b_G G_x|^2$, the value of $|M_b|^2$ can be determined approximately by $|M_b|^2 = 1.33 m_0 E_g$ in a quantum confined system [40]. Then eqn. (2.10) and (2.11) can be expressed as:

$$M_{4-fold}^2 = \frac{|M_b|^2}{V} \left| \int_{(y-z\ plane)} e^{-i(\vec{k}_{e\perp} - \vec{k}_{0\perp}) \cdot \vec{r}_\perp} \left[\int_0^L \xi_{e,n}^*(x) \eta(\vec{r}, x_o) dx \right] dydz \right|^2 \quad (2.12)$$

$$M_{2-fold}^2 = \frac{|M_b|^2}{V} \left| \int_{(y-z\ plane)} e^{-i\vec{k}_{e\perp} \cdot \vec{r}_\perp} \left[\int_0^L \xi_{e,n}^*(x) \eta(\vec{r}, x_o) e^{+ik_0 x} dx \right] dydz \right|^2 \quad (2.13)$$

Here, L is the device dimension along the x direction. Define two functions for an impurity state at position x_o: $G'_n(y, z, x_o) = \left[\int_0^L \xi_{e,n}^*(x) \eta(\vec{r}, x_o) dx \right]$ and $G''_n(y, z, x_o) = \left[\int_0^L \xi_{e,n}^*(x) \eta(\vec{r}, x_o)\ e^{+ik_{ox} x} dx \right]$ for 4-fold and 2-fold case respectively, eqn. (2.12) and (2.13) can be rewritten as:

$$M_{4-fold}^2 = \frac{|M_b|^2}{V} |\mathcal{G}'_n(k_{e\perp}, x_o)|^2 \quad (2.14)$$

$$M_{2-fold}^2 = \frac{|M_b|^2}{V} |\mathcal{G}''_n(k_{e\perp}, x_o)|^2 \quad (2.15)$$

Here, $\mathcal{G}'_n(k_{e\perp}, x_o)$ is the 2-D Fourier transform of $G'_n(y, z, x_o)$:

$$\mathcal{G}'_n(k_{e\perp}, x_o) = \int_{(y-z\ plane)} e^{-i(\vec{k}_{e\perp} - \vec{k}_{0\perp}) \cdot \vec{r}_\perp} G'_n(y, z, x_o) dydz \quad (2.16)$$

And, $\mathcal{G}''_n(k_{e\perp}, x_o)$ is the 2-D Fourier transform of $G''_n(y, z, x_o)$:

$$\mathcal{G}''_n(k_{e\perp}, x_o) = \int_{(y-z\ plane)} e^{-i\vec{k}_{e\perp}\cdot\vec{r}_\perp}\, G''_n(y, z, x_o)dydz \tag{2.17}$$

Using the eqn. (2.2), the expression of $\hat{H}_{PO}$ and the expression of light intensity $I = \frac{1}{2}nc\varepsilon_0\omega^2 A_0^2$, the optical absorption coefficient for the 4-fold degeneracy case can be written as:

$$\alpha_{4-fold} = \frac{e^2 h|M_b|^2}{2nc\varepsilon_0 EV^2}\sum_n A\int_{x_o=0}^{L}\rho_h(E_h)dx_o \iint_{|\vec{k}_{e\perp}-\vec{k}_{0\perp}|,E_h}|\mathcal{G}'_n(k_{e\perp}, x_o)|^2\,\delta(E_n + E_h - E)(1 - f_c - f_v)\frac{2A}{(2\pi)^2}d^2(|\vec{k}_{e\perp} - \vec{k}_{0\perp}|)dE_h \tag{2.18}$$

where $\rho_h(E_h)$ is the density of states of the impurity state, and $\rho_h(E_h) = P(x_o)\delta(E-E_h)$, $\rho_h(E_h)$ is zero except when $E_h = -\varepsilon_m = -0.045$ eV, the ionization energy of the acceptor state taking the valence band edge as the energy reference level. For electrons at one specific subband energy level, using effective mass approximation the energy for the 4-fold and 2-fold degeneracy cases are:

$$E_{n-4\,fold} = E_g - e|\phi_{bi} + V| + E_{no} + \frac{\hbar^2|\vec{k}_{e\perp}-\vec{k}_{0\perp}|^2}{2m_e} \tag{2.19}$$

$$E_{n-2\,fold} = E_g - e|\phi_{bi} + V| + E_{no} + \frac{\hbar^2 k_{e\perp}^2}{2m_e} \tag{2.20}$$

where $e|\phi_{bi} + V|$ is the energy difference of the valence band with respect to the valence band edge in the charge neutral region, and E_{no} is the subband energy level with respect to the conduction band edge in the charge neutral region as illustrated in the Figure 2.3. In this case, the summation over all the transitions between the electron and impurity states have been represented using integrals instead. And the net transition rate is $1 -$

$f_c - f_v = (1 - f_c)(1 - f_v) - f_c f_v$, to be consistent with the hole energy definition that the Fermi function for holes here f_v is defined as the probability for a state to be occupied by a hole. Similarly for the 2-fold degeneracy case, we have:

$$\alpha_{2-fold} = \frac{e^2\hbar|M_b|^2}{2nc\varepsilon_0 EV^2}\sum_n A\int_{x_o=0}^{L}\rho_h(E_h)dx_o\iint_{k_{e\perp},E_h}|\mathcal{G}''_n(k_{e\perp},x_o)|^2\,\delta(E_n+E_h-E)(1-f_c-f_v)\frac{2A}{(2\pi)^2}d^2k_{e\perp}dE_h \tag{2.21}$$

Then from eqn. (2.19), (2.20) and $\delta(E_n + E_h - E)$, eqn.(2.18) and (2.21) can be further expressed as:

$$\alpha_{4-fold} = \frac{e^2\hbar|M_b|^2}{2nc\varepsilon_0 EV^2}\sum_n A\int_{x_o=0}^{L}dx_o\int_{|\vec{k}_{e\perp}-\vec{k}_{0\perp}|}\left|\mathcal{G}'_n(k_{e\perp},x_o)\right|^2 P(x_o)\delta(\varepsilon_m + E + e\left|\phi_{bi}+V\right| - E_g - E_{no} - \frac{\hbar^2\left|\vec{k}_{e\perp}-\vec{k}_{0\perp}\right|^2}{2m_e})(1-f_c-f_v)\frac{2A}{(2\pi)^2}d^2\left(\left|\vec{k}_{e\perp}-\vec{k}_{0\perp}\right|\right) \tag{2.22}$$

$$\alpha_{2-fold} = \frac{e^2\hbar|M_b|^2}{2nc\varepsilon_0 EV^2}\sum_n A\int_{x_o=0}^{L}dx_o\int_{k_{e\perp}}\left|\mathcal{G}''_n(k_{e\perp},x_o)\right|^2 P(x_o)\delta(\varepsilon_m + E + e\left|\phi_{bi}+V\right| - E_g - E_{no} - \frac{\hbar^2 k_{e\perp}^2}{2m_e})(1-f_c-f_v)\frac{2A}{(2\pi)^2}d^2k_{e\perp} \tag{2.23}$$

Now we revisit the expressions for $G'_n(y,z,x_o)$ and $G''_n(y,z,x_o)$:

$$G'_n(y,z,x_o) = \left[\int_0^L \xi_{e,n}^*(x)\eta(r,x_o)dx\right] = \xi_{e,n}^*(x)\frac{2a^*}{(2a^*)^{3/2}} \tag{2.24}$$

$$G''_n(y,z,x_o) = \left[\int_0^L \xi_{e,n}^*(x)\eta(r,x_o)\;\; e^{+ik_{ox}x}dx\right] = \xi_{e,n}^*(x_o)\frac{2\sin(k_{ox}a)}{k_o(2a^*)^{3/2}} \tag{2.25}$$

In eqn. (2.24) and (2.25), the impurity state wavefunction as discussed earlier is assumed to be:

$$\eta(x,y,z;\; x_o) = \frac{1}{(2a^*)^{3/2}} \quad (|x-x_o| \le a^*, |y| \le a^*, |z| \le a^*) \tag{2.26}$$

$$\eta(x, y, z;\ x_o) = 0 \ \text{(elsewhere)} \tag{2.27}$$

Therefore, using 2-D Fourier transform, eqn. (2.16) and (2.17) can be written as:

$$\mathcal{G}'_n(k_{e\perp}, x_o) = \xi^*_{e,n}(x_o)(2a^*)^{3/2} \frac{sin^2[(|\vec{k}_{e\perp} - \vec{k}_{0\perp}|)a^*]}{[(|\vec{k}_{e\perp} - \vec{k}_{0\perp}|)a^*]^2} \tag{2.28}$$

$$\mathcal{G}''_n(k_{e\perp}, x_o) = \xi^*_{e,n}(x_o)(2a^*)^2 \frac{sin^2[k_{e\perp}a^*]}{[k_{e\perp}a^*]^2} \left|\frac{2\sin(k_{ox}a^*)}{k_{0x}(2a^*)^{3/2}}\right| \tag{2.29}$$

Then use eqn. (2.28) and (2.29), eqn. (2.22) and (2.23) become:

$$\alpha_{4-fold} =$$

$$\frac{e^2\hbar|M_b|^2(2a^*)^3}{2nc\varepsilon_0 EL^2} \sum_n \sum_{\mathrm{x_{o(ODR)}}} \left[P(x_o)^{-\frac{1}{3}}\right] \int_{|\vec{k}_{e\perp} - \vec{k}_{0\perp}|} \left|\xi^*_{e,n}(x_o)\right|^2 \frac{sin^4[(|\vec{k}_{e\perp} - \vec{k}_{0\perp}|)a^*]}{[(|\vec{k}_{e\perp} - \vec{k}_{0\perp}|)a^*]^4} P(x_o)\delta(\varepsilon_m + E +$$

$$e\left|\phi_{bi} + V\right| - E_g - E_{no} - \frac{\hbar^2\left|\vec{k}_{e\perp} - \vec{k}_{0\perp}\right|^2}{2m_e})(1 - f_c - f_v) \frac{2}{(2\pi)^2} d^2\left(\left|\vec{k}_{e\perp} - \vec{k}_{0\perp}\right|\right) \tag{2.30}$$

$$\alpha_{2-fold} =$$

$$\frac{e^2\hbar|M_b|^2(2a^*)^4}{2nc\varepsilon_0 EL^2} \sum_n \sum_{\mathrm{x_{o(ODR)}}} \left[P(x_o)^{-\frac{1}{3}}\right] \int_{k_{e\perp}} \left|\xi^*_{e,n}(x_o)\right|^2 \frac{sin^4[k_{e\perp}a^*]}{[k_{e\perp}a^*]^4} \left|\frac{2\sin(k_{ox}a^*)}{k_{0x}(2a^*)^{3/2}}\right|^2 P(x_o)\delta(\varepsilon_m +$$

$$E + e\left|\phi_{bi} + V\right| - E_g - E_{no} - \frac{\hbar^2 k_{e\perp}^2}{2m_e})(1 - f_c - f_v) \frac{2}{(2\pi)^2} d^2 k_{e\perp} \tag{2.31}$$

Here, the integral $\int_{x_o=0}^{L} dx_o$ has been converted into summation using factor $P(x_o)^{-\frac{1}{3}}$ to replace dx_o in the integral, and ODR stands for over doped region. If $\mathcal{G}'_n(k_{e\perp}, x_o)$ and $\mathcal{G}''_n(k_{e\perp}, x_o)$ are assumed to be depend only on the magnitude but not on the direction of $\vec{k}_{e\perp}$, then $d^2\vec{k}_{e\perp}$ can be written as $2\pi k_{e\perp} dk_{e\perp}$. Next, let $u_m = \frac{\hbar^2 k_{m\perp}^2}{2m_e}$, and $d^2k_{m\perp} = 2\pi k_{m\perp} dk_{m\perp} = \frac{2\pi m_e}{\hbar^2} du_m$. $k_{m\perp} = \left|\vec{k}_{e\perp} - \vec{k}_{0\perp}\right|$ for the 4-fold degeneracy case, and $k_{m\perp} = k_{e\perp}$ for the 2-fold degeneracy case. And for both two cases $k_{m\perp}$ can be represented by:

$$k_{m\perp} = \frac{\sqrt{2m_e}}{\hbar}(\varepsilon_m + E + e|\phi_{bi} + V| - E_g - E_{no}) \tag{2.32}$$

We can further rewrite the δ function in eqn. (2.30) and (2.31): $\delta\left(\varepsilon_m + E + e|\phi_{bi} + V| - E_g - E_{no} - \frac{\hbar^2 k_{m\perp}^2}{2m_e}\right) = \delta(\varepsilon_m + E + e|\phi_{bi} + V| - E_g - E_{no} - u_m)$. Therefore the absorption coefficients can be written as:

$$\alpha_{4-fold} = \frac{e^2 h|M_b|^2(2a^*)^3}{2nc\varepsilon_0 EL^2} \sum_n \sum_{\mathrm{x_{o(ODR)}}} \left[P(x_o)^{-\frac{1}{3}}\right] \int_{u_m} \left|\xi_{e,n}^*(x_o)\right|^2 \frac{sin^4[k_{m\perp}a^*]}{[k_{m\perp}a^*]^4} P(x_o)\delta(\varepsilon_m + E + e|\phi_{bi} + V| - E_g - E_{no} - u_m)(1 - f_c - f_v)\frac{2}{(2\pi)^2}\frac{2\pi m_e}{\hbar^2} du_m \tag{2.33}$$

$$\alpha_{2-fold} = \frac{e^2 h|M_b|^2(2a^*)^4}{2nc\varepsilon_0 EL^2} \sum_n \sum_{\mathrm{x_{o(ODR)}}} \left[P(x_o)^{-\frac{1}{3}}\right] \int_{u_m} \left|\xi_{e,n}^*(x_o)\right|^2 \frac{sin^4[k_{m\perp}a^*]}{[k_{m\perp}a^*]^4} \left|\frac{2\sin(k_{ox}a^*)}{k_{0x}(2a^*)^{3/2}}\right|^2 P(x_o)\delta(\varepsilon_m + E + e|\phi_{bi} + V| - E_g - E_{no} - u_m)(1 - f_c - f_v)\frac{2}{(2\pi)^2}\frac{2\pi m_e}{\hbar^2} du_m \tag{2.34}$$

Utilizing δ function in eqn. (2.33) and (2.34), we get the following:

$$\alpha_{4-fold} = \frac{e^2 m_e|M_b|^2(2a^*)^3}{nc\varepsilon_0 m_0^2 E\hbar L^2} \sum_{\mathrm{x_{o(ODR)}}} P(x_o)^{\frac{2}{3}} \sum_n \left|\xi_{e,n}^*(x_o)\right|^2 \frac{sin^4[k_{m\perp}a^*]}{[k_{m\perp}a^*]^4}(1 - f_c - f_v) \tag{2.35}$$

$$\alpha_{2-fold} = \frac{e^2 m_e|M_b|^2(2a^*)^4}{nc\varepsilon_0 m_0^2 E\hbar L^2} \sum_{\mathrm{x_{o(ODR)}}} P(x_o)^{\frac{2}{3}} \sum_n \left|\xi_{e,n}^*(x_o)\right|^2 \frac{sin^4[k_{m\perp}a^*]}{[k_{m\perp}a^*]^4} \left|\frac{2\sin(k_{ox}a^*)}{k_{0x}(2a^*)^{3/2}}\right|^2 (1 - f_c - f_v) \tag{2.36}$$

For both two cases, we need to sum over all the subbands n that satisfies:

$$E_{no} \le E + \varepsilon_m - E_g + e|\phi_{bi} + V| \tag{2.37}$$

Using eqn. (2.35) and (2.36) one can calculate the optical absorption coefficient to optical radiation with photon energies of $E = \hbar\omega$ for a specific confined structure if the confined one-dimensional electron wavefunction and its associated subband energy

level are known. Numerical calculation (using MATLAB) results of the core-shell silicon nanowires will be presented in Chapter 3 as an example in comparison with experimental results.

2.4 Conclusion

This chapter introduced the concept of enabling silicon to detect sub-bandgap photons and presented the physical mechanisms that behind the design. An analytical model and derivations of optical absorption coefficient based on these physical mechanism have been discussed.

This chapter, in part, is a reprint of material as it appears in the following publication: Yuchun Zhou, Yu-hsin Liu, James Cheng and Yuhwa Lo, "Bias dependence of sub-bandgap light detection for core-shell silicon nanowires", Nano Letters, 12, 5929-5935 (2012). The dissertation author was the primary investigator and author of this material.

Chapter 3

Core-shell Nanowire Device Design, Fabrication and Characterization

Chapter 3 provides a detailed description of the core-shell silicon nanowire device design for sub-bandgap light detection and the fabrication steps with critical details. The experimental setup and device characterization results are further presented with physical explanations.

3.1. Nanowire Device Design

In order to realize a device structure that can effectively incorporate all three physical mechanisms described in Chapter 2 that facilitate sub-bandgap optical absorption, we fabricated vertically arrayed p-core and n-shell silicon nanowires. The device is fabricated starting from a boron-doped p^+-Si wafer with a doping concentration ~ 10^{19} cm^{-3}. Due to the introduction of abundant localized impurity states, we augment the uncertainty in the momentum space according to the uncertainty principle. The probability for optical absorption is drastically enhanced when the uncertainty reaches the difference between the conduction band minimum and the valence band minimum. In order others, through using highly doped silicon the

mechanism of impurity-state assisted photon absorption can be utilized. A proximity solid-state diffusion method is used to convert the shell of the boron-doped silicon nanowires into n-type. The inherent nanowire geometry also ensures an increased wavefunctions overlap through the Franz-Keldysh effect and the quasi-quantum confinement effect.

3.2. Device Fabrication

The arrayed core-shell silicon nanowire device fabrication steps are illustrated schematically in Figure 3.1. As discussed earlier, the device is fabricated starting from a boron-doped p^+-Si wafer with a doping concentration ~ 10^{19} cm^{-3}.

The first step was to define the nanowire array geometry using electron-beam lithography. A 30 × 30 nickel-disk array (pitch is fixed at 1 μm) with the diameter of nanowires varying from 240 to 360 nm was finally realized on top of the p^+-Si wafer (Figure 3.1(a)). Having electron-beam lithography patterned nickel-disk arrays on top of the wafer as etch mask, nanowires with a height of 2.5 μm were etched anisotropically using the ICP-RIE dry etch process with C_4F_8 and SF_6 gases (Oxford P-100), the RIE power is 30 W and the ICP power is 1200W. To ensure the morphology of the nanowire sidewalls, the etch rate is controlled at around 5 – 6 nm/s. After the formation of p^+-nanowires, the nickel disks were removed by standard wet etch process using the nickel TFB etchant (Figure 3.1(b)).

Next, the proximity diffusion method is used to create the core-shell structures. In order to perform the diffusion process, a source wafer was prepared first by placing

the wafer into the buffered oxide etch (6:1 NH_4F: HF) solution to remove the native oxide for around 90s.

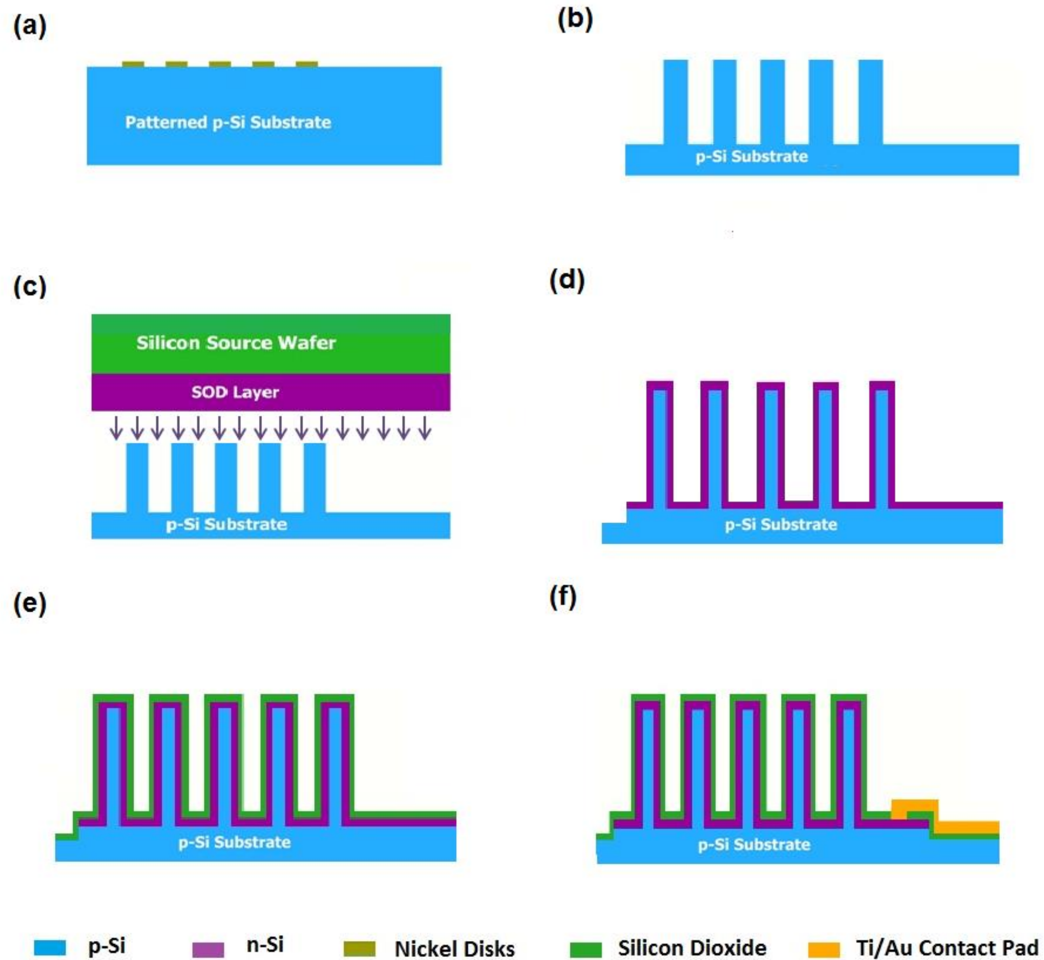

Figure 3.1: Process flow for the core-shell silicon nanowire photodetector.

After the BOE etch, a phosphorous-containing spin-on-dopant (SOD) solution (from Filmtronics, Inc.) is spin-coated on a separate silicon wafer at 4000 rpm for 10 seconds, followed by a standard baking process at 200 ℃ for 15 minutes. And the nanowire sample was cleaned using 2% hydrofluoric acid and DI water before the diffusion process. The SOD-coated wafer was then placed as a dopant source above the

wafer with nanowire structures. The two wafers were separated by a distance of around 1 mm using quartz spacers and loaded into a rapid-thermal-annealing (RTA) furnace. The diffusion was then carried out at 950 ℃ for 35 seconds, during which the phosphorous atoms evaporate from the source wafer and precipitate on and diffuse into the nanowires, and p-core/n-shell nanowire structures were formed. After the diffusion process, a diluted 2% HF solution was used to remove the SOD residues on the nanowires (Figure 3.1(c)).

After the formation of core-shell nanowires, another dry etch step was performed to create mesa structures for electrical isolation between nanowire arrays. First, a 1 μm of SiO_2 was deposited on the sample wafer using Oxford plasma PECVD system. Positive photoresist S-1818 was used to pattern the SiO_2 layer. The photoresist was spun at 3500 rpm to get a nominal thickness of 1.5 μm. The next steps were standard soft bake at 115 ℃ for 90s and UV exposure using Karl Suss MA6 mask aligner at 11 mW/cm^2 for 20s. The resist was then developed using commercial developer Microposit MF-321 for 45s followed by hard bake at 115 ℃ for 180s. To remove any resist residues, 30s O_2 descum at 200 mTorr flow and 200 W power was performed after the development. The realized mesa pattern spans 35 μm × 46 μm each right on top of the nanowire array. The sample was then transferred into Oxford P-80 dry etching machine, where the SiO_2 layer was etched with S1818 as an etch mask using CHF_3 and Ar as reacting gases. After the dry etch, the photoresist was removed using solvents and the sample was put back again in the Oxford P-100 dry etch system for the silicon mesa etch. This time, the SiO_2 layer was used as the etch mask for the silicon mesa etch.

Using the same recipe for the nanowire etch, a 320 nm high mesa structure was formed (Figure 3.1(d)). The SiO_2 mask was further removed after the mesa etch by the buffered oxide etch (BOE). Now 320 nm high mesa structures spanning 35 μm × 46 μm each have been created. And there are a total of 900 nanowires in a 30 × 30 array (1 μm in pitch) on each device mesa. Another layer of SiO_2 ~ 250 nm is deposited again using PECVD for n-contact windows patterning (Figure 3.1(e)). NR9-3000PY was used to pattern the layer. The photoresist was spun at 2500 rpm for 40s to get a nominal thickness of 3 um. The next steps were standard prebake at 150 ℃ for 150s and UV exposure using Karl Suss MA6 mask aligner at 11 mW/cm^2 for 9s. For negative resist, a post exposure bake is done at 100 ℃ for 60 – 90s, and then the resist is developed using commercial developer Futurrex RD6 for 20s. After patterning the resist, 30 nm Ti and 100 nm Au was deposited using Temescal BJD 1800 electron beam evaporator at rate of about 1 – 1.5 Å/s. The purpose of the 30 nm Ti layer was to provide better adhesion of the gold layer to the silicon substrate. Then metal lift off was performed to remove the photoresist using Acetone, IPA and DI water. For efficient lift off, the resist thickness should be at least three times of the total metal thickness, so that the solvents can attack the photoresist beneath the metal readily. The reason why electron beam evaporation was utilized instead of sputtering or other metal deposition techniques was that the directionality of this process is relatively much better. This is critical to avoid severe sidewall deposition which could block the photoresist and hinder the lift off process. After the contact windows were filled with Ti/Au, another similar step of photolithography and patterning using NR9-3000 was performed for metal Ti/Au fingers that connects the metal contact pads away from the optical active regions to the

device. For the Ti/Au finger and contact pads the thickness of Ti was chosen to be 50 nm and Au to be 200 nm (Figure 3.1(f)). The sample was then soaked in acetone overnight without sonication due to the fact that the nanowires are fragile and might be destroyed easily during the sonication. After the liftoff, to make a back side contact indium solder was pasted on the backside of the substrate. A backside metallization could also be done as well for this purpose. And the p-contact on the backside is shared by all the devices on the substrate. For comparisons of device characteristics, planar devices of the same sized mesa without the nanowire array were also fabricated.

(a)

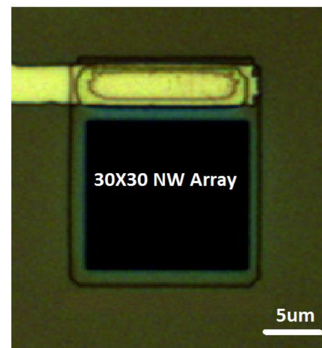

(b)

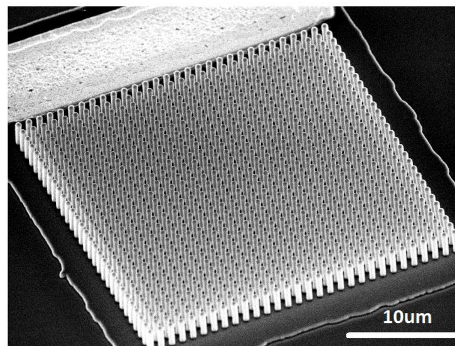

Figure 3.2: (a) –(c) Optical and SEM images of a fabricated core-shell silicon nanowire device.

(c)

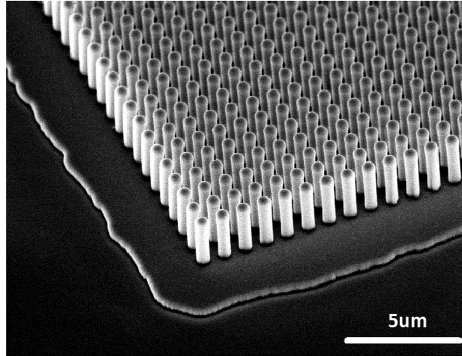

Figure 3.2: (a) –(c) Optical and SEM images of a fabricated core-shell silicon nanowire device (continued).

The images of an accomplished device are shown in Figure 3.2. Figure 3.2(a) shows the bright-field optical microscopic image of the device using a 50 × objective lens. The nanowire area appears to be much darker than the surrounding Si area, manifesting the effect of photon trapping. Figure 3.2(b) and (c) show the SEM images of a full device and a zoomed-in view of the nanowires near the edge of the mesa.

3.3. Device Characterization

3.3.1. Experimental Setup

A brief overview of the experimental setup including electrical and optical components is depicted in Figure 3.3. The sample was placed on top of a sample stage that is connected to a commercial parameter analyzer (Agilent 4155B). The laser sources for the measurements are either 1054 nm (Advanced Laser Diode Systems-PiL106) or 1310 nm (Eudyna FLD3F7CZ) infrared lasers. To illuminate the sample, a

10/90 beam splitter was placed between the focus lens and the laser output for the purpose of measuring the output power simultaneously using the optical power meter (Newport 1830-C).

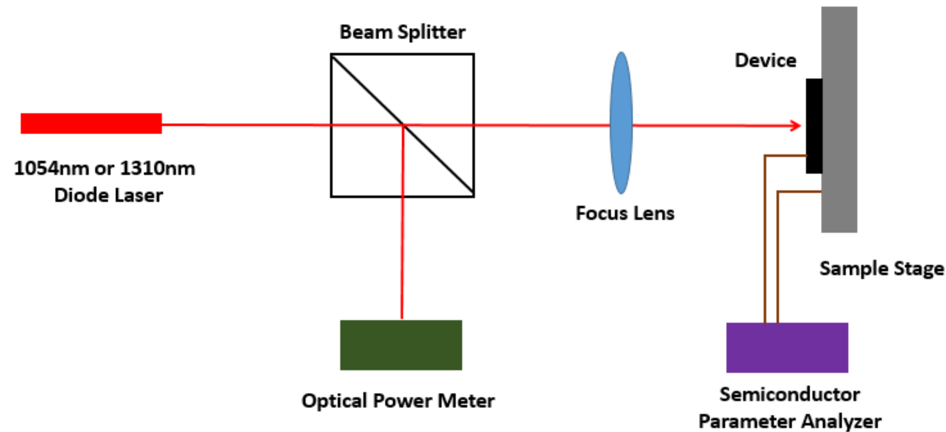

Figure 3.3: Overview schematic of the measurement setup.

3.3.2. Photoresponse Measurement Results

Using the experimental setup shown in Figure 3.4, the current–voltage characteristics were measured on the nanowire device fabricated through the aforementioned processes. The dark I – V characteristics of a 340 nm-diameter nanowire device is shown in Figure 3.5 as an example, where a clear rectifying behavior was observed. By fitting the forward bias regime using the Shockley's diode equation [41], an ideality factor of ~ 1.71 was obtained (Figure 3.5(b)). In the reverse bias region, the dark current is 10.5 nA under 1.5 V reverse bias. A slightly faster increase in dark current at reverse bias greater than 1.0 V is mostly caused by the increase of the depletion width where most dark current contributing carriers are generated by thermal

excitation. Moreover, devices with smaller nanowire diameters also exhibited lower dark current values, for example, 6.9 nA for a 240 nm-diameter nanowire device at 1.5 V reverse bias. The typical I–V characteristics of p-n junctions demonstrated the successful fabrication of radial core-shell silicon p-n junctions using the proximity diffusion method described in Section 3.2.

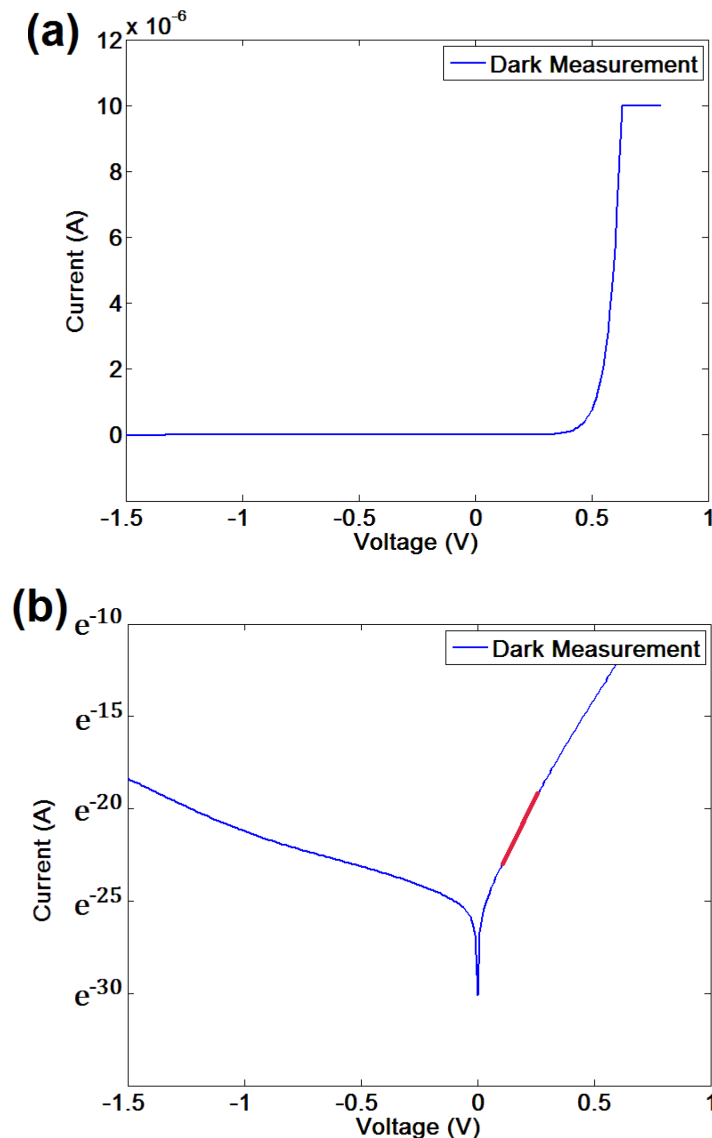

Figure 3.4: (a) Dark current-voltage characteristics of the fabricated arrayed silicon nanowires showing typical rectifying behavior of p-n junctions. (b) Log scale plot of the I-V plot with the extraction of the ideality factor n = ~1.71.

Using the experimental setup shown in Figure 3.4, the current–voltage characteristics were measured on the nanowire device fabricated through the aforementioned processes.

The devices were tested for their photoresponses to infrared photons using 1054 and 1310 nm laser sources. The photon energy of 1054 nm light is slightly above the bandgap energy of Si (~ 1100 nm) at room temperature, while that of 1310 nm light is well below the bandgap of silicon. Figure 3.6(a) and 3.6(b) represent the measurement results of core-shell Si nanowires for optical signals at 1054 nm and 1310 nm, respectively. There exists a noticeable difference in the voltage dependence of photoresponse at these two wavelengths. For sub-bandgap photon detection (1310 nm), the photoresponse increases rapidly with the reverse bias voltage. Such phenomenon was not observed when the excitation wavelength (e.g. 1054 nm) is slightly above the bandgap energy. Based on the model discussed already in Chapter 2, we found that such large differences in voltage-dependent photoresponses are directly resulted from our design using the three aforementioned physical mechanisms – the Franz-Keldysh effect, the quasi-quantum confinement effect and the impurity state assisted photon absorption. Both the Franz-Keldysh effect and the quasi-quantum confinement effect increase the overlap integral between electron and hole wavefunctions. Most importantly, the number of electron subbands increases with the bias voltage due to the increase in the confinement energy. The large number of impurity states is introduced directly by using the highly boron-doped silicon as the starting material for device fabrication and the k-selection rule would be relaxed accordingly to utilize the impurity state assisted photon absorption in silicon.

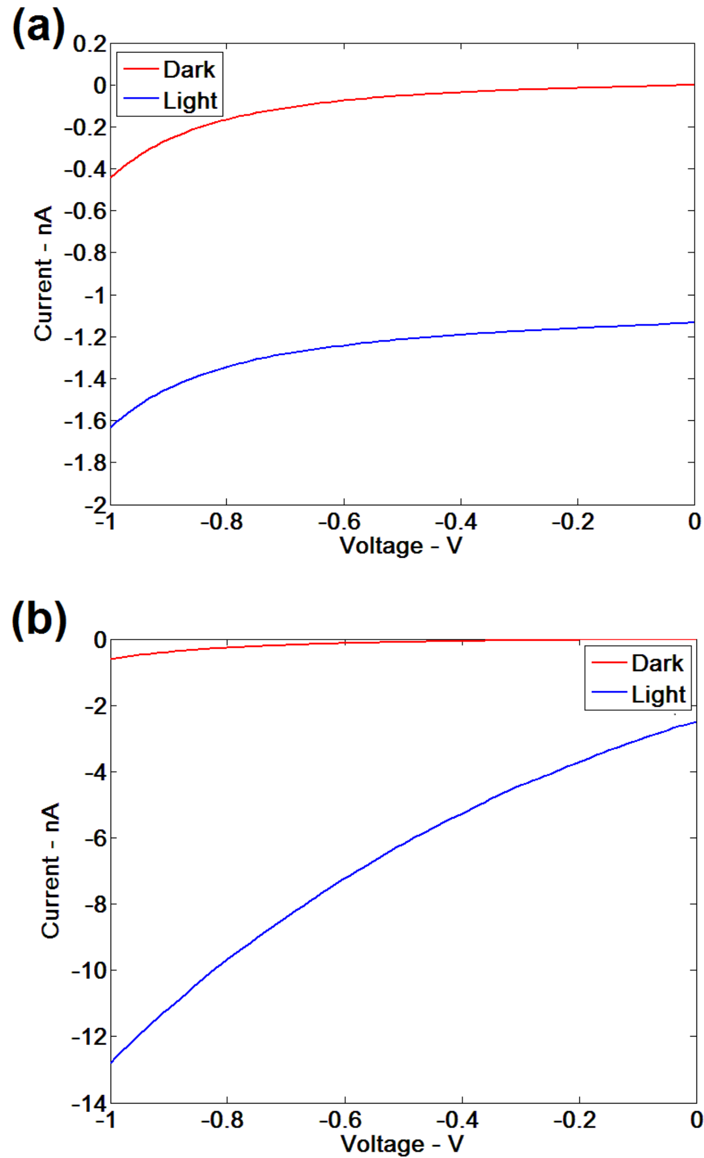

Figure 3.5: (a) Dark and light measurements in the reverse bias region at 1054 nm. (b) Dark and light measurements in the reverse bias region at 1310 nm. Note the very different voltage-dependent behaviors of photocurrent in the reverse bias region. The photoresponse increases rapidly with the reverse bias only for sub bandgap (1310 nm) photons.

Furthermore, in order to extract the absorption directly from the nanowires at 1310 nm, comparisons between the planar device without nanowires and the device with

nanowires have been made under the same measurement conditions, as illustrated in Figure 3.7.

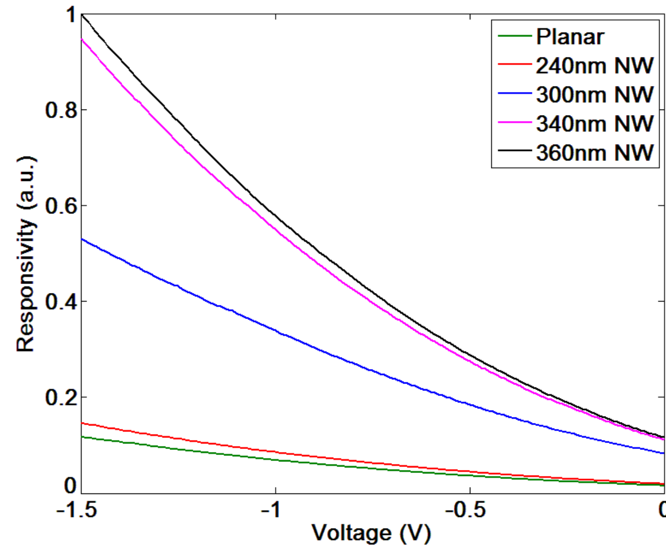

Figure 3.6: Measured photo-responsivity of the nanowire devices and the planar device.

Although earlier studies have shown that nanowire arrays exhibiting enhanced absorption at visible and UV wavelengths due to the waveguiding effects caused by the large index difference between semiconductor nanowires and materials between nanowires, optical simulations show that such waveguiding effects have negligible influence on nanowires that are only 2.5 μm high at 1310 nm. Therefore, for our nanowire device with a very low fill factor the waveguiding effect is negligible. And we could use the following procedure to calculate the true nanowire photoresponse to 1310 nm light. Over the mesa area that contains a nanowire array, the net photoresponse is the sum of the response of the nanowires and that of the planar area not covered by the nanowires (including those areas between the nanowires). We define R_{NW} as the

photo-responsivity of nanowires, $R_{PlanarM}$ as the photo-responsivity of the planar structure (which also equals to the measured photo-responsivity of the device without nanowires), and R_M as the measured photo-responsivity from the device that contains both nanowires and planar area. Assume A is the total optically active area over the mesa and $a = 30 \times 30 \times \pi \times (\frac{d}{2})^2$ is the area occupied by the 30×30 nanowire array, where d the diameter of the core-shell nanowire is (equals to 240, 300, 340, and 360 nm). Using the above definitions, the following equation of photocurrent for a nanowire device under illumination, assuming P is the optical power density (unit: W/cm^2):

$$R_{NW} \times P \times a + R_{PlanarM} \times P \times (A - a) = R_M \times P \times A \quad (3.1)$$

The actual photo-responsivity of the nanowires R_{NW} can then be extracted from the measured results of $R_{PlanarM}$ and R_M shown in Figure 3.7 and expressed as:

$$R_{NW} = (R_M - R_{PlanarM}) \times \frac{A}{a} + R_{PlanarM} \quad (3.2)$$

The calibrated results of R_{NW} are shown in Figure 3.8. Note that the sub-bandgap photo-responsivity at 1310 nm of core-shell nanowires is nearly two orders of magnitude stronger than that of the planar structure. It can also be seen that nanowires having larger diameters exhibit larger photoresponses, and nanowires having diameters less than 240 nm do not show p-n junction characteristics, signifying that the entire p-doped core is turned into n-type due to the phosphorous diffusion. Also the responsivity of the 360 nm nanowire is slightly lower than that of the 340 nm case, indicated that there exists an optimal core-shell thickness relation giving rise to the highest sub-bandgap photoresponse.

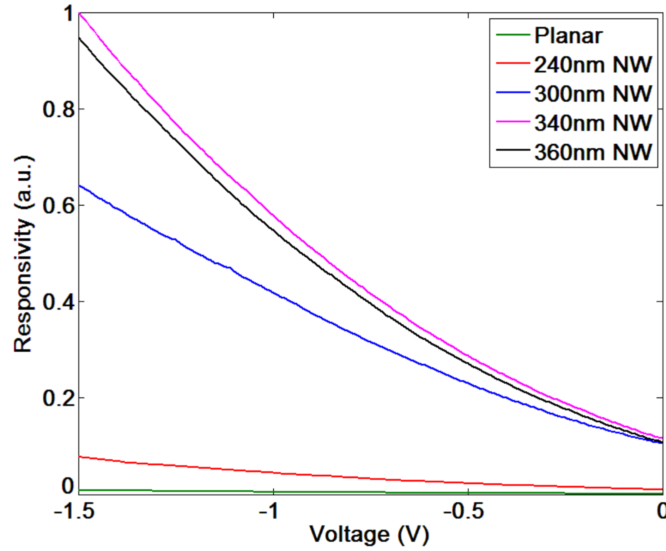

Figure 3.7: Photo-responsivities of the nanowires with various diameters and the planar structure obtained from calibrated calculations.

3.3.3. Numerical Simulation Results

Besides the experimental characterizations of the nanowires, we further performed numerical calculations of the absorption coefficient of the nanowires using the model discussed in Chapter 2. The simulation considers a 300 nm-diameter nanowire structure with a height of 2.5 µm. We assume the inner core has a radius of 66 nm and the shell has a thickness of 84 nm as illustrated in Figure 3.9. Since the core-shell structure is formed by the rapid thermal diffusion, the p-type doping concentration of the core is equal to the concentration of the p-substrate (10^{19} cm^{-3}), and the effective n-shell doping concentration used in the simulation is assumed to be 2×10^{17} cm^{-3}. Note that although the actual impurity level of the n-shell should be rather high to overcompensate the background doping of the p-Si, the surface states pin the Fermi-

level and trap most of the electrons to the surface states, leaving an effective electron concentration to be around 2×10^{17} cm^{-3}.

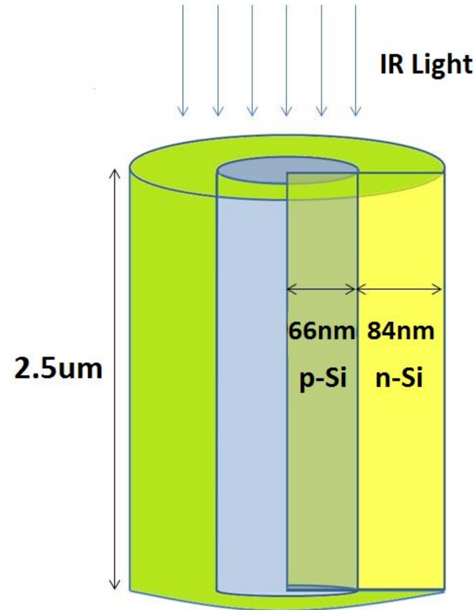

Figure 3.8: Schematic of the simulated structure and the range of p-core and n-shell, respectively.

As described above, the sub-bandgap photon absorption originates from the interactions between the wavefunction of electrons in the n-shell and the wavefunction of impurity states (holes) and our model considers optical transitions between confined electrons and holes in the localized impurity states for a core/shell p^+-n Si nanowire structure under the reverse bias. The simulation starts with the calculations of the overlap integral of wavefunctions between the impurity states and electrons using one-dimensional approximations as if we take a radial slice of the core-shell structure (Figure 3.10). Recall eqn. (2.35) and (2.36) in Chapter 2:

$$\alpha_{4-fold} = \frac{e^2 m_e |M_b|^2 (2a^*)^3}{nc\varepsilon_0 m_0^2 E\hbar L^2} \sum_{\mathrm{x_{o(ODR)}}} P(x_o)^{\frac{2}{3}} \sum_n \left|\xi_{e,n}^*(x_o)\right|^2 \frac{sin^4[k_{m\perp}a^*]}{[k_{m\perp}a^*]^4} (1 - f_c - f_v) \tag{3.3}$$

$$\alpha_{2-fold} = \frac{e^2 m_e |M_b|^2 (2a^*)^4}{nc\varepsilon_0 m_0^2 E\hbar L^2} \sum_{\mathrm{x_{o(ODR)}}} P(x_o)^{\frac{2}{3}} \sum_n \left|\xi_{e,n}^*(x_o)\right|^2 \frac{sin^4[k_{m\perp}a^*]}{[k_{m\perp}a^*]^4} \left|\frac{2\sin(k_{ox}a^*)}{k_{0x}(2a^*)^{3/2}}\right|^2 (1 - f_c - f_v) \tag{3.4}$$

In this case, the over-doped region (ODR) covers from the center of the nanowire to the nanowire surface ($0 < x_o < 150$ nm). Due to the device geometry and the p-type doping concentration (1×10^{19} cm^{-3}), the distance between impurities along the x-direction can be approximated as ~ 4.7 nm and we assume all the impurity states are equally spaced.

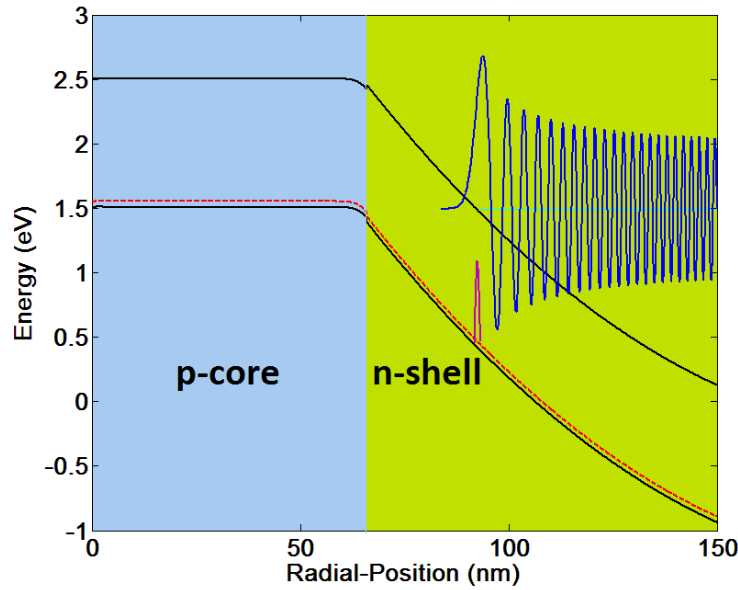

Figure 3.9: The concept of sub-bandgap photon absorption illustrating the interaction between a confined electron wave function (blue) and a localized impurity state wavefunction (red) in a core-shell silicon nanowire at 1.5 V reverse bias.

Using eqn. (3.3) and (3.4) and the electron wavefunction associated with each specific subband energy level in the x-direction were obtained from commercial software

SILVACO Atlas using one-dimensional approximations, the calculated absorption coefficient for the nanowire structure turns out to be 13 cm^{-1} at 0 V and 68.2 cm^{-1} at -1.5 V, respectively. Furthermore, the voltage dependence of photoresponse exhibits an excellent agreement between the experimental data and the theoretical calculations, as shown in Figure 3.11. The results in Figure 3.11 are normalized because it is difficult to measure the exact value of absorption coefficient of core-shell nanowires precisely. Since our physical model contains no fitting parameter, the good agreement with the experimental data gave us confidence in the calculated absorption coefficient for core-shell silicon nanowires.

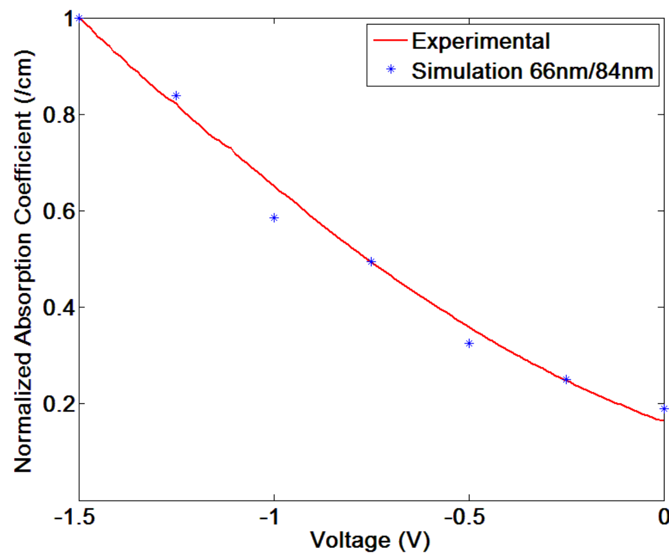

Figure 3.10: Comparisons between experimental data and simulation results of the 300-nm diameter nanowires assuming the diffused p-n junction has a 1×10^{19} cm^{-3}/2×10^{17} cm^{-3} effective doping level and a core/shell radius of 66 nm/84 nm.

Although the current diffusion process produced a relatively low effective n-shell doping due to the Fermi-level pinning by the surface states, the physical model

predicts very significant enhancement of the absorption coefficient with the increasing doping concentration of the n-shell region, which may be achieved with epitaxial growth or passivation of the surface states. Figure 3.12 shows the calculated absorption coefficient dependence on the doping level of n-shell using the same p-doped core (10^{19} cm^{-3}). The results show that the absorption coefficient of Si core-shell nanowires at 1310 nm can reach 313.1 cm^{-1} at 0 V and 582.0 cm^{-1} at -1.5 V. The increase in zero-bias absorption with the doping level of n-shell is particularly dramatic (over 30 ×). Thus, by increasing the n-shell doping to $10^{18\text{-}19}$ cm^{-3}, we expect to achieve highly efficient Si nanowire IR detectors as well as photovoltaic devices.

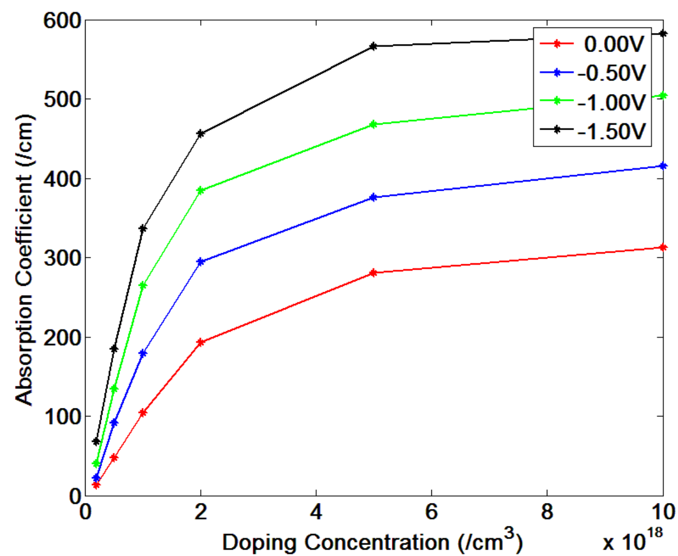

Figure 3.11: Calculated absorption coefficient dependence on the effective doping concentration in the n-shell region of a nanowire under different reverse bias conditions.

3.4. Conclusion

This chapter presented the details of the core-shell silicon nanowire device design as well as details of the critical fabrication steps. The experimental setup was

described with detail electrical and optical arrangements and the procedure of the measurements. Finally both the measurement and simulation results were presented and the comparisons between the two sets of the data were performed and discussed.

This chapter, in part, is a reprint of material as it appears in the following publications: Yuchun Zhou, Yu-hsin Liu, James Cheng and Yuhwa Lo, "Bias dependence of sub-bandgap light detection for core-shell silicon nanowires", Nano Letters, 12, 5929-5935 (2012); Yu-hsin Liu, Yuchun Zhou, and Yuhwa Lo, "High efficiency silicon 1310 nm detector without defect states or heteroepitaxy", Applied Physics Letters, 103, 041119 (2013). The dissertation author was the primary/secondary investigator and author of these materials.

Chapter 4

Cycling Excitation Process (CEP) in Silicon P-N Junctions

This chapter will describe the experimental observation of a new photoresponse amplification mechanism in heavily doped, partially compensated silicon p-n junction devices. Device fabrication, measurement and simulation results will be presented. Finally, the physical process behind the gain mechanism will be discussed.

4.1. Internal Gain Mechanism

Signal amplification is a fundamental process for all electronic and optoelectronic systems. The underlining physics of any signal amplification mechanisms is built upon the complex interactions among electrons, photons, phonons, and excitons. Improved understanding of these physical processes has spurred the enhancement of the quality of the obtained signals and fueled the development of new generations of electrical and photonic devices for communications, computation, imaging, and photovoltaics.

Broadly speaking, signal amplification can be divided into two groups – an external process that uses transistor amplifiers and an internal process that uses the

intrinsic material properties to amplify the signals. The best sensitivity or the highest signal-to-noise ratio has usually been obtained from the combination of the two amplification mechanisms. Avalanche multiplication due to impact ionization has been known to be the primary internal mechanism for signal amplification in semiconductors to date [15] – [22]. Therefore, most of the state-of-the-art photoreceivers for telecommunications and single-photon avalanche diodes (SPADs) for quantum communications and imaging have adopted the impact ionization mechanism.

However, conventional impact ionization usually requires high bias voltage, typically 30 to 200 V depending on the applications and the semiconductor materials, and often suffers from high excess noise associated with the avalanche process. Because of the very high operation voltage, avalanche multiplication by impact ionization is incompatible with the mainstream complementary metal-oxide-semiconductor (CMOS) process, and imposes serious limits on the power consumption and the level of integration (e.g. number of pixels for imaging applications). In spite of these limitations, avalanche multiplication remains to be the only viable internal signal amplification mechanism for semiconductor devices over the past few decades because of the lack other alternatives.

Here, a new gain mechanism that occurs at much lower bias than impact ionization and favors room temperature over cryogenic temperature in heavily doped and compensated silicon p-n junctions will be discussed in detail in the following sections.

4.2. CEP Device Design and Fabrication

In order to obtain a clear understanding and demonstration of the gain mechanisms, a simple mesa device structure has been selected for the investigation of the device characteristics. To achieve the heavily doped and highly compensated silicon p-n junction, a similar solid state proximity diffusion method described in Chapter 3 has been utilized to convert the top layer of a highly doped (e.g. boron doped ~ 8×10^{18} cm^{-3}) silicon wafer into n-type silicon. During the process, phosphorous was introduced via the diffusion at 950°C for 35s in a rapid thermal annealing (RTA) furnace using the phosphorous containing spin-on-dopant (SOD) as the dopant source [42]. The formed junction depth is around 100 nm, as confirmed by the secondary ion mass spectroscopy (SIMS) profile shown in Figure 4.2. After which, individual p-n junctions were formed by inductively coupled plasma reactive-ion etching (ICP-RIE, Oxford P-100) with C_4F_8 and SF_6 gases. Each device mesa has an area of 35 μm × 55 μm and is 350 nm deep. After the mesa etch, a thin layer of SiO_2 ~ 250 nm was deposited using PECVD and patterned lithographically (Karl Suss MA-6) for n- and p- metal contacts. E-beam (Temescal BJD 1800) evaporated Ti/Au (50nm/200nm) was used to form the Ohmic contacts for both n- and p- layers through the contact windows respectively (inset of Figure 1(a)). For comparisons, the same sized mesa devices were fabricated using an OMCVD (organometallic chemical vapor deposition) grown p-n junction on top of a silicon wafer. Using semiconductor parameter analyzer (Agilent 4500B), typical p-n junction current-voltage characteristics were obtained from both samples. Specifically, the diffused p-n junction device has an ideality factor of 1.98 and a leakage current of 85 pA at 1V reverse bias as shown in Figure 1.

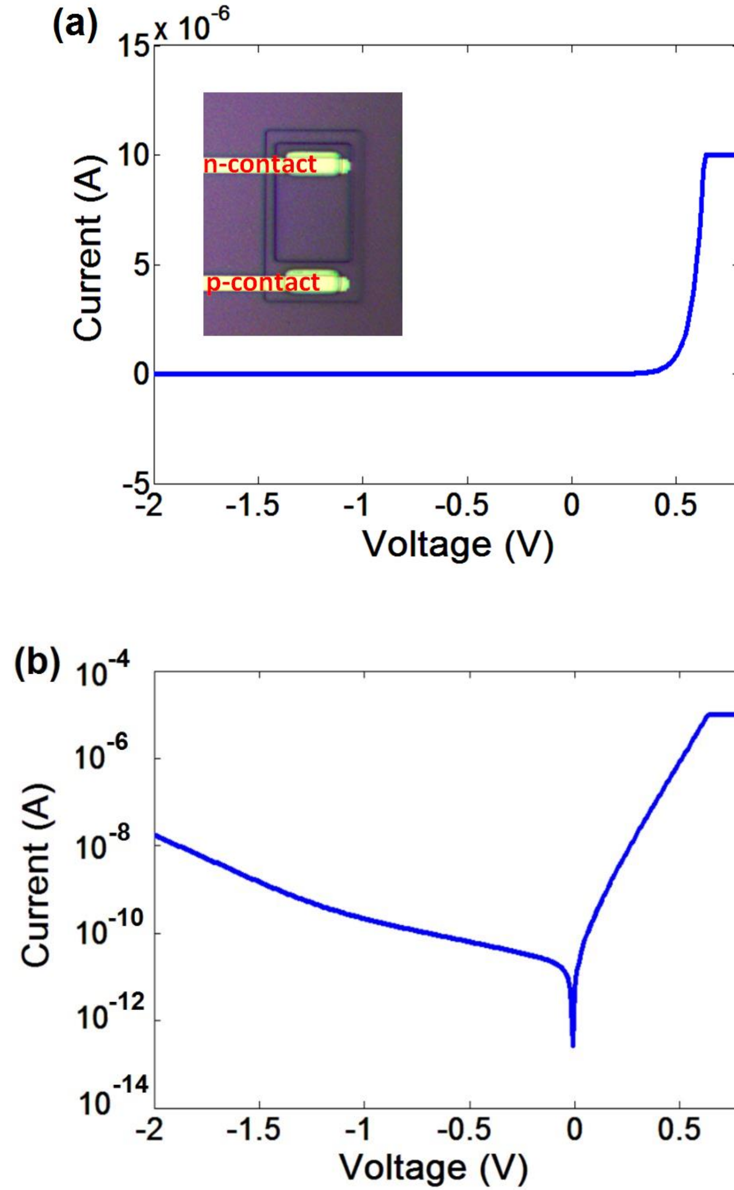

Figure 4.1: (a) Dark current-voltage characteristics of the diffused p-n junction in the absence of light illumination. Inset: Optical microscope image of the fabricated device. (b) Log scale plot of the dark I-V characteristics of the sample junction. The ideality factor is 1.98.

4.3. CEP Device Characterization

4.3.1. Doping Concentration Profiling

Secondary ion mass spectroscopy (SIMS) technique was used to analyze the composition, especially the type of dopants and the doping concentrations of both the OMCVD and the diffused p-n junctions. In our samples, the dopants are boron and phosphorous in silicon.

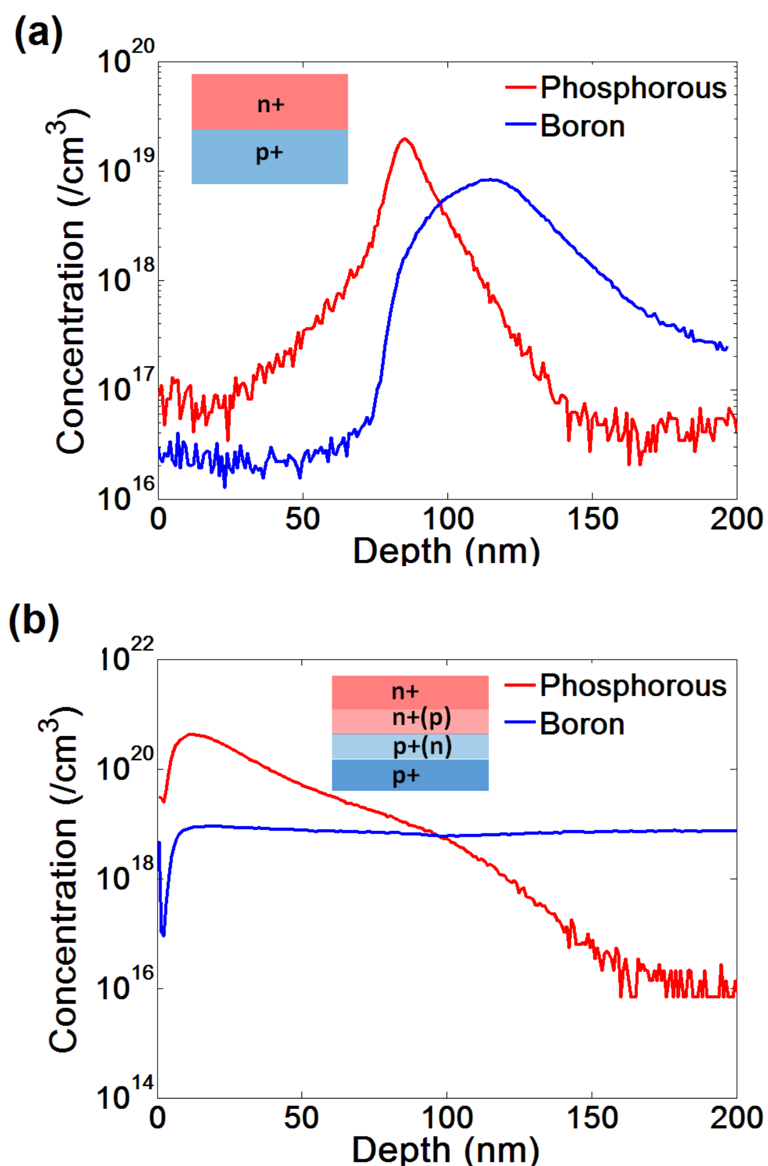

Figure 4.2: (a) SIMS profile of phosphorous and boron in the OMCVD grown silicon p-n junction. (b) SIMS profile of phosphorous and boron in the diffused p-n junction.

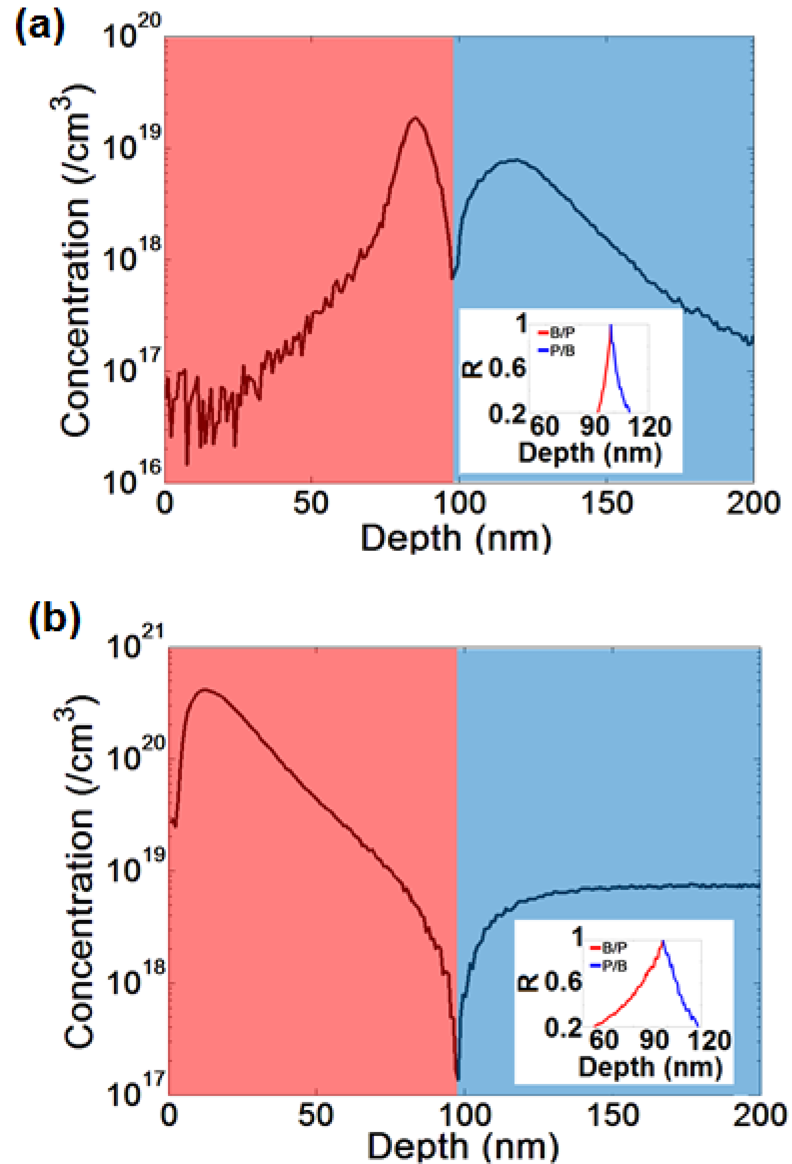

Figure 4.3: (a) Effective doping concentrations of the OMCVD junction. Inset: compensation ratio near the metallurgical junction. (b) Effective doping concentrations of the diffused junction. Inset: compensation ratio near the metallurgical junction.

The major difference between the two structures is the extent of doping compensation as illustrated Figure 4.3. For the OMCVD grown structure, the precise control of the gas flow enables minimum co-existence of both n- and p- type impurities, thus giving rise to a p-n junction with extremely small doping compensation [43]. On

the other hand, the formation of the diffused p-n junction for the diffused sample has to overcompensate the background doping in the substrate to form the n-layer, and the phosphorous diffusion tail also partially compensates the p-region. As a result, the OMCVD sample serves as a model for an uncompensated p-n junction and the diffused sample for a partially compensated p-n junction. The compensation ratio near the junction for both two samples were presented in the insets of Figure 4.3(a) and (b), which confirm that much wider partially compensated regions are present for the diffused sample compared to the epitaxially grown sample.

4.3.2. Bias Dependence Measurement

The photocurrent measurement was done using the setup depicted in Figure 4.3, in order to investigate the temperature dependence of the photoresponse, the device chip was cut into smaller pieces to fit into ceramic dual-in-line packages. The backside of the chip was glued to the package using conductive silver paste (Pelco conductive 187) and baked at 120 ℃ for 30 mins to remove the solvents in the paste. Then the device under test (DUT) was wire bonded using West Bond ball bonder. Gold wires were attached from the on-chip contact pads to the pins of the package. Then a SMA connector was attached to the pins by soldering in a way that both the package and the SMA connector can fit into a cryochamber (Janis VPF-100) for low temperature measurements (Figure 4.5).

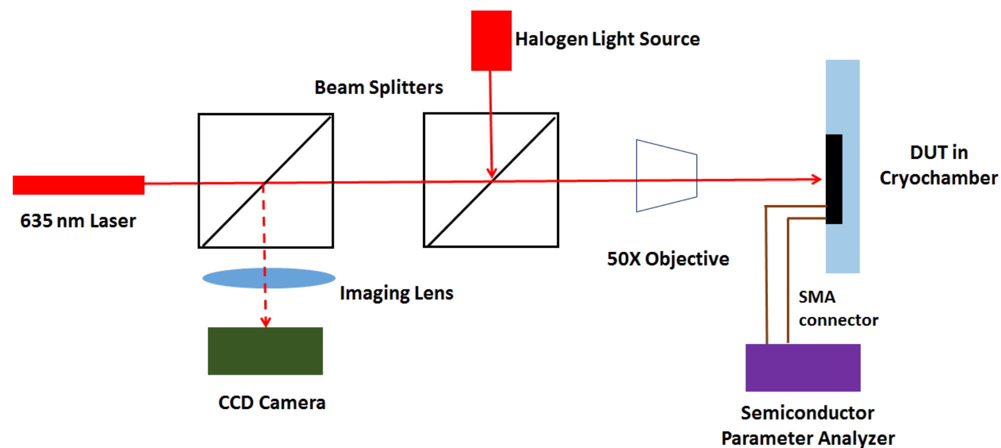

Figure 4.4: Experimental Setup for CEP device measurement.

Since the device was packaged and placed inside of the cryochamber, a simple imaging system was built which was placed on top of a micrometer stage with 3-D linear and rotational control. And a halogen lamp was used for rough alignment to locate the device in the cryochamber, after which using the reflection light from 635 nm laser itself, the image could be captured by the CCD camera directly.

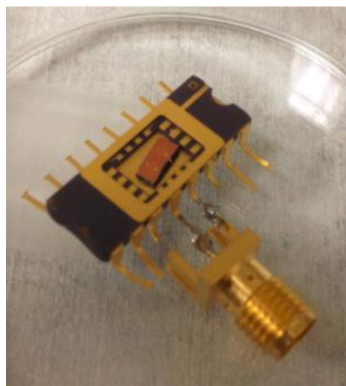

Figure 4.5: Packaged device ready for measurement.

To focus the collimated light to the device mesa, a 50× objective was placed in front of the cryochamber window. A 635 nm laser (Lasermate Group, Inc.) was used

as the light source for the photocurrent measurement. The output was fiber coupled and connected to a mount on the micrometer stage for alignment. The photocurrent of both the epitaxially grown and the diffused devices was measured. The epitaxially grown p-n junction device exhibit the photoresponse of a standard p-n or p-i-n diode, having a nearly constant photocurrent level independent of the bias voltage. In sharp contrast, the diffused p-n junction device shows that the photocurrent increases significantly with the increase of the reverse bias voltage from 0 to -4 V, signifying signal amplification as shown in Figure 4.6.

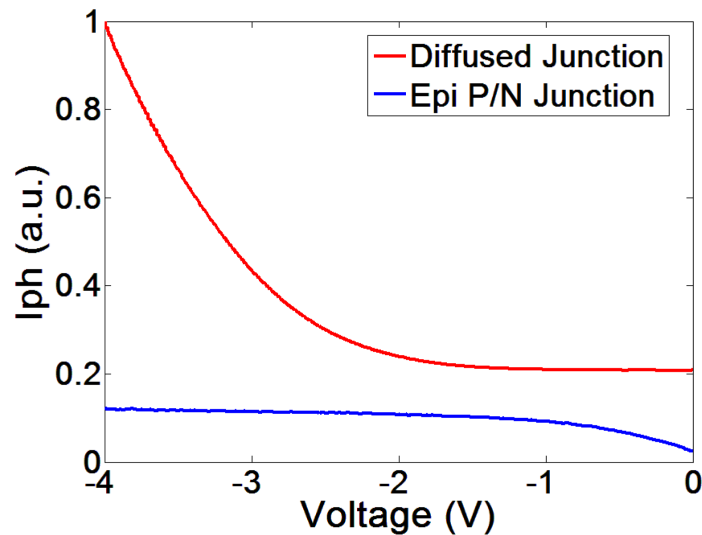

Figure 4.6: Bias dependence of photoresponse to 635 nm laser light for both the diffused and OMCVD epitaxial grown Si p-n junctions at room temperature.

Device simulations have shown that for both device structures avalanche multiplication due to impact ionization does not take place until -20 to -25 V bias, whereas the experimental data from the diffused p-n junction shows that the amplification starts at a bias voltage as low as -2 V. Since the devices have shown typical

I-V characteristics of a normal p-n junction in the dark condition, the observed amplification behavior cannot originate from the photoconductive effect or phototransistor behavior. Moreover, the photoresponse data show that this phenomenon exists only in the heavily compensated p-n junction but is absent in regular p-n junctions. Therefore, the distinctive signal amplification must be explained by an internal carrier multiplication mechanism that is not present in the normal p-n junctions.

4.3.3. Temperature Dependence Measurement

To explore the phenomenon further, the bias dependence of photoresponse under different temperatures was also measured. The commercial cryochamber depicted in Figure 4.4 can be used for cooling control from as low as liquid nitrogen temperature (~ 77 K) to as high as 400 K. A temperature controller Lakeshore 325 was used to monitor and control the temperature within the chamber. It has a two thermal diodes, one was placed near the heater which will be controlled by the heater and the other one was put closer to the actual packaged device to have a more accurate temperature reading. Figure 4.7 shows that the photocurrent of the diffused junction increases monotonically with bias voltage over the entire temperature range of measurements (160 K to 280 K). What is particularly interesting is that the photocurrent is increased with temperature under all bias voltages. Such characteristics can be better shown in Figure 4.8 taking the data at -3 V as an example. For comparison, the temperature dependence of photoresponse of a conventional Si p-i-n diode is also included in the figure.

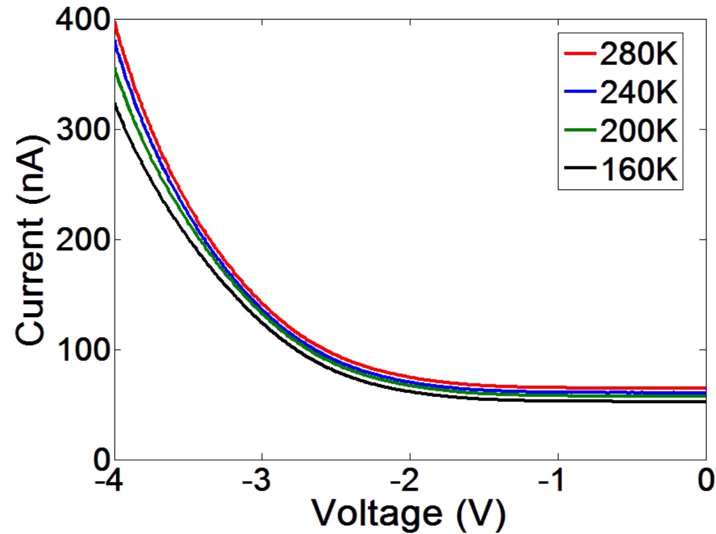

Figure 4.7: Bias dependence of photoresponse to 635 nm laser light at various temperatures for the diffused p-n junction with high doping concentration.

To remove any effects introduced by light coupling and the experimental setup, the normalized photocurrent at different temperatures has been plotted in Figure 4.8 to demonstrate the fundamentally different temperature dependence of photoresponse between the compensated p-n junction and conventional p-n junctions. For conventional Si p-n or p-i-n diodes, the photoresponse between 500 nm and 700 nm is nearly temperature independent, as shown in Figure 4.8. However, we have found that the photoresponse of the heavily compensated p-n junction possessing amplification characteristics has shown an increased photoresponse with increasing temperature. We note that by contrast the photoresponse of an avalanche photodetector decreases with increasing temperature because the increasing phonon scattering hinders the acceleration of carriers under the applied electric field and results in a lower probability for impact ionization [44], [45].

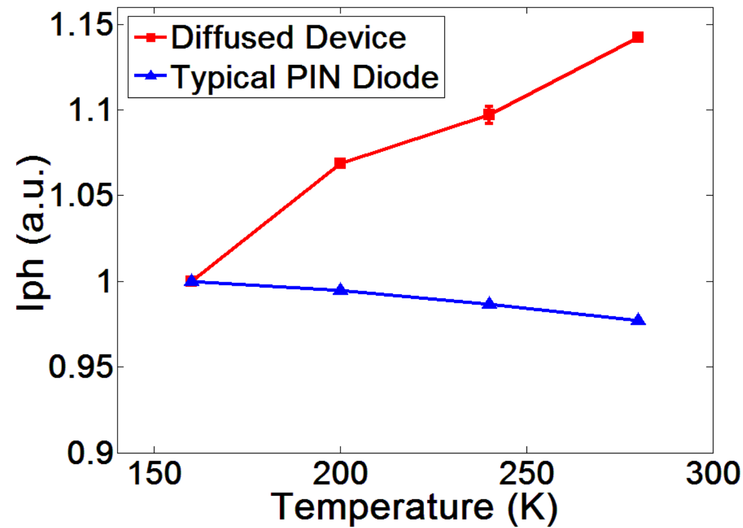

Figure 4.8: Comparison of the temperature dependence of photoresponse between a highly compensated silicon p-n junction and a conventional silicon p-i-n diode at -3 V.

4.4. Results Discussion

Both the bias dependence and temperature dependence l results indicated the existence of a new internal signal amplification mechanism in heavily doped and compensated silicon p-n junctions. It occurred at a much lower voltage than impact ionization and had a gain that increases with temperature to favor room temperature over cryogenic operation. Based on the fact that the gain is only present in materials with significant doping concentration and doping compensation, a cycling excitation process (CEP) consisting of a photoexcited carrier (electron) traversing the p-n junction to gain sufficient kinetic energy to excite an electron-hole pair whose dissociation enables the hole component to repeat the same process by traversing the junction in the opposite direction was proposed and will be discussed in this section.

Figure 4.9 illustrates a pathway for cyclical e-h generations initiated by a photon absorbed in the p-region of the p-n junction, where the primary or the zeroth generation of electron-hole pair (e_p^0 and h_p^0) is created. We label each electron and hole by e and h with superscripts denoting generation and subscripts (p or n) indicating location of the carrier. A symmetric case can also be made for the excitation in the n-region. The primary hole h_p^0 leaves the device via the p-contact and the primary electron e_p^0 moves into the depletion region of the p-n junction gliding over the energy slope and gains kinetic energy. The amount of kinetic energy acquired by the electron is determined by the built-in potential, the applied bias, and the dissipative effect of inelastic scattering by phonons or by carriers in the Fermi sea known as shake-up [46], [47]. For heavily doped p-n junction under low reverse bias, the width of the depletion region (20 to 40 nm) is comparable to the electron mean free path (~ 15 nm) at room temperature [48]. Hence the energetic electron can gain sufficient energy to excite an electron across the energy gap from an ionized acceptor (A^-) in the partially compensated n-doped region. This excitation process, indicated by the vertical arrows in the n-region, generates the first generation of electron hole pair ($e_n^1$and h_n^1). After the excitation, both the zeroth (e_n^0) and first generation (e_n^1) electron leave the device via the n-contact. In the meantime, the acceptor that just lost its electron may capture an electron form the valence band, and this process produces the secondary mobile hole (h_n^1), which can traverse the depletion region and gain sufficient energy for a second excitation process to produce the second generation of electron-hole pair (e_p^2 and h_p^2) in the p-side (depletion region or the p-region) of the junction. The hole goes to the p-contact directly and the electron will again serve as the seed for a new cycle of excitations. Since such scattering and

dissociation events occur with finite probabilities and the carriers suffer energy dissipation by other causes, the cycling process does not exhibit any perpetual motion behavior and renders a net steady state gain.

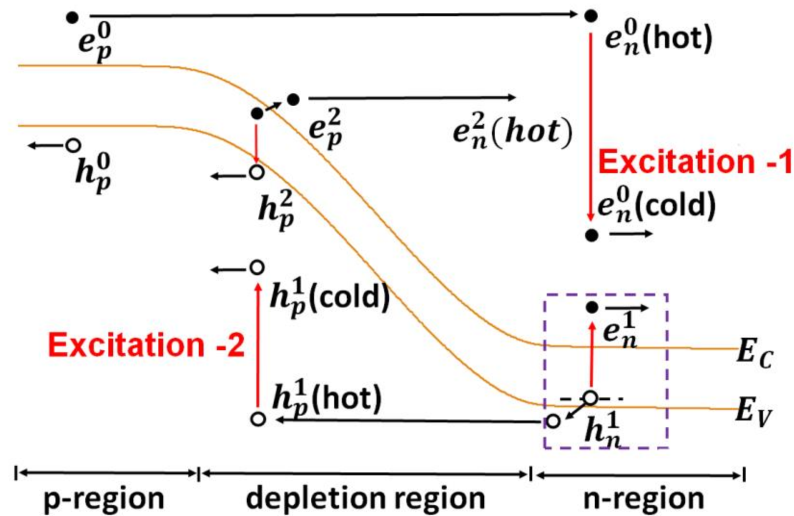

Figure 4.9: Schematic illustration of a cycling excitation process assuming a photon is absorbed in the p-region of the p-n junction and the first two excitation events were depicted in the schematic.

A density of states (DOS) diagram for a point in the n-region of the p-n junction (e.g. a point in the purple square as illustrated in Figure 4.9) is shown in Figure 4.10 [49] – [53]. Given such excitations happen in heavily doped and compensated materials, the transition is believed to be mainly between the donor and acceptor (DA) states which could be either in the extended or local states on either side of the mobility edge of the impurity band [54] – [58]. Thus the transition can produce either a bound DA exciton or a pair of mobile electron and localized hole or vice versa, and the resultant localized electron or hole thermalizes readily to become mobile carrier contributing to the

photocurrent. The interactions between the localized electrons or holes and phonons may also explain why the partially compensated p/n junction device favors room temperature rather than cytogenetic operation. Different from the conventional impact ionization where all carriers are in the conduction and valence bands and can be represented by extended waves, the process concerned here involves the localized wavefunctions which overlap somewhat but determines the interband transitions . This relaxes the k-selection rule and thus allows the process to occur at a much lower voltage than impact ionization.

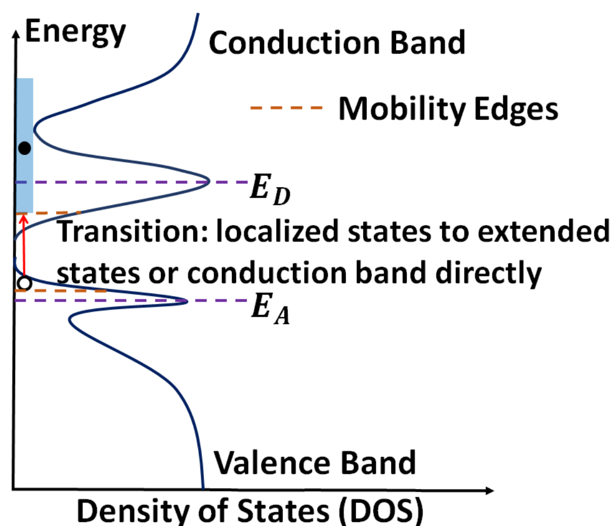

Figure 4.10: Density of states (DOS) distribution with respect to the band diagram in the n-region of the p-n junction. The red arrow indicates the excitation process of bringing an electron across the energy gap from an ionized acceptor (A^-) in the n-region.

In summary, the observed photoresponse amplification mechanisms is due to cycling excitation process (CEP) initiated by optical excitation of electron and hole which produce the back-to-back ionization processes involving at least one localized

state, by virtue of the increase in kinetic energy of a carrier across the p-n junction. This process connects the presence of the heavily doped donor and acceptor compensation, the driving by optical excitation, and the assistance by heat, to produce qualitatively the observed bias and temperature characteristics. Such an effect has as its mainstay the excitation of an electron (hole) from a bound acceptor (donor) state, combined with thermal ionization, to form mobile electron-hole pair. Since the concept in principal can be applied to other semiconductor materials and the initial carrier may be created by photoexcitation or electrical injection in a properly designed structure, the signal amplification effect can potentially be incorporated into various kinds of devices including photodetectors and field effect or bipolar transistors.

This chapter, in part, is a reprint of material as it appears in the following publication: Yuchun Zhou, Yu-hsin Liu, Samia N. Rahman, David Hall, L.J. Sham and Yuhwa Lo, "Discovery of a photoresponse amplification mechanism in compensated PN junctions", Applied Physics Letters, 106, 031103 (2015). The dissertation author was the primary investigator and author of this material.

Chapter 5

CEP Gain Characteristics Modeling

In this chapter, the gain characteristics will be modeled based on the discussions presented in Chapter 4. In particular, a quantum mechanical calculation of the process of electron excitation from ionized acceptors to conduction band will be discussed. Finally, a more general analytical analysis of the cycling excitation process including the gain and its statistic properties will be presented.

5.1 Interband Transition Calculations

As mentioned in Chapter 4, the photoresponse amplification comes from the transition between a localized state to extended states or conduction band directly. In the following, we formulate the quantum mechanical calculation of the excitation process – the excitation of an electron from an ionized acceptor to become a free electron using perturbation theorem [59], [60]. Therefore, the Hamiltonian is defined as:

$$H = H_o + H' = \frac{-\hbar^2}{2m_e}\nabla^2_{\boldsymbol{r_1}} + \frac{-\hbar^2}{2m_e}\nabla^2_{\boldsymbol{r_2}} + V_a + \frac{e^2}{4\pi\epsilon|\boldsymbol{r_1}-\boldsymbol{r_2}|} \quad (5.1)$$

In which, the unperturbed part H_o and the interacting part H' are:

$$H_o = \frac{-\hbar^2}{2m_e}\nabla^2_{\boldsymbol{r_1}} + \frac{-\hbar^2}{2m_e}\nabla^2_{\boldsymbol{r_2}} + V_a \quad (5.2)$$

$$H' = \frac{e^2}{4\pi\epsilon|\boldsymbol{r_1}-\boldsymbol{r_2}|} \tag{5.3}$$

In eqn. (5.2), $\boldsymbol{r_1}$ and $\boldsymbol{r_2}$ are the coordinates of the incoming electron and the electron initially bounded with the acceptor atom before the excitation. V_a is introduced by the potential from the acceptor atom. Here, we have used the effective mass approximation so the unperturbed Hamiltonian does not include the lattice potential term. And in eqn. (5.3), we assumed that the excitation process is through Coulomb interaction only, where $\epsilon = 11.68\,\varepsilon_0$ is the dielectric constant of silicon. The normalized initial state wavefunction before the transition can be represented by:

$$\Psi_{initial}(\boldsymbol{r_1}, \boldsymbol{r_2}, t) = \left[\varphi_{k_1} e^{-i\omega_1 t}\right]\left[\varphi_{1S} e^{-i\omega_2 t}\right] = \left[\frac{e^{i\boldsymbol{k_1 r_1}}}{\sqrt{V}} e^{-i\omega_1 t}\right]\left[\frac{e^{-r_2/a_S}}{\sqrt{\pi a_S^3}} e^{-i\left|\frac{\epsilon_i}{\hbar}\right| t} e^{+i\frac{E_g}{\hbar} t}\right] \tag{5.4}$$

Again, subscript 1 or 2 was used to denote either the incident (hot) electron or the bounded electron. Therefore, $\boldsymbol{k_1}$ is the wave vector of the incident electron. Note that here we further assumed that the external field makes negligible changes of the electron momentum over the range of electron-acceptor interaction. So, we could assume that k_1 to be a constant within the interaction range. ω_1 is the angular frequency associated with the incident electron and $\omega_1 = \frac{\hbar^2 {k_1}^2}{2m_e}$. For the electron bounded with the acceptor, we assume the wavefunction of the impurity state is given by the 1s hydrogenic form: $\frac{e^{-r_2/a_S}}{\sqrt{\pi a_S^3}}$, where $a_S = \frac{4\pi\hbar^2}{m_e e^2}$, is the Bohr radius using effective mass approximation. Define the energy required for removing the bound electron from the acceptor to the conduction band:

$$E_i = E_g - |\epsilon_i| \tag{5.5}$$

where $|\epsilon_i|$=0.045 eV is the ionization energy for acceptors (boron in this case) and E_g is the bandgap energy of silicon. If we choose the conduction band edge as the energy reference, thus the time dependent part can be written in the form of $e^{-i\left|\frac{\epsilon_i}{\hbar}\right|t} e^{+i\frac{E_g}{\hbar}t}$ as shown in eqn. (5.4). After the collision, the normalized final state wavefunction can be written as:

$$\Psi_{final}(\boldsymbol{r_1}, \boldsymbol{r_2}, t) = \sum_{i,j} a_{ij}(t)|i,j> e^{-i\omega_i t} e^{-i\omega_j t} = \sum_{i,j} \frac{e^{ik_i r_1}}{\sqrt{V}} \frac{e^{ik_j r_2}}{\sqrt{V}} e^{-i\omega_i t} e^{-i\omega_j t} \tag{5.6}$$

Again, subscripts i and j denote the incident electron after the collision and the electron used to be bounded with the acceptor. And after the excitation event both two electrons possess the electron wavefunctions as extended (traveling) waves with the time dependent terms written as $e^{-i\omega_i t}$ and $e^{-i\omega_j t}$. Therefore the transition rate from the initial state $\Psi_{initial}(\boldsymbol{r_1}, \boldsymbol{r_2}, t)$ to the final state $\Psi_{final}(\boldsymbol{r_1}, \boldsymbol{r_2}, t)$ using the perturbation theorem:

$$W(i,j) = \frac{d}{dt}\left|a_{ij}(t)\right|^2 = \frac{2\pi}{\hbar^2}\left|< k_i, k_j|H'|k_1, 1s >\right|^2 \delta(\omega_i + \omega_j - \omega_1 + \frac{E_i}{\hbar}) \tag{5.7}$$

First, let's calculate the matrix element:

$$\left|< k_i, k_j|H'|k_1, 1s >\right| = \left| \iint_{r_1 r_2} \left[\frac{e^{-ik_i r_1}}{\sqrt{V}} \frac{e^{-ik_j r_2}}{\sqrt{V}}\right] \left[\frac{e^2}{4\pi\epsilon|\boldsymbol{r_1}-\boldsymbol{r_2}|}\right] \left[\frac{e^{ik_1 r_1}}{\sqrt{V}} \frac{e^{-r_2/a_s}}{\sqrt{\pi a_s^3}}\right] d^3r_1 d^3r_2 \right| \tag{5.8}$$

The 1-s hydrogenic state term e^{-r_2/a_s} can be expressed using Fourier integral:

$$e^{-r_2/a_s} = \left(\frac{1}{2\pi}\right)^3 \int_{k_2} A(\boldsymbol{k_2}) e^{i\boldsymbol{k_2}\boldsymbol{r_2}} d^3k_2 \tag{5.9}$$

Assuming here the angle between $\boldsymbol{k_2}$ and $\boldsymbol{r_2}$ is θ, $A(\boldsymbol{k_2})$ can be written as:

$$A(\boldsymbol{k_2}) = \int_{r_2} e^{-r_2/a_s} e^{-i\boldsymbol{k_2 r_2}} d^3r = 2\pi \int_{\theta=0}^{\pi} \int_{r_2=0}^{\infty} e^{-r/a_s} e^{-i[k_2 cos\theta]r_2} r_2^2 dr_2 \, sin\theta d\theta =$$

$$4\pi(a_s)^3 \int_{\theta=0}^{\pi} \frac{sin\theta \, d\theta}{(1+ik_2 a_s cos\theta)^3} = \frac{8\pi(a_s)^3}{(1+a_s^2 k_2^2)^2} \quad (5.10)$$

Note that $A(\boldsymbol{k_2})$ depends only on the length of $\boldsymbol{k_2}$ (k_2), not the direction of $\boldsymbol{k_2}$.Therefore, eqn. (5.9) can be expressed as:

$$e^{-r_2/a_s} = \left(\frac{1}{2\pi}\right)^3 \int_{k_2} \frac{8\pi(a_s)^3}{(1+a_s^2 k_2^2)^2} e^{i\boldsymbol{k_2 r_2}} d^3k_2 \quad (5.11)$$

Substitute eqn. (5.11) into eqn. (5.8):

$$\left| < k_i, k_j | H' | k_1, 1s > \right| =$$

$$\left| \frac{\sqrt{V}}{\sqrt{\pi a_s^3}} \left(\frac{1}{2\pi}\right)^3 \int_{k_2} \frac{8\pi(a_s)^3}{(1+a_s^2 k_2^2)^2} d^3k_2 \iint_{r_1 r_2} \left[\frac{e^{-i\boldsymbol{k_i r_1}}}{\sqrt{V}} \frac{e^{-i\boldsymbol{k_j r_2}}}{\sqrt{V}}\right] \left[\frac{e^2}{4\pi\epsilon|\boldsymbol{r_1}-\boldsymbol{r_2}|}\right] \left[\frac{e^{i\boldsymbol{k_1 r_1}}}{\sqrt{V}} \frac{e^{i\boldsymbol{k_2 r_2}}}{\sqrt{V}}\right] d^3r_1 d^3r_2 \right| \quad (5.12)$$

Let $\boldsymbol{k_1} - \boldsymbol{k_i} = \Delta_1$ and $\boldsymbol{k_2} - \boldsymbol{k_j} = \Delta_2$, we have:

$$\left| < k_i, k_j | H' | k_1, 1s > \right| =$$

$$\left| \frac{8\pi(a_s)^3\sqrt{V}}{V^2\sqrt{\pi a_s^3}} \left(\frac{1}{2\pi}\right)^3 \int_{k_2} \frac{1}{(1+a_s^2 k_2^2)^2} d^3k_2 \iint_{r_1 r_2} d^3r_1 d^3r_2 \left[\frac{e^2}{4\pi\epsilon|\boldsymbol{r_1}-\boldsymbol{r_2}|}\right] e^{i\Delta_1 \boldsymbol{r_1}} e^{i\Delta_2 \boldsymbol{r_2}} \right| \quad (5.13)$$

Define $f(\boldsymbol{r}) = \frac{1}{|r|}$ and $g(\boldsymbol{r}) = e^{i\Delta_1 \boldsymbol{r}}$, the term $\iint_{r_1 r_2} d^3r_1 d^3r_2 \left[\frac{e^2}{4\pi\epsilon|\boldsymbol{r_1}-\boldsymbol{r_2}|}\right] e^{i\Delta_1 \boldsymbol{r_1}} e^{i\Delta_2 \boldsymbol{r_2}}$ can be written as:

$$\iint_{r_1 r_2} d^3r_1 d^3r_2 \left[\frac{e^2}{4\pi\epsilon|\boldsymbol{r_1}-\boldsymbol{r_2}|}\right] e^{i\Delta_1 \boldsymbol{r_1}} e^{i\Delta_2 \boldsymbol{r_2}} = \frac{e^2}{4\pi\epsilon} \int_{r_2} e^{i\Delta_2 \boldsymbol{r_2}} d^3r_2 \left[\int_{r_1} f(\boldsymbol{r_1} - \boldsymbol{r_2}) g(\boldsymbol{r_1}) \, d^3r_1\right]$$

$$= \frac{e^2}{4\pi\epsilon} \int_{r_2} e^{i\Delta_2 \boldsymbol{r_2}} [f * g] d^3 r_2 \tag{5.14}$$

Let $H(r_2) = \int_{r_1} f(\boldsymbol{r_1} - \boldsymbol{r_2}) g(\boldsymbol{r_1})\, d^3 r_1 = f * g$, we have:

$$\iint_{r_1 r_2} d^3 r_1 d^3 r_2 \left[\frac{e^2}{4\pi\epsilon |\boldsymbol{r_1} - \boldsymbol{r_2}|}\right] e^{i\Delta_1 \boldsymbol{r_1}} e^{i\Delta_2 \boldsymbol{r_2}} = \frac{e^2}{4\pi\epsilon} \int_{r_2} e^{i\Delta_2 \boldsymbol{r_2}} [f * g] d^3 r_2$$

$$= \frac{e^2}{4\pi\epsilon} \int_{r_2} e^{i\Delta_2 \boldsymbol{r_2}} H(r_2) d^3 r_2 = \frac{e^2}{4\pi\epsilon} F(H) = \frac{e^2}{4\pi\epsilon} F(f) F(g) \tag{5.15}$$

$F(H)$, $F(f)$ and $F(g)$ are the Fourier transforms of the functions $H, f,$ and g, then:

$$F(f) = \int_{r_2} \frac{e^{i\Delta_2 \boldsymbol{r_2}}}{|r_2|} d^3 r_2 = \int_{r} \frac{e^{i\Delta_2 \boldsymbol{r}}}{|r|} d^3 r \tag{5.16}$$

$$F(g) = \int_{r_2} e^{i\Delta_1 \boldsymbol{r_1}} e^{i\Delta_2 \boldsymbol{r_2}}\ d^3 r_2 = (2\pi)^3 \delta(\Delta_1 + \Delta_2) \tag{5.17}$$

Therefore, eqn. (5.14) becomes:

$$\iint_{r_1 r_2} d^3 r_1 d^3 r_2 \left[\frac{e^2}{4\pi\epsilon |\boldsymbol{r_1} - \boldsymbol{r_2}|}\right] e^{i\Delta_1 \boldsymbol{r_1}} e^{i\Delta_2 \boldsymbol{r_2}} = \frac{e^2}{4\pi\epsilon} (2\pi)^3 \delta(\Delta_1 + \Delta_2) \int_{r} \frac{e^{i\Delta_2 \boldsymbol{r}}}{|r|} d^3 r \tag{5.18}$$

Substitute eqn. (5.18) into eqn. (5.13), we have:

$$|< k_i, k_j | H' | k_1, 1s >| = \left| \frac{8\pi (a_s)^3 \sqrt{V}}{V^2 \sqrt{\pi a_s^3}} \frac{e^2}{4\pi\epsilon} \int_{k_2} \frac{1}{(1 + a_s^2 k_2^2)^2} d^3 k_2\, \delta(\Delta_1 + \Delta_2) \int_{r} \frac{e^{i\Delta_2 \boldsymbol{r}}}{|r|} d^3 r \right| \tag{5.19}$$

Note that the δ function here $(\Delta_1 + \Delta_2) = \delta(\boldsymbol{k_1} + \boldsymbol{k_2} - \boldsymbol{k_i} - \boldsymbol{k_j})$ demonstrates that the phase matching condition or momentum conservation condition was inherently satisfied for all the random value of $\boldsymbol{k_2}$s from Fourier transform of the impurity state wavefunction. Using the phase matching condition, eqn. (5.19) becomes:

$$\left|< k_i, k_j|H'|k_1, 1s >\right| = \left|\frac{8\pi(a_s)^3\sqrt{V}}{V^2\sqrt{\pi a_s^3}}\frac{e^2}{4\pi\epsilon}\frac{1}{(1+a_s^2|\boldsymbol{k_i}+\boldsymbol{k_j}-\boldsymbol{k_1}|^2)^2}\int_r \frac{e^{i(\boldsymbol{k_i}-\boldsymbol{k_1})r}}{|r|}d^3r\right| \quad (5.20)$$

To calculate the term $\int_r \frac{e^{i(\boldsymbol{k_i}-\boldsymbol{k_1})r}}{|r|}d^3r$ in eqn. (5.20), we assume the angle between $(\boldsymbol{k_i} - \boldsymbol{k_1}$ and $\boldsymbol{r}$ is θ again we have:

$$\int_r \frac{e^{i(\boldsymbol{k_i}-\boldsymbol{k_1})r}}{|r|}d^3r = 2\pi\int_{\theta=0}^{\pi}\int_{r=0}^{\infty}\frac{e^{i|\boldsymbol{k_i}-\boldsymbol{k_1}|rcos(\theta)}}{r}sin\theta\, d\theta r^2 dr = \frac{4\pi}{|\boldsymbol{k_i}-\boldsymbol{k_1}|^2} \quad (5.21)$$

Substitute eqn. (5.21) into eqn. (5.20):

$$\left|< k_i, k_j|H'|k_1, 1s >\right| = \left|\frac{8\pi(a_s)^3\sqrt{V}}{V^2\sqrt{\pi a_s^3}}\frac{e^2}{4\pi\epsilon}\frac{1}{(1+a_s^2|\boldsymbol{k_i}+\boldsymbol{k_j}-\boldsymbol{k_1}|^2)^2}\frac{4\pi}{|\boldsymbol{k_i}-\boldsymbol{k_1}|^2}\right| \quad (5.22)$$

Therefore, eqn. (5.7) can be written as:

$$W(i,j) = \frac{2\pi}{\hbar^2}\left|\frac{8\pi e^2(a_s)^3\sqrt{V}}{\epsilon V^2\sqrt{\pi a_s^3}}\frac{1}{(1+a_s^2|\boldsymbol{k_i}+\boldsymbol{k_j}-\boldsymbol{k_1}|^2)^2}\frac{1}{|\boldsymbol{k_i}-\boldsymbol{k_1}|^2}\right|^2 \delta(\omega_i + \omega_j - \omega_1 + \frac{E_i}{\hbar}) \quad (5.23)$$

Eqn. (5.23) represents the transition rate between one specific initial state and the corresponding final state /*i, j*>. Now, let's summarize all the available k states using the constraint on ks based on the energy conservation:

$$k_i^2 + k_j^2 = -\frac{2m_e E_i}{\hbar^2} + k_1^2 \quad (5.24)$$

Therefore the total transition rate is:

$$W_{TOT} = \sum_{Allowed\ k_i,k_j} W(i,j) = \frac{2\pi}{\hbar^2}\left|\frac{8\pi e^2(a_s)^3\sqrt{V}}{\epsilon V^2\sqrt{\pi a_s^3}}\right|^2 \int_{k_i}\int_{k_j}\frac{1}{(1+a_s^2\left|\boldsymbol{k_i}+\boldsymbol{k_j}-\boldsymbol{k_1}\right|^2)^4}\frac{1}{|\boldsymbol{k_i}-\boldsymbol{k_1}|^4}\delta(\omega_i +$$

$$\omega_j - \omega_1 + \frac{E_i}{\hbar})\frac{V}{(2\pi)^3}\frac{V}{(2\pi)^3}d^3k_j\, d^3k_i \quad (5.25)$$

Representing δ function using k vector instead of angular frequency ω, eqn. (5.25) can be written as:

$$W_{TOT} = \frac{2\pi}{\hbar^2}\frac{2m_e}{\hbar}\left|\frac{8\pi e^2(a_s)^3\sqrt{V}}{\epsilon V^2\sqrt{\pi a_s^3}}\right|^2 \int_{k_i}\int_{k_j} \frac{1}{\left(1+a_s^2|\boldsymbol{k_i}+\boldsymbol{k_j}-\boldsymbol{k_1}|^2\right)^4}\frac{1}{|\boldsymbol{k_i}-\boldsymbol{k_1}|^4}\delta([k_1^2-\frac{2m_eE_i}{\hbar^2}]-[k_i^2+k_j^2])\frac{V}{(2\pi)^3}\frac{V}{(2\pi)^3}d^3k_j\, d^3k_i \quad (5.26)$$

Let $C = \frac{2\pi}{\hbar^2}\frac{2m_e}{\hbar}\left|\frac{8\pi e^2(a_s)^3\sqrt{V}}{\epsilon V^2\sqrt{\pi a_s^3}}\right|^2$ and define the angle between $\boldsymbol{k_1}-\boldsymbol{k_i}$ and $\boldsymbol{k_j}$ is θ_j, we have:

$$W_{TOT} = C\int_{k_i}\frac{d^3k_i}{|\boldsymbol{k_i}-\boldsymbol{k_1}|^4}2\pi\int_{\theta_j=0}^{\pi}d\theta_j\int_{k_j=0}^{\infty}\frac{(sin\theta_j)k_j^2dk_j}{\left\{1+a_s^2\left[\left(k_jsin\theta_j\right)^2+(|\boldsymbol{k_i}-\boldsymbol{k_1}|-k_jcos\theta_j)^2\right]\right\}^4}\delta([k_1^2-\frac{2m_eE_i}{\hbar^2}]-[k_i^2+k_j^2])\frac{V}{(2\pi)^3}\frac{V}{(2\pi)^3} \quad (5.27)$$

Now let $P_j = k_j^2$,

$$W_{TOT} = C\int_{k_i}\frac{d^3k_i}{|\boldsymbol{k_i}-\boldsymbol{k_1}|^4}2\pi\int_{\theta_j=0}^{\pi}d\theta_j\int_{P_j=0}^{\infty}\frac{(sin\theta_j)\sqrt{P_j}d\,P_j}{2\{1+a_s^2[\,P_j+|\boldsymbol{k_i}-\boldsymbol{k_1}|^2-2\sqrt{P_j}|\boldsymbol{k_i}-\boldsymbol{k_1}|cos\theta_j]\}^4}\delta(\,P_j+k_i^2-k_1^2+\frac{2m_eE_i}{\hbar^2})\frac{V}{(2\pi)^3}\frac{V}{(2\pi)^3} \quad (5.28)$$

Using $\delta(\,P_j+k_i^2-k_1^2+\frac{2m_eE_i}{\hbar^2})$ and if $P_j = \left[k_1^2-\frac{2m_eE_i}{\hbar^2}\right]-k_i^2 = U-k_i^2$, we have:

$$W_{TOT} = C\int_{k_i}\frac{d^3k_i}{|\boldsymbol{k_i}-\boldsymbol{k_1}|^4}2\pi\int_{\theta_j=0}^{\pi}\frac{(sin\theta_j)\sqrt{U-k_i^2}d\theta_j}{2\left\{1+a_s^2\left[(U-k_i^2)+|\boldsymbol{k_i}-\boldsymbol{k_1}|^2-2\sqrt{U-k_i^2}|\boldsymbol{k_i}-\boldsymbol{k_1}|cos\theta_j\right]\right\}^4}\frac{V}{(2\pi)^3}\frac{V}{(2\pi)^3} \quad (5.29)$$

After the integration over θ_j and let $k_{j0} = \sqrt{U-k_i^2} = \sqrt{k_1^2-\frac{2m_eE_i}{\hbar^2}-k_i^2}$:

$$W_{TOT} = C'\int_{k_i}\frac{d^3k_i}{|\boldsymbol{k_i}-\boldsymbol{k_1}|^4}\left[\frac{1}{|\boldsymbol{k_i}-\boldsymbol{k_1}|}\right]\left\{\left[\frac{1}{1+a_s^2(|\boldsymbol{k_i}-\boldsymbol{k_1}|-k_{j0})^2}\right]^3-\left[\frac{1}{1+a_s^2(|\boldsymbol{k_i}-\boldsymbol{k_1}|+k_{j0})^2}\right]^3\right\} \quad (5.30)$$

In eqn. (5.30),

$$C' = C\frac{V}{(2\pi)^3}\frac{V}{(2\pi)^3}\frac{2\pi}{12a_s^2} = \frac{1}{V}\frac{(m_e a_s)}{\hbar^3}\left|\frac{e^2}{4\pi\epsilon}\right|^2\frac{32}{3\pi} \tag{5.31}$$

Now, the total transition rate becomes a single integral over k_i. Assuming the angle between the scattered electron wave vector $\boldsymbol{k_i}$ and the original incident electron wave vector $\boldsymbol{k_1}$ is θ_i, eqn. (5.30) becomes:

$$W_{TOT} = C'\int_{k_i}\frac{d^3k_i}{|\boldsymbol{k_i}-\boldsymbol{k_1}|^4}\left[\frac{1}{|\boldsymbol{k_i}-\boldsymbol{k_1}|}\right]\left\{\left[\frac{1}{1+a_s^2(|\boldsymbol{k_i}-\boldsymbol{k_1}|-k_{j0})^2}\right]^3-\left[\frac{1}{1+a_s^2(|\boldsymbol{k_i}-\boldsymbol{k_1}|+k_{j0})^2}\right]^3\right\}$$

$$= C'\int_{\theta_i=0}^{\pi}2\pi sin\theta_i d\theta_i\int_{k_i=0}^{\sqrt{\left[k_1^2-\frac{2m_eE_i}{\hbar^2}\right]}}\frac{k_i^2dk_i}{|\boldsymbol{k_i}-\boldsymbol{k_1}|^4}\left[\frac{1}{|\boldsymbol{k_i}-\boldsymbol{k_1}|}\right]\left\{\left[\frac{1}{1+a_s^2(|\boldsymbol{k_i}-\boldsymbol{k_1}|-k_{j0})^2}\right]^3-\right.$$

$$\left.\left[\frac{1}{1+a_s^2(|\boldsymbol{k_i}-\boldsymbol{k_1}|+k_{j0})^2}\right]^3\right\} \tag{5.32}$$

And for $|\boldsymbol{k_i}-\boldsymbol{k_1}|$ we have:

$$|\boldsymbol{k_i}-\boldsymbol{k_1}| = \sqrt{k_i^2+k_1^2-2k_1k_icos\theta_i} \tag{5.33}$$

The expressions for C' is a variable as a function of the active device volume V in eqn. (5.31) and we have:

$$k_{j0} = \sqrt{k_1^2-\frac{2m_eE_i}{\hbar^2}-k_i^2} \tag{5.34}$$

Using eqn. (5.31) to eqn. (5.34), for a given incident electron with wave vector $\boldsymbol{k_1}$, the net total transition rate can be expressed as:

$$W_{TOT} = C' \int_{\theta_i=0}^{\pi} 2\pi sin\theta_i d\theta_i \int_{k_i=0}^{\sqrt{\left[k_1^2 - \frac{2m_e E_i}{\hbar^2}\right]}} \frac{k_i^2 dk_i}{|\boldsymbol{k_i} - \boldsymbol{k_1}|^5} \left\{ \left[\frac{1}{1 + a_s^2 (|\boldsymbol{k_i} - \boldsymbol{k_1}| - k_{j0})^2} \right]^3 - \left[\frac{1}{1 + a_s^2 (|\boldsymbol{k_i} - \boldsymbol{k_1}| + k_{j0})^2} \right]^3 \right\} \quad (5.35)$$

Note that the upper limit for k_i integral is $k_i = \sqrt{\left[k_1^2 - \frac{2m_e E_i}{\hbar^2}\right]}$. This is determined by energy requirement for the transition to happen. Furthermore, the net rate of secondary electron excitation with an acceptor concentration profile $N_a(z)$, assuming z is the incident electron traveling direction:

$$R = A \int_{z=0}^{L} W_{TOT}\, N_a(z) dz =$$

$$\frac{(m_e a_s)}{\hbar^3} \left| \frac{e^2}{4\pi\epsilon} \right|^2 \frac{32}{3\pi} \int_{z=0}^{L} \frac{N_a(z)}{L_{int}} dz \int_{\theta_i=0}^{\pi} 2\pi sin\theta_i d\theta_i \int_{k_i=0}^{\sqrt{\left[k_1^2 - \frac{2m_e E_i}{\hbar^2}\right]}} \frac{k_i^2 dk_i}{|\boldsymbol{k_i} - \boldsymbol{k_1}|^5} \left\{ \left[\frac{1}{1 + a_s^2 (|\boldsymbol{k_i} - \boldsymbol{k_1}| - k_{j0})^2} \right]^3 - \left[\frac{1}{1 + a_s^2 (|\boldsymbol{k_i} - \boldsymbol{k_1}| + k_{j0})^2} \right]^3 \right\} \quad (5.36)$$

Here, A is defined as the cross section associated with the incident electron wave, and L_{int} is the interaction length of the excitation event. Therefore, the interaction volume can be defined as $V = AL_{int}$. Therefore, as the electron traveling through the whole active interaction region $0 \le z \le L$, the average number of secondary electrons that can be produced from the collisions with the ionized acceptors is:

$$X = A \int_{z=0}^{L} \frac{L_{int}}{v(z)} W_{TOT}\, N_a(z) dz =$$

$$\frac{(m_e a_s)}{\hbar^3} \left| \frac{e^2}{4\pi\epsilon} \right|^2 \frac{32}{3\pi} \int_{z=0}^{L} \frac{N_a(z)}{v(z)} dz \int_{\theta_i=0}^{\pi} 2\pi sin\theta_i d\theta_i \int_{k_i=0}^{\sqrt{\left[k_1^2 - \frac{2m_e E_i}{\hbar^2}\right]}} \frac{k_i^2 dk_i}{|\boldsymbol{k_i} - \boldsymbol{k_1}|^5} \left\{ \left[\frac{1}{1 + a_s^2 (|\boldsymbol{k_i} - \boldsymbol{k_1}| - k_{j0})^2} \right]^3 - \left[\frac{1}{1 + a_s^2 (|\boldsymbol{k_i} - \boldsymbol{k_1}| + k_{j0})^2} \right]^3 \right\} \quad (5.37)$$

Here, $v(z)$ is the velocity of the incident electron at one specific location z when the collision happens. It has to be mentioned that W_{TOT} in eqn. (5.36) and (5.37) is also usually z dependent – $W_{TOT}(z)$, since the value of W_{TOT} is a function of the magnitude of the incident wave vector k_1 which may gain its value while the electron traveling through a high electric field region (e.g. the depletion region of a p-n junction) [61]. Figure 5.1 shows the average number of electron-hole pairs generated by a high energetic carrier as a function of bias voltage from MATLAB calculations based on eqn. (5.37) considering that the back-to-back cycling excitation process happens only within the depletion region of the diffused p-n junction discussed in Chapter 4.

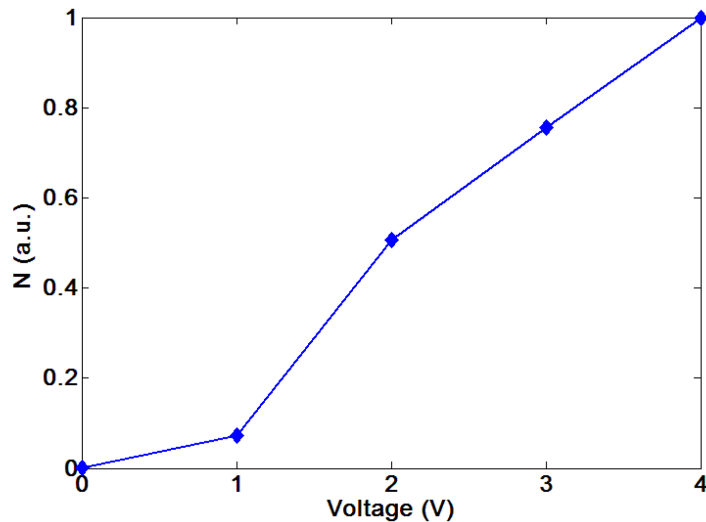

Figure 5.1: Average number of electron-hole pairs (N) generated by an energetic carrier as a function of the bias voltage from numerical simulations.

Therefore, using eqn. (5.37) the average number of secondary electrons that can be produced for one incoming hot electron can be calculated numerically for a specific device structure. The parameters including k_i and $v(z)$ can be obtained using

commercial software Silvaco Atlas based on the corresponding device structure and the bias conditions.

5.2 Analytical and Simulation Results

5.2.1 Analytical Analysis of the CEP Process

We further performed an analytical analysis of the CEP process as described in Chapter 4, and the expression of the photoresponse gain (amplification factor) was obtained as a function of the average number of secondary electron-hole pairs by one incoming hot electron or hole.

Figure 5.2 shows how the photogenerated primary (zeroth generation) electron-hole pair initiates the cycling excitation process. In the figure, we label each electron and hole according to its generation. For example, we use "0" to denote the primary electron and hole generated by photon absorption. The number of electron-hole pairs produced by the $i-$th generation hot electron and hot hole is assumed to be X_i and Y_i, respectively. X_i and Y_i are considered to be independent random variables and all X_i's and Y_i's have their mean values:

$$\langle X_i \rangle = x \; (i = 0,1,2,\dots) \tag{5.38}$$

$$\langle Y_i \rangle = y \; (i = 0,1,2,\dots) \tag{5.39}$$

The average number of electron-hole pairs produced by the absorption of a single photon in the p-side over the series of cyclic excitations is given by:

$$G_{p-side} = \langle 1 + X_o + X_oY_1 + X_oY_1X_2 + X_oY_1X_2Y_3 + X_oY_1X_2Y_3X_4 + \cdots \rangle \tag{5.40}$$

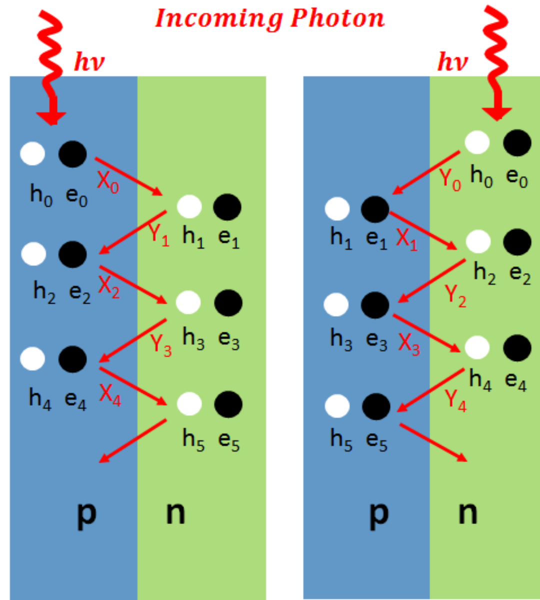

Figure 5.2: Carrier multiplication by cycling excitation process initiated from a single photon incident on either the p-side or n-side of the heavily doped and compensated junction.

Using the relations in eqn. (5.38) and eqn. (5.39), we can simplify eqn. (5.40) into the following:

$$G_{p-side} = \frac{1+x}{1-xy} \tag{5.41}$$

Such cyclic excitations described in eqn. (5.40) or eqn. (5.41) can also be better illustrated in a block diagram in Figure 5.3.

Similarly, the average number of electron-hole pairs due to absorption of a single photon in the n-side is derived as:

$$G_{n-side} = \langle 1 + Y_o + Y_oX_1 + Y_oX_1Y_2 + Y_oX_1Y_2X_3 + Y_oX_1Y_2X_3Y_4 + \cdots \rangle \tag{5.42}$$

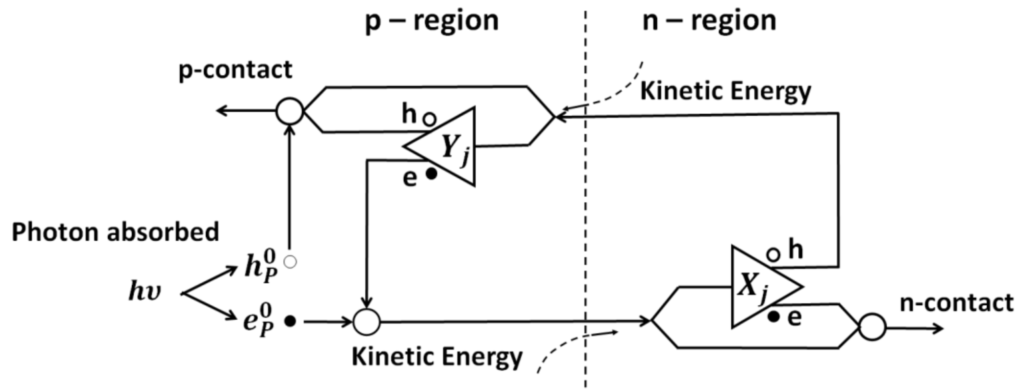

Figure 5.3: Block diagram illustration of the cycling excitation process (CEP), taking the process initiated by a photon absorbed in the p-region of the p-n junction as an example, in which the j – th hot electron or hole can produce X_j or Y_j e-h pairs in each excitation event.

Again, using eqn. (5.38) and eqn. (5.39), we can simplify eqn. (5.42) into the following:

$$G_{n-side} = \frac{1+y}{1-xy} \tag{5.43}$$

Finally, the total number of electron-hole pairs of a p-n junction device can be derived as:

$$G_{junction} = \frac{P_p(1+x)+P_n(1+y)}{(P_p+P_n)(1-xy)} \tag{5.44}$$

where P_p and P_n in eqn. (5.44) stand for the probabilities for the incoming photon to be absorbed in the p – side and n – side of the device. Using eqn. (5.44), under the assumptions that $P_p = P_n$ (equal opportunity for light to be absorbed in p – and n – side of the p – n junction) and $x = y$, the gain as function of the x/y can be plotted in the following figure:

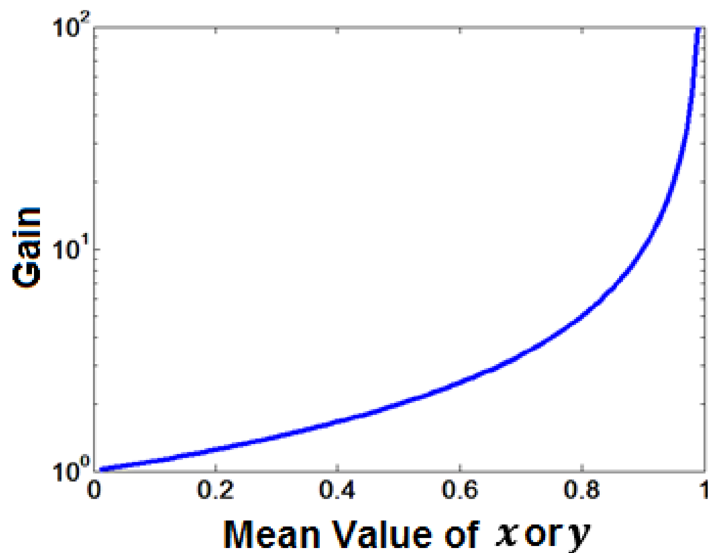

Figure 5.4: The photoresponse gain as a function of the mean value of x/y, and x/y varies from 0.01 to 0.99 under the assumption that $P_p = P_n$ and $x = y$.

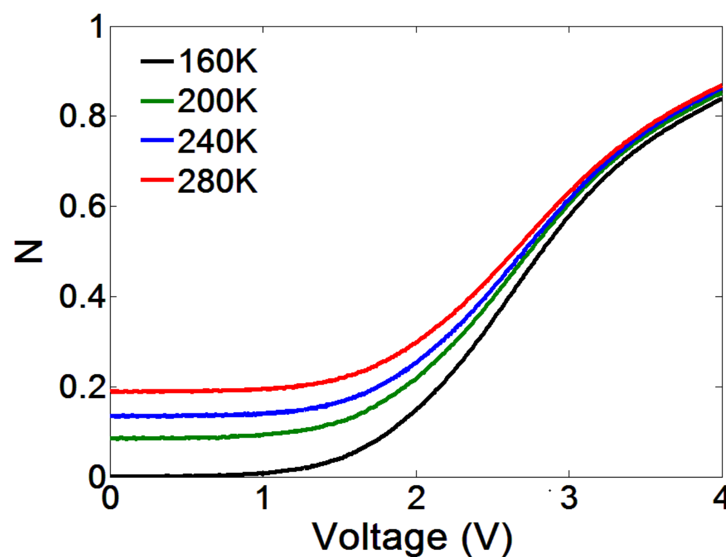

Figure 5.5: Average number of electron-hole pairs N generated by an energetic carriers as a function of the bias voltage at different temperatures, obtained from measured data in Figure. 4.7 and eqn. (5.44).

Furthermore, if we take the diffused junction we discussed in Chapter 4 as an example, under 635 nm light illumination, the average number of electron-hole pairs –

N as a function of bias voltage could be obtained for various temperatures as shown in Figure. 5.5. The gain value was extracted using the measurement data presented in Figure 4.7.

5.2.2 Numerical Calculation Results

Since the cycling excitation process (CEP) highly depends on the probability for the excitation event to happen, Monte Carlo simulations have been performed for the low bias condition to evaluate the gain from numerical calculations.

Based on the analytical model described in the previous section, in the low bias region, a total number of 10000 trials were performed for selection of the value of X and Y. The value of X or Y was set to equal to be either “0” or “1” indicating if one specific excitation event has successfully happened. And the probability p for the value of X or Y equals to 0 or 1 has been assigned manually for the 10000 trials. For simplicity, in order to compare the numerical results with the analytical model, $P_p = P_n = 0.5$ and $x = y$ were assumed. Then the corresponding gain value from this hypothesized p-n junction structure using the analytical model can be expressed as:

$$G_{junction} = \frac{1+0.5(x+y)}{(1-xy)} = \frac{1+x}{1-x^2} \tag{5.45}$$

Figure 5.6(a) and (b) show the histograms of gain distribution for $p = 0.5$ and $p = 0.95$ from Monte Carlo simulations results respectively. And gain was obtained to be equal to $G_{junction} = 2$ for $p = 0.5$ and $G_{junction} = 20$ for $p = 0.95$.

From the histogram of gain distribution, the noise characteristics of the photoresponse amplification mechanism can also be extracted. The excess noise can be characterized by a noise factor defined by the ratio between the mean square value of the gain $\langle G_{junction}^2 \rangle$ and the square of the mean of the gain $\langle G_{junction} \rangle^2$:

$$N.F. = \frac{\langle G_{junction}^2 \rangle}{\langle G_{junction} \rangle^2} \quad (5.46)$$

Therefore, from Figure 5.6(a) and (b), the excess noise factor can be calculated numerically: $N.F.$ =1.2557 for gain at 2 and $N.F.$ = 1.4789 for gain at 20. As expected, both the gain and the spread of the gain (excess noise factor) increase with the mean value of $\langle X_i \rangle / \langle Y_i \rangle$.

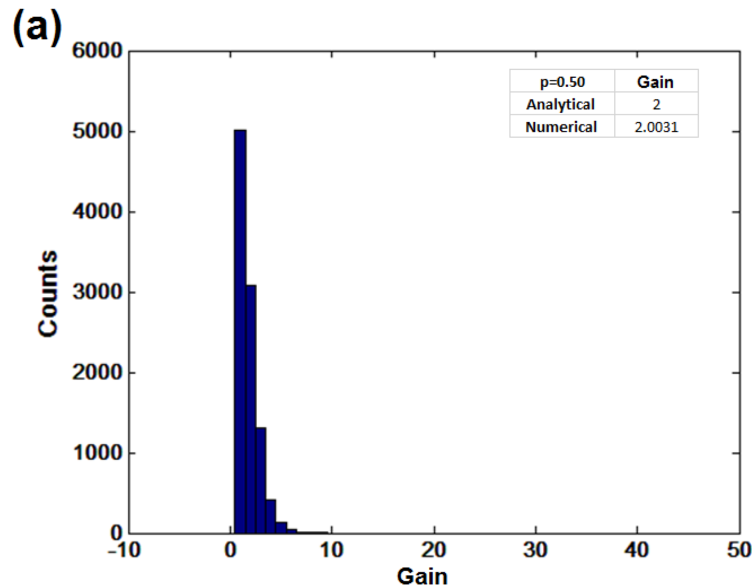

Figure 5.6: (a) Histogram of gain distribution with the e-h pair generation probability at $p = 0.5$ with corresponding gain value of 2 and noise factor N.F. =1.2557. (b) Histogram of gain distribution for $p = 0.95$, with the corresponding gain value of 20.0 and noise factor N.F. =1.4789 (continued).

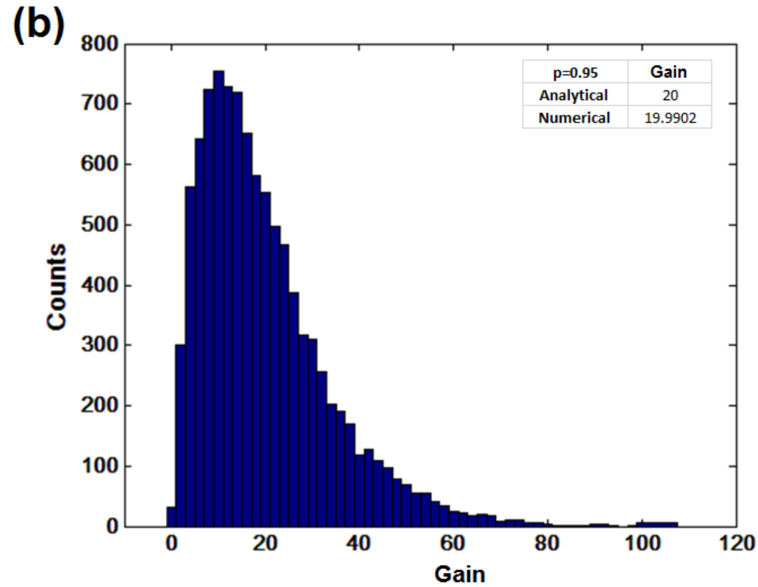

Figure 5.6: (a) Histogram of gain distribution with the e-h pair generation probability at $p = 0.5$ with corresponding gain value of 2 and noise factor N.F. =1.2557. (b) Histogram of gain distribution for $p = 0.95$, with the corresponding gain value of 20.0 and noise factor N.F. =1.4789 (continued).

From Monte Carlo simulations, the relatively small spread of gain distribution also indicates that the excess noise factor for the CEP process is expected to be much lower than that of conventional electron injection avalanche photodiodes [1].

5.3 Conclusion

This chapter discussed the quantum mechanical analysis of the interband transitions including localized states, specifically the derivations of the process of electron excitation from ionized acceptors to the conduction band were described in

details. A more general analysis of the cycling excitation process was introduced and the gain and noise characteristics were also discussed through Monte Carlo simulations.

This chapter, in part, is a reprint of material as it appears in the following publication: Yuchun Zhou, Yu-hsin Liu, Samia N. Rahman, David Hall, L.J. Sham and Yuhwa Lo, "Discovery of a Photoresponse Amplification Mechanism in Compensated PN Junctions", Applied Physics Letters, 106, 031103 (2015). The dissertation author was the primary investigator and author of this material.

Chapter 6

Conclusions

This chapter will provide brief summary on the material presented in the dissertation and outlook on the related research directions.

6.1. Thesis Summary

This thesis presented two major advancements in exploring single crystal silicon's properties: (1) using silicon nanostructures for sub-bandgap photon detection and (2) the discovery of a photoresponse amplification mechanism in compensated silicon p-n junctions. The device design, fabrication, and characterization results have several key contributions, which are summarized in the following:

- Design and fabrication of core-shell silicon nanowire device using the solid-state proximity diffusion method to incorporate all the necessary physical mechanism proposed to enhance infrared light detection capability.
- Creating a model that incorporates three key physical mechanisms behind the sub-bandgap photon absorption process. The model was demonstrated by the implementation of device characterizations.

- Simulation and formulation of an analytical model to understand the physical mechanisms as well as the photoresponse behavior of the nanowire device.
- Design, fabrication and characterization of a heavily doped, highly compensated silicon p-n junction mesa device.
- Experimental observation of a new internal gain behavior in silicon for visible (635 nm) light under various temperatures at very low bias voltage range.
- Development of a physical model – cycling excitation process (CEP) describing the origins of the gain behavior and simulations have been performed in comparisons with measurement results.

The core-shell silicon nanowire device presented in this dissertation has been able to exhibit distinguishable and prominent photoresponse under sub-bandgap light illumination at 1310 nm. A typical and strong bias dependence of the photoresponse behavior indicates that the sub-bandgap absorption is attributed to the intrinsic properties of core-shell silicon nanowires rather than surface states.

The attractive characteristics are based on three physical mechanisms: the Franz-Keldysh effect, the quasi-quantum confinement effect and the impurity state assisted photon absorption. These physical mechanisms were inherently built in the analytical model used to study the sub-bandgap photon absorption process. The strong bias dependence behavior was observed from experimental results and the data match well with the simulation results based on the proposed physical model. It is believed that this

verified concept could lead to the realization of highly efficient, low cost, and CMOS compatible infrared photodetectors and focal plane arrays using single crystal silicon nanostructures.

An internal new photoresponse mechanism in heavily doped, partially compensated silicon p-n junctions under very low bias range was observed using the fabricated mesa devices. The observed photocurrent gain occurs at a bias that is more than an order of magnitude below the threshold voltage for conventional impact ionization. Moreover, the amplified photoresponse is enhanced rather than suppressed with increasing temperature.

Based on the distinctive characteristics, a cycling excitation process (CEP) model was proposed involving the inelastic scattering between energetic carriers and the ionized impurities in the depletion and charge neutral regions of the p – n junction. The gain characteristics have also been analytically modeled based on the CEP process. The model also showed more insights on the contributions to the gain from the depletion region and the charge neutral region respectively.

6.2. Outlook

As discussed intensively in the dissertation, the device performance including the sub-bandgap photon absorption and the gain characteristics depends strongly on the doping profile of specific device structures. Currently, all the devices were fabricated using the proximity diffusion method to over compensate the high background doping concentration. This method gives little control over the doping profiles and makes it

hard to predict device behaviors. Since the concepts of both sub-bandgap light detection and the CEP process have been verified, implementation of epitaxial growth techniques may be a promising solution to produce exact doping profiles for better design control in future research including photoresponse and noise characteristics studies.

One major advantage of the cycling excitation process (CEP) is that the gain occurs at a much smaller voltage (< 10 V) than conventional impact ionization, which makes the process CMOS compatible. This renders the flexibility to incorporate the CEP mechanism into transistors and other device structures to significantly expand the applicability of the effect to other application areas.

Moreover, by bandgap engineering of Si or SiGe heterostructures for integration with the CEP process, the combination between the new gain mechanism and the negative feedback mechanism may also be achieved. Through meticulous design and fabrication, single infrared photon detection using silicon may even be feasible.

References

[1] S. Sze and K. Ng, Physics of Semiconductor Devices, New York: Wiley, 2007.

[2] G. Reed, Silicon Photonics: The State of Art, Wiley-Interscience, 2008.

[3] S. S. Li, Semiconductor Physical Electronics, Springer, 2006.

[4] A. Saha and N. Manna, Optoelectronics and Optical Communication, Laxmi Publications, 2011.

[5] A. Yariv and P. Yeh, Photonics: Optical Electronics in Modern Communications, Oxford University Press , 2007.

[6] M. S. Wartak, Computational Photonics: An Introduction with MATLAB, Cambridge University Press, 2013.

[7] V. A. Kovalev and W. E. Eichinger, Elastic Lidar: Theory, Practice, and Analysis Methods, John Wiley & Sons, 2004.

[8] F. Vignola, J. Michalsky and T. Stoffel, Solar and Infrared Radiation Measurements, CRC Press, 2012.

[9] S. Assefa, F. Xia and Y. A. Vlasov, "Reinventing germanium avalanche photodetector for nanophotonic on-chip optical interconnects," *Nature,* vol. 464, no. 7285, pp. 80-84, 2010.

[10] J. Michel, J. Liu and L. C. Kimerling, "High-performance Ge-on-Si photodetectors," *Nature Photonics,* vol. 4, no. 8, pp. 527-534, 2010.

[11] T. Liang, H. Tsang, I. Day, J. Drake, A. Knights and M. Asghari, "Silicon waveguide two-photon absorption detector at 1.5 μm wavelength for autocorrelation measurements," *Appl. Phys. Lett.,* vol. 81, no. 7, pp. 1323-1325, 2002.

[12] I. Goykhman, B. Desiatov, J. Khurgin, J. Shappir and U. Levy, "Locally Oxidized Silicon Surface-Plasmon Schottky Detector for Telecom Regime," *Nano Letters,* vol. 11, no. 6, pp. 2219-2224, 2011.

[13] A. Zhang, H. Kim, J. Cheng and Y.-H. Lo, "Ultrahigh Responsivity Visible and Infrared Detection Using Silicon Nanowire Phototransistors," *Nano Letters,* vol. 10, no. 6, pp. 2117-2120, 2010.

[14] A. Zhang, S. You, C. Soci, Y. Liu, D. Wang and Y.-H. Lo, "Silicon nanowire detectors showing phototransistive gain," *Appl. Phys. Lett.,* vol. 93, p. 121110, 2008.

[15] 9. A. Itzler, X. Jiang, M. Entwistle, K. Slomkowski, A. Tosi, F. Acerbi, F. Zappa and S. Cova, "Advances in InGaAsP-based avalanche diode single photon detectors," *J. Mod. Opt.,* vol. 58, pp. 174-200, 2011.

[16] E. Yagyu, E. Ishimura, M. Nakaji, H. Itamoto, T. Aoyagi, K. Yoshiara and Y. Tokuda, "Recent advances in AlInsAs avalanche photodiodes," in *Conference on Optical Fiber Communication and the National Fiber Optic Engineers Conference*, 2007.

[17] S. Mandai, M. W. Fishburn, Y. Maruyama and E. Charbon, "A wide spectral range single-photon avalanche diode fabricated in an advanced 180 nm CMOS technology," *Opt. Exp.,* vol. 20, no. 6, pp. 5849-5857, 2012.

[18] B. F. Levine, R. N. Sacks, J. Ko, M. Jazwiecki, J. A. Valdmanis, D. Gunther and J. H. Meier, "A new planar InGaAs–InAlAs avalanche photodiode," *IEEE Photon. Technol. Lett.,* vol. 18, no. 18, pp. 1898-1900, 2006.

[19] M. A. Itzler, X. Jiang, M. Entwistle, B. M. Onat and K. Slomkowski, "Single-photon Detectors Based on InP Avalanche Diodes: Status and Prospects," in *SPIE Proc.*, 2010.

[20] O. Hayden, R. Agarwal and C. M. Lieber, "Nanoscale avalanche photodiodes for highly sensitive and spatially resolved photon detection," *Nature Materials,* vol. 5, pp. 352-356, 2006.

[21] G. Bulgarini, M. E. Reimer, M. Hocevar, E. P. A. M. Bakkers, L. P. Kouwenhoven and V. Zwiller, "Avalanche amplification of a single exciton in a semiconductor nanowire," *Nature Photonics,* vol. 6, pp. 455-458, 2012.

[22] C. Yang, C. J. Barrelet, F. Capasso and C. M. Lieber, "Single p-type/intrinsic/n-type silicon nanowires as nanoscale avalanche photodetectors," *Nano Letters,* vol. 6, p. 2929–2934, 2012.

[23] R. H. Hadfield, "Single-photon detectors for optical quantum information applications," *Nature Photonics,* vol. 3, pp. 696-705, 2009.

[24] K. Foubert, G. Lasfargues, L. Mathieu, S. Benahmed, G. Vojetta, J. Rothman and Q. B. à l. Guillaume, "Development of HgCdTe single-element APDs based detectors for low flux short wave infrared application," in *Proc. SPIE* , 2013.

[25] M. T. Trinh, R. Limpens, W. D. A. M. d. Boer, J. M. Schins, L. D. A. Siebbeles and T. Gregorkiewicz, "Direct generation of multiple excitons in adjacent silicon nanocrystals revealed by induced absorption," *Nature Photonics,* vol. 6, pp. 316-321, 2012.

[26] C. Delerue, G.Allan, J. J. H. Pijpers and M. Bonn, "Carrier multiplication in bulk and nanocrystalline semiconductors: Mechanism, efficiency, and interest for solar cells," *Phys. Rev. B,* vol. 81, p. 125306, 2010.

[27] J. Michel, J. Liu and L. C. Kimerling, "High-performance Ge-on-Si photodetectors," *Nature Photonics,* vol. 4, pp. 527-534, 2010.

[28] Z. H. Zhu, Y. C. Zhou, D. Crouse and Y.-H. Lo, "Pick-and-place multi-wafer bonding for optoelectronic integration," *Electron. Lett. ,* vol. 34, no. 12, p. 1256, 1998.

[29] S. J. S. M. E. G. J. U. Y. D. M. L. a. T. M. L. M. W. Geis, "Silicon waveguide infrared photodiodes with >35 GHz bandwidth and phototransistors with 50 A/W response," *Opt. Express,* vol. 17, no. 7, pp. 5193-5204, 2009.

[30] H. Chen, X. Luo and A. W. Poon, "Cavity-enhanced photocurrent generation by 1.55μm wavelengths linear absorption in a p-i-n diode embedded silicon microring resonator," *Appl. Phys. Lett.,* vol. 95, p. 171111, 2009.

[31] A. Cavallini, L. Polenta, T. Rossi, R. Calarco, R. Meijers, T. Richter and H. Lüth, "Franz-Keldysh Effect in GaN Nanowires," *Nano Letters,* vol. 7, no. 7, pp. 2166-2170, 2007.

[32] S. G. McMeekin, M. R. S. Taylor, B. Vögele, C. R. Stanley and C. N. Ironside, "Franz–Keldysh effect in an optical waveguide containing a resonant tunneling diode," *Appl. Phys. Lett.,* vol. 65, p. 1076, 1994.

[33] D. A. B. Miller, D. S. Chemla and S. Schmitt-Rink, "Electroabsorption of highly confined systems: Theory of the quantum-confined Franz–Keldysh effect in semiconductor quantum wires and dots," *Appl. Phys. Lett.,* vol. 52, p. 2154, 1988.

[34] S. G. McMeekin, M. R. S. Taylor, B. Vögele, C. R. Stanley and C. N. Ironside, "Franz–Keldysh effect in an optical waveguide containing a resonant tunneling diode," *Appl. Phys. Lett.,* vol. 65, p. 1076, 1994.

[35] D. Miller, Quantum Mechanics for Scientists and Engineers, New York : Cambridge, 2008.

[36] J. Davies, The Physics of Low-Dimensional Semiconductors: An Introduction, New York: Cambridge, 1998.

[37] S. Lindsay, Introduction to Nanoscience, Oxford University Press, 2009.

[38] S. L. Chuang, Physics of Photonic Devices, John Wiley & Sons , 2012.

[39] M. Lax and E. Burstein, "Broadening of impurity levels in silicon," *Phys. Rev.* , vol. 100, pp. 592-602, 1955.

[40] Y. Arakawa and A. Yariv, "Quantum well lasers--Gain, spectra, dynamics," *IEEE J. Quantum Electron.,* vol. 22, no. 9, pp. 1887-1899, 1986.

[41] D. K. Schroder, Semiconductor Material and Device Characterization, John Wiley & Sons, 2006.

[42] Y. Zhou, Y.-H. Liu, J. Cheng and Y.-H. Lo, "Bias Dependence of Sub-Bandgap Light Detection for Core–Shell Silicon Nanowires," *Nano Letters,* vol. 12, pp. 5929-5935, 2012.

[43] Y.-H. Liu, Y. Zhou and Y.-H. Lo, "High efficiency silicon 1310 nm detector without defect states or heteroepitaxy," *Appl. Phys. Lett.,* vol. 103, p. 041119, 2013.

[44] W. Tsang, "Part D - Photodetectors," in *Semiconductors and Semimetals*, New York , Academic Press , 1985.

[45] Y. K. Su, C. Chang and T. Wu, "Temperature dependent characteristics of a PIN avalanche photodiode (APD) in Ge, Si and GeAs," *Opt. Quant. Electron.,* vol. 11, pp. 109-117, 1979.

[46] R. Sooryakumar, A. Pinczuk, A. C. Gossard, D. S. Chemla and L. J. Sham, "Tuning of the valence-band structure of GaAs quantum wells by uniaxial stress," *Phys. Rev. Lett.* , vol. 58, p. 1150, 1987.

[47] J. Shah and G. Iafrate, "Hot Carriers in Semiconductors," in *Proceedings of the Fifth International Conference*, Boston, 1987.

[48] J. F. Verwey, R. P. Kramer and B. J. d. Maagt, "Mean Free Path of Hot Electrons at the Surface of Boron~Doped Silicon," *J. Appl. Phys.,* vol. 46, pp. 2612-2619, 1975.

[49] J. Singh, Electronic and Optoelectronic Properties of Semiconductor Structures, Cambridge University Press, 2007.

[50] F. Williams, "Donor—acceptor pairs in semiconductors," *Phys. Stat. Solidi,* vol. 25, no. 2, pp. 493-512, 1968.

[51] J. Pankove, Optical Processes in Semiconductors, Dover Publications, 2010.

[52] E. Rashba and M. Sturge, Excitons: Modern Problems in Condensed Matter Sciences, Amsterdam: North-Holland, 1982.

[53] P. Y. Yu and M.Cardona, Fundamentals of Semiconductors – Physics and Materials Properties (2nd Edition), Springer, 1999.

[54] D. G. Thomas, J. J. Hopfield and W. M. Augustyniak, "Kinetics of Radiative Recombination at Randomly Distributed Donors and Acceptors," *Phys. Rev.,* vol. 140, p. A202, 1965.

[55] N. Mott, Disordered Semiconductors, Plenum Press, 1987.

[56] D. S. Lee and J. G. Fossum, "Energy-band distortion in highly doped silicon," *IEEE Trans. Electron. Devices,* Vols. ED-30, no. 6, pp. 626-634, 1983.

[57] 2. E. B. Xavier Blase1, C. Chapelier, T. Klein and C. Marcenat, "Superconducting group-IV semiconductors," *Nature Materials,* vol. 8, pp. 375-382, 2009.

[58] D. Adler, Amorphous Semiconductors, Cleveland: CRC Press, 1971.

[59] B. K. Ridley, Quantum Processes in Semiconductors (Fifth Edition), Oxford University Press, 2013.

[60] A. F. J. Levi, Applied Quantum Mechanics, Cambridge University Press, 2006.

[61] M. Lundstrom, Fundamentals of Carrier Transport, Cambridge University Press, 2009.